TRANSIENTLY DEVELOPING FREE AND OPPOSING JETS IN RELATION TO GAS-ASSISTED LASER EVAPORATIVE HEATING PROCESS

BY

GHULAM MURSHED ARSHED

A Thesis Presented to the

DEANSHIP OF GRADUATE STUDIES

In Partial Fulfillment of the Requirements
for the Degree

MASTER OF SCIENCE

In

MECHANICAL ENGINEERING

KING FAHD UNIVERSITY OF PETROLEUM AND MINERALS

Dhahran, Saudi Arabia

RABI'-I 1424 H
MAY 2003

KING FAHD UNIVERSITY OF PETROLEUM AND MINERALS
DHAHRAN 31261, SAUDI ARABIA

DEANSHIP OF GRADUATE STUDIES

This thesis, written by **GHULAM MURSHED ARSHED** under the direction of his thesis advisor and approved by his thesis committee, has been presented to and accepted by the Dean of Graduate Studies, in partial fulfillment of the requirements for the degree of **MASTER OF SCIENCE IN MECHANICAL ENGINEERING** .

Thesis Committee

Dr. S.Z. Shuja (Thesis Advisor)

Prof. B.S. Yilbas (Member)

Dr. Faleh A. Al-Sulaiman
Department Chairman

Prof. M.O. Budair (Member)

Prof. Osama A. Jannadi
Dean, College of Graduate Studies

Date

Dedicated to

My Parents, Brothers, Sisters and Wife

ACKNOWLEDGEMENTS

Words cannot at all express my thankfulness to Almighty **Allah**, *subhanahu-wa-ta ala*, the most Merciful; the most Benevolent Who blessed me with the opportunity and courage to complete this task.

First and foremost gratitude is due to the esteemed institution, the **King Fahd University of Petroleum and Minerals** for my admittance, and to its learned faculty members for imparting quality learning and knowledge with their valuable support and able guidance that have led my way through this point of undertaking my research work.

My heartfelt gratitude and special thanks to my thesis advisor learned **Professor S.Z. Shuja**. I am grateful to him for his consistent help, untiring guidance, constant encouragement and precious time that he has spent with me in completing this course of work. I do admire his exhorting style that has given me tremendous confidence and ability to do independent research. Working with him in a friendly and motivating environment was really a joyful and learning experience.

I must appreciate and thank **Professor B.S. Yilbas** for his constructive and

positive criticism, extraordinary attention and thought-provoking contribution in my research. It was surely an honor and an exceptional learning experience to work with him.

I am grateful to **Professor M.O. Budair** for his help, advice, cooperation and comments.

I would like to acknowledge the Chairman of Mechanical Engineering Department **Dr. Faleh Al-Sulaiman** for his cooperation in providing the computer lab facility.

Sincere friendship is the spice of life. I owe thanks to my graduate fellow students from Pakistan, India and Saudi Arabia; most particularly, Iftekhar, Ovais, Zamin, Zahid Qamar, Salman, Kamran, Hasan, Bilal, Muneib, Ahmad, Sohail, Fahim, Junaid, Jawwad, and Fahad. I would also appreciate Javed, Muzaffar, Kaukab, Raheel, Umar, Kashif, Adnan, Navaid, Imran, Shakir, Qadir, Alam, Aqeel, and Faisal Iftekhar for their priceless love and sincerity which really helped me in building my personality.

Family support plays a vital role in the success of an individual. I am thankful to my entire family for its love, support and prayers throughout my life especially my dearest mother and father who devoted their lives in the endeavor of getting me a quality education, my dearest brothers: Ghulam Sarwar, Ghulam Mohammad,

and Ghulam Mustafa, my dearest sisters: Sughra Sulatana, Najma and Asma and my dearest sister's husband, Mohammad Azam, and my dearest brother-in-law, Mohammad Arafat. Not to forget the true affection and encouragement of my dearest wife, Mehnaz, that gave me the meaning of everything in my life.

I would in the end must appreciate the efforts of my brothers who supported me a lot during my education and without their help I could not achieve my goals.
May Allah help us in following Islam according to Quran and Sunnah ! *(Aameen)*

Contents

List of Figures

List of Tables

Abstract

Name: Ghulam Murshed Arshed

Title: Transiently Developing Free and Opposing Jets in Relation to Gas-Assisted Laser Evaporative Heating Process

Major Field: Mechanical Engineering

Date of Degree: MAY 2003

Laser finds wide application in industry due to its precision of operation, low cost, and local processing. Since the laser machining is involved with complex physical processes, the modeling of laser induced heating gives insight into the physical processes involved. Moreover, model studies reduce the experimental cost and provide parametric data for heating optimization.

Laser heating of solid substrate surface results in evaporated vapor jet, which emanates from the surface. Depending upon the magnitude of laser beam intensity, the evaporated vapor jet develops transiently, which implies that the velocity profile of the jet varies spatially and temporally. In practical laser heating process an assisting gas jet coaxial with the laser beam impinges onto the transiently developing vapor jet. In the present study, a high temperature transiently developing helium jet, imitating the vapor ejection from a laser induced cavity, and an opposing steady air jet, resembling the assisting gas jet, are modeled numerically. Since the thermophysical properties of the evaporating surface are not known in the open literature, helium at high temperature is considered as the transiently developing jet. In order to predict the flow, temperature, and species mass fraction fields, the governing equations are solved numerically using the finite volume method. To validate the present computational model, the simulation conditions are changed and the predictions are compared with the experimental results available in the literature.

It is found that the assisting air jet influences considerably the flow field in the region close to the transiently developing jet. In the early stage transiently developing jet expands in the axial direction and as the time progresses radial expansion of the jet dominates due to the assisting air jet which suppresses the transiently developing jet expansion in the axial direction; in which case, a circulation cell next to the assisting air jet boundary is developed. The radial jet developed due to opposing of transiently developing and assisting air jets behaves similar to the free jet, and the transiently developing jet characteristics do not affect considerably the radial free jet characteristics.

Master of Science Degree
King Fahd University of Petroleum and Minerals
MAY 2003

خلاصة الرسالة

الاسم: غلام مرشد ارشد
عنوان الرسالة: ناقاثان حر ومعاكس له نامیان و متغيّران مع الوقت بالنسبة الى غاز مساند لعملية التبخر بواسطة التسخين باليز

التخصص: هندسة ميكانيكية
تاريخ الشهادة: مايو 2003 , ربيع الأول هـ

نظرا لدقة عملية التسخين ، رخصة التكلفة والقدرة على تحديد مكان العمل بواسطة الليزر، فإن له تطبيقات واسعة في الصناعة . وبما أن عملية التصنيع بواسطة الليزر تتضمن تعقيدات فيزيائية ، فإن نمذجة التسخين بواسطة الليزر تعطي مدخل إلى فيزيائية عملية التصنيع . بالإضافة إلى ذلك فإن دراسات النمذجة تقلل من التكلفة المخبرية وتزود الباحث بمعلومات تحت حالات مختلفة (باراميترك) للوصول إلى أفضل حالة تسخين بواسطة الليزر .

نتيجة إلى تسخين أساس السطح الصلب بالليزر فإن بخار نفاث ينبعث منه . اعتمادا على مقدار كثافة شعاع الليزر فإن البخار النفاث المنبعث يتغير مع الوقت وهذا يعني بأن شكل سرعة البخار النفاث تتغير مع الفراغ والزمن . في التطبيقات العملية للتسخين بالليزر يوجد غاز نفاث مساعد في نفس محور شعاع الليزر , يرتطم مع البخار النفاث المتغير. في الدراسة الحالية تم نمذجة غاز هليوم نفاث نام ومتغير مع الوقت ذو درجة حرارة عالية ، يمثل البخار المنبعث من التجويف المستحث بواسطة الليزر . كما تم نمذجة هواء نفاث منتظم مع الوقت معاكس للهليوم . نظرا لكون الخواص الفيزيائية الحرارية للسطح المتبخر غير معروفة في البحوث المنشورة ، فإن الهليوم عند درجة الحرارة العالية اختير ليمثل الغاز النفاث المتنامي مع الوقت . لكي يمكن التنبؤ بمجالات الانسياب والحرارة ، فإن المعادلات المتعلقة بذلك تم حلها حسابيا باستخدام طريقة التحكم بالحجم . ولإجازة النموذج الحسابي فإن حالات المحاكاة تم تغييرها ونتيجة هذا التغيّر تمت مقارنته مع النتائج العملية الموجودة في البحوث.

في هذه الدراسة وجد أن الهواء النفاث يؤثر بشكل كبير على مجالات التدفق في المنطقة القريبة من الهليوم النفاث المتنامي . في المرحلة البدائية فإن النفاث النامي يتمدد في الاتجاه المحوري وكلما تقدم الوقت فإن التمدد القطري للنفاث يصبح أكثر حضورا لأن نفاث الهواء المساعد يحصر النفاث النامي المحوري . في هذه الحالة تنتج خلية دوران بجانب الهواء النفاث المتنامي . والنفاث القطري الناتج بسبب النفاث المتنامي مع الوقت ونفاث الهواء المساعد ، يشبه في سلوكه النفاث الحر ، وأما بالنسبة لخواص النفاث المتنامي فهي لا تؤثر بشكل معتبر على خواص النفاث القطري الحر .

درجة الماجستير في العلوم
جامعة الملك فهد للبترول و المعادن
الظهران المملكة العربية السعودية
مايو 2003 , ربيع الأول هـ

Nomenclature

a	coefficients used in discretized equations
c	speed of sound $\left(\frac{m}{s}\right)$
A	area (m^2)
b_j	half velocity width of the jet (m)
b	constant in source term in Eq. (4.16)
CV	control volume
c_p, c_v	specific heat of a mixture at constant pressure and volume $\left(\frac{J}{Kg \cdot K}\right)$
c_{p_k}	specific heat of the k^{th} species at constant pressure $\left(\frac{J}{Kg \cdot K}\right)$
C	various empirical constants in turbulence model
d	diameter of the jet at the inlet (m)
D	jet width (m)
$D_{e,\ w,\ n\ or\ s}$	diffusion conductance times area $\left(\frac{Kg}{s}\right)$
D_{im}	diffusion coefficient of the i^{th} species in the mixture $\left(\frac{m^2}{s}\right)$
$\widetilde{e}$	Favre-averaged specific internal energy of a mixture $\left(\frac{J}{Kg}\right)$
E	total specific internal energy of a mixture $\left(\frac{J}{Kg}\right)$
E_w	wall roughness parameter in Eq. (3.41)
f	various wall functions used in Eqs. (3.23 & 3.25)
F_j	mass flux through the face 'j' $\left(\frac{Kg/s}{m^2}\right)$
$F_{e,\ w,\ n\ or\ s}$	mass flow rate through the face of the control volume $\left(\frac{Kg}{s}\right)$

G	production rate of turbulence kinetic energy $\left(\frac{Kg}{m \cdot s^3}\right)$
$grad$	gradient
h_k	specific enthalpy of the k^{th} species $\left(\frac{J}{Kg}\right)$
h_k^o	specific enthalpy of the k^{th} species at T_{ref} $\left(\frac{J}{Kg}\right)$
$\widetilde{h}$	Favre-averaged specific enthalpy of a mixture $\left(\frac{J}{Kg}\right)$
h''	fluctuating component of mixture specific enthalpy $\left(\frac{J}{Kg}\right)$
H	total specific enthalpy of a mixture $\left(\frac{J}{Kg}\right)$
J_j	total flux (convection plus diffusion) across the face 'j' $\left(\frac{Kg/s}{m^2} \times [\phi]\right)$
$J_{e,\ w,\ n\ or\ s}$	integrated total flux over the control volume face $\left(\frac{Kg}{s} \times \ [\phi]\right)$
k	turbulence kinetic energy $\left(\frac{m^2}{s^2}\right)$
k_{in}	turbulence kinetic energy at the jet inlet $\left(\frac{m^2}{s^2}\right)$
l_m	mixing length (m)
$\dot{m}_{in}$	mass flux at the jet inlet (inlet to control volume) $\left(\frac{Kg/s}{m^2}\right)$
M_t	turbulence Mach number
$\dot{M}_{He}$	total exit momentum flow rate at helium jet inlet $\left(\frac{Kg \cdot m/s}{s}\right)$
$\dot{M}_{Air}$	total exit momentum flow rate at air jet inlet $\left(\frac{Kg \cdot m/s}{s}\right)$
n	exponent in Eq. (3.30)
$\widehat{n}$	unit normal vector
N_s	total number of gaseous species
PD	pressure-dilatation $\left(\frac{Kg}{m \cdot s^3}\right)$
$\overline{p}$	time-averaged pressure of a mixture (Pa)

$\overline{p}\,'$	pressure correction (Pa)
$\overline{p}^{*}$	guessed pressure (Pa)
p'	fluctuating component of mixture pressure (Pa)
P	Pee function in Eq. (3.45)
$P_{e,\ w,\ n\ or\ s}$	Peclet number
q_w	wall heat flux $\left(\frac{Watt}{m^2}\right)$
r	distance along the radial direction (m)
r_o	radius of the jet inlet in Eq.(3.30) (m)
R	gas constant $\left(\frac{J}{Kg \cdot K}\right)$
$\overline{R}$	time-averaged source term in Eq. (3.2) $\left(\frac{Kg/s}{m^3}\right)$
$\overline{S}_h$	time-averaged source term in Eq. (3.5) $\left(\frac{Watt}{m^3}\right)$
S_o	constant in source term in Eq. (4.6) $\left(\frac{Kg/s}{m^3} \times [\phi]\right)$
S_P	coefficient of source term in Eq. (4.6) $\left(\frac{Kg/s}{m^3}\right)$
$\overline{S}_\phi$	arbitrary time-averaged source term in Eq. (3.46) $\left(\frac{Kg/s}{m^3} \times [\phi]\right)$
t	time (s)
T_{ref}	mixture reference temperature $(= 298.15\ K)$
$\widetilde{T}$	Favre-averaged temperature of a mixture (K)
T''	fluctuating component of mixture temperature (K)
T_{in}	temperature at the jet inlet (K)
T_w	wall temperature (K)
T_p^+	dimensionless temperature at near wall point y_p
T_p	temperature at near wall point y_p (K)

$\widetilde{u}$	Favre-averaged axial velocity $(\frac{m}{s})$
$\widetilde{u}^{n-1}$	velocity along x-direction of the previous iteration $(\frac{m}{s})$
$\widetilde{u}'$	velocity correction along x-direction $(\frac{m}{s})$
$\widetilde{u}^*$	guessed velocity along x-direction $\left(\frac{m}{s}\right)$
u''	fluctuating component of axial velocity $(\frac{m}{s})$
u_i, u_j	arbitrary velocity $(\frac{m}{s})$
$\widetilde{u}_i$, $\widetilde{u}_j$	Favre-averaged arbitrary velocity $(\frac{m}{s})$
u_i'', u_j''	fluctuating component of arbitrary velocity $(\frac{m}{s})$
u_p	resultant tangential velocity $(\frac{m}{s})$
u^+	dimensionless resultant tangential velocity
u_o	maximum axial velocity at the jet inlet $(\frac{m}{s})$
u_{in}	axial velocity at the jet inlet (inlet to control volume) $(\frac{m}{s})$
u_τ	resultant friction velocity $(\frac{m}{s})$
$\widetilde{\mathrm{v}}$	Favre-averaged radial velocity $(\frac{m}{s})$
$\widetilde{\mathrm{v}}^{n-1}$	velocity along r-direction of the previous iteration $(\frac{m}{s})$
$\widetilde{\mathrm{v}}'$	velocity correction along r-direction $(\frac{m}{s})$
$\widetilde{\mathrm{v}}^*$	guessed velocity along r-direction $(\frac{m}{s})$
v''	fluctuating component of radial velocity $(\frac{m}{s})$
v_{in}	radial velocity at the jet inlet (inlet to control volume) $(\frac{m}{s})$
$\widetilde{\mathrm{V}}$	Favre-averaged velocity magnitude $(\frac{m}{s})$
x	axial distance (m)
x_i, x_j	arbitrary distance (m)
y_p	normal distance from point p to the solid wall (m)

y_p^+	dimensionless normal distance from point p to the solid wall
$\widetilde{Y}_i$, $\widetilde{Y}_k$	arbitrary Favre-averaged mass fraction
Y_i'', Y_k''	fluctuating component of arbitrary species mass fraction
$\widetilde{Y}_{He}$	Favre-averaged mass fraction of helium
$\widetilde{Y}_{N_2}$	Favre-averaged mass fraction of nitrogen
$\widetilde{Y}_{O_2}$	Favre-averaged mass fraction of oxygen
Z_t	penetration depth/length (m)

Greek symbols

α	closure constants in Eq. (3.20)
$\alpha_{\tilde{u}}, \alpha_{\tilde{v}}, \alpha_{\overline{p}}$	under-relaxation factors
γ	specific heat ratio of a mixture (c_p/c_v)
Γ	diffusion coefficient $\left(\frac{Kg}{m \cdot s}\right)$
δ_{ij}	Kronecker delta
ϵ	dissipation rate of turbulence kinetic energy $\left(\frac{m^2}{s^3}\right)$
ϵ_{in}	dissipation rate of turbulence kinetic energy at the jet inlet $\left(\frac{m^2}{s^3}\right)$
κ	von Karman's constant
μ	laminar dynamic viscosity of a mixture $\left(\frac{Kg}{m \cdot s}\right)$
μ_t	eddy viscosity of a mixture $\left(\frac{Kg}{m \cdot s}\right)$
$\overline{\rho}$	time-averaged density of a mixture $\left(\frac{Kg}{m^3}\right)$
ρ'	fluctuating component of mixture density $\left(\frac{Kg}{m^3}\right)$
σ	laminar Prandtl number
$\sigma_t, \sigma_{\tilde{Y}}$	turbulent Prandtl number and turbulent Schmidt number
$\sigma_k, \sigma_\epsilon$	turbulence constants in Eqs. (3.17) & (3.18) respectively
$\overline{\tau}_{ij}$	time-averaged stress tensor (Pa)
τ_w	wall shear stress (Pa)
ϕ	arbitrary variable
$[\phi]$	unit of arbitrary variable (ϕ)
$\forall$	volume (m^3)

subscripts

amb	ambient
in	inlet
i, j	arbitrary direction
i, j, k	indices used to represent different species
i, j	indices used in grid staggering
I, J	indices used in grid staggering
P	a typical node in the computational domain
o	maximum
t	turbulent
w	wall
N, S, E, W	nodes around a control volume
n, s, e, w	interface of a node to its north, south, east, or west

Chapter 1

INTRODUCTION

The word laser is an acronym for "Light Amplification by Stimulated Emission of Radiation". Albert Einstien in 1917 showed the process of stimulated emission must exist but it was not until 1960 that T.H. Maiman first achieved laser action at optical frequencies in ruby. The basic principles and construction of a laser are relatively straightforward and is somewhat surprising that the invention of the laser was so long delayed.

In the time which has elapsed since Maiman first demonstrated laser action in ruby in 1960, the applications of lasers have multiplied to such an extent that almost all aspects of our daily life are touched upon by lasers. They are used in many types of industrial processing, engineering, meteorology, scientific research, communications, holography, medicine and for military purposes.

The laser is a unique source of radiation capable of delivering intense coherent electromagnetic fields in the spectral range between the ultraviolet and the far infrared. This laser beam coherence is manifested in two ways: *i*) it possesses good temporal coherence qualities since it is highly monochromatic, and *ii*) it is spatially coherent - as evidenced by the nearly constant phase wave front and directionality of

the emitted light. The temporal coherence of the laser is a measure of the ability of the beam to produce interference effects as a result of differences in path lengths and is, therefore, important for such applications as interferometry and holography. The spatial coherence is particularly important for power applications where it provides the capability of focusing all the laser's available output energy into an extremely spot size. Thus power densities, which are unattainable with any other source of light, can be attained.

Spatial and temporal coherence are properties that have long been recognized as indispensable for various industrial and laboratory applications. Long before the advent of the laser, light possessing various degrees of coherence could be obtained by filtering ordinary light. However, the filtering process resulted in an output beam of such low intensity as to render such techniques useless in most practical applications. It remained for the laser, with its inherent properties of coherence and high intensity, to demonstrate the applicability of optical electromagnetic radiation to numerous new technologies.

1.1 Types of Lasers

There are mainly four broad classes of lasers available classified on the basis of lasing medium. These include gas lasers, solid state lasers, semiconductor lasers and organic dye lasers.

1.1.1 Gas Lasers

Gas lasers utilize a gaseous material as the active laser medium. They can provide continuous beam of laser in some cases. There are three subcategories of gas lasers, which are neutral gas lasers: helium-neon lasers, argon lasers, krypton lasers and xenon lasers; ionized gas lasers: argon ion lasers, krypton ion lasers and helium-cadmium lasers; and molecular lasers: carbon dioxide lasers, fast gas transport CO_2 lasers, gas dynamic lasers, nitrogen lasers and carbon monoxide lasers.

1.1.2 Solid State Lasers

The solid-state laser is characterized by active media involving ions of an impurity in some solid host material. The laser material is in the form of a cylindrical rod with the ends polished, flat and parallel. The ions commonly employed are either ions of the transition metals such as chromium, manganese. Cobalt and nickel or of rare earth element. The host material in which these impurity elements are embedded tend to be hard, gemlike crystalline materials, or alternatively glasses. The typical examples are ruby lasers, Nd: YAG lasers and Nd: glass lasers.

1.1.3 Semiconductor Lasers

A semiconductor laser uses a small chip of semiconductor material. In size and appearance it is similar to transistor. Examples are GaAs lasers, ZnS lasers, ZnO lasers and CdS lasers.

1.1.4 Organic Dye Lasers

These lasers employ liquid solutions of certain dye materials. The dye materials are relatively complex organic molecules with molecular weights of several hundred. These materials are dissolved in organic solvents commonly methyl alcohol. Thus, the active material for dye lasers is liquid.

1.2 Interaction of Laser with Materials

Laser application areas have been mentioned above and among them our focus is on laser machining of materials.

When a laser beam falls on the surface of a substrate, part of it is absorbed and part of it is reflected. The energy that is absorbed begins to generate a heat-affected zone where the microstructure of the substrate material may alter. Depending upon the time scale of interaction of laser with the material and the intensity (power per unit area) of the laser, the material may undergo sublimation, melting or both melting and vaporization. The phenomena of sublimation takes place when a very high intensity (of the order of $10^{13}\ W/m^2$) and short pulse of the order of 10 nanoseconds) laser beam strikes the surface of the substrate. On the other hand, the phenomenon of melting takes place when a low intensity (of the order of $10^9\ W/m^2$ or less) and long pulse (of the order of milliseconds) laser strikes the surface of the substrate. However, the phenomena of melting and vaporization both occur when laser beam of intensity of the order of $10^{11}\ W/m^2$ and pulse of the order of several hundred milliseconds

strikes the surface of the substrate.

The sketch (Fig. 1.1) shows the interaction of the laser with the material. The sketch shows that when a laser beam strikes the surface of the substrate material it undergoes heating and subsequent phase change processes. There are various regimes as indicated in the sketch; a melt pool which is the region between solid-liquid interface and liquid-vapor interface, a zone of mixture of molten material and vapor which is above the liquid-vapor region, a vapor jet zone ($6 - 9\ mm$) which is above the initial surface of the material, and the retarding zone which is about $21 - 24\ mm$ above the vapor jet zone.

Such localized heating can produce an enormous amount of thermal stress to cause fracture in the material if the thermal stress exceeds the fracture strength of the material. Mechanical damage can also be caused to the substrate material due to the shock waves generated during laser-material interaction. The shock waves are produced due to the recoil pressure of the vapor generated during rapid vaporization. Also continuous exposure of the vapor to the laser beam may lead to formation of plasma which, in turn, interacts with the laser beam to generate shock waves.

Depending upon the assisting matter used in the process (e.g. gas, liquid or powder), which influences the process (i.e., cools, removes melt, reacts etc.), chemical reactions may take place between the assisting matter and the workpiece if they are chemically reactive. This results in the activation of the various phenomena such as burning, sintering, soldering, alloying, etc.

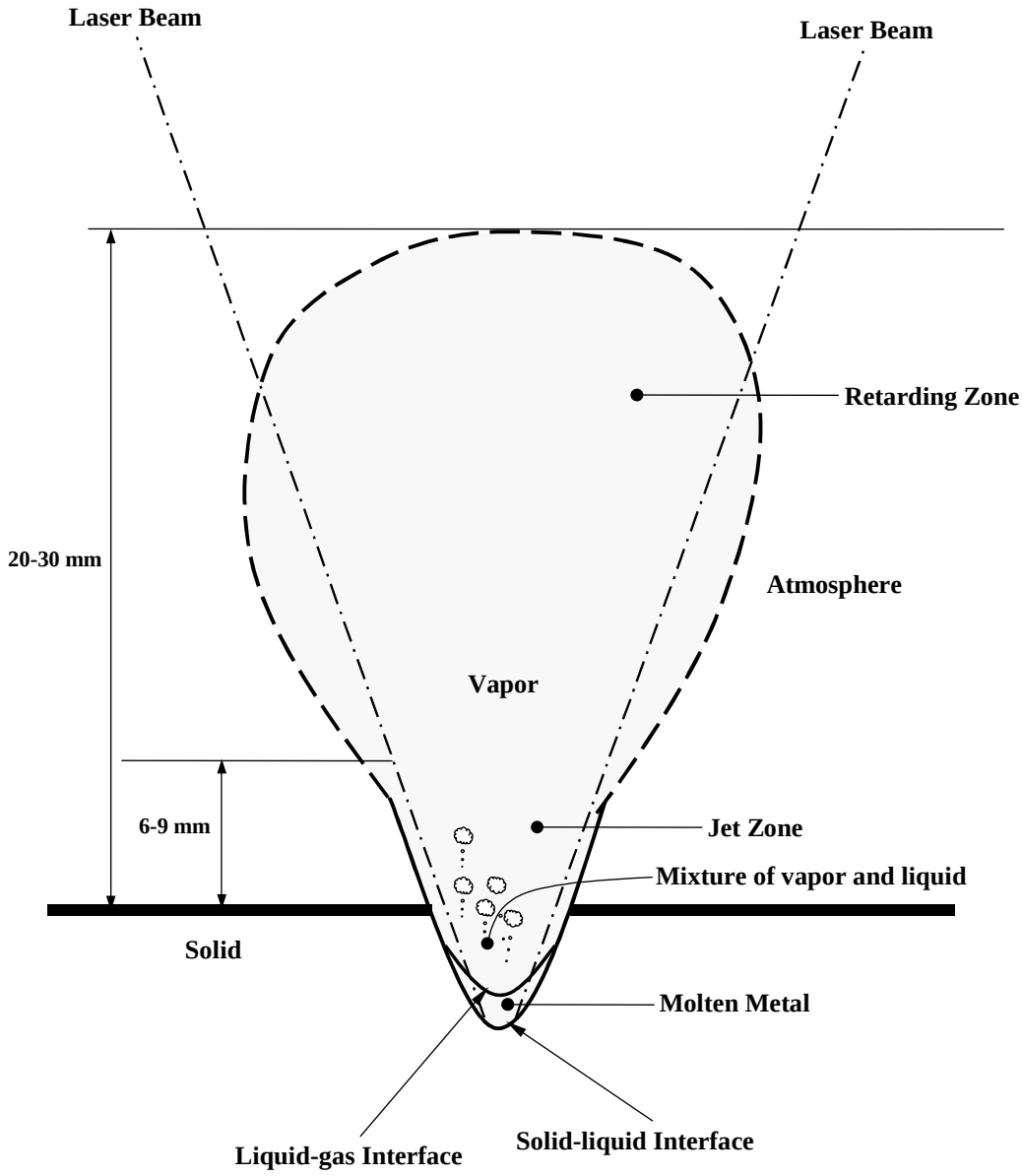

Figure 1.1: Sketch showing laser heating of a solid surface and subsequent phase change processes.

1.2.1 Classification of Laser Heating

Laser heating of the engineering metals is involved with two processes.

- Conduction-limited laser heating.
- Non-conduction-limited laser heating.

1.2.1.1 Conduction-Limited Laser Heating

If the substrate material remains solid and no phase change occurs during laser heating then the heating process is called conduction-limited laser heating. The typical examples are laser heat treatment, laser hardening, laser fracturing and laser sheet bending.

1.2.1.2 Non-Conduction-Limited Laser Heating

Laser heating process in which phase change of the substrate material is involved is called non-conduction-limited laser heating. The typical examples are laser welding, laser drilling, laser cutting, laser grooving, laser scribing, laser marking, laser shock processing and laser surface alloying.

1.2.2 Advantages of Laser Machining

Laser offers the following advantages in material processing:

1. There is no mechanical contact with the work-piece material and contamination problems are reduced.

2. The heat-affected zone surrounding the area is small.

3. The laser works well with hard, brittle materials or refractory materials, and it can sometimes work for joining dissimilar metals, which are difficult to weld by conventional techniques.

4. Small hole-diameters in case of drilling can be achieved.

5. The operation is very fast, occurring in approximately $10^{-12} - 10^{-3}$ sec . with pulse lasers.

6. The processing is readily adapted to automation.

7. No welding electrodes are required in case of laser welding.

8. Extremely small welds may be accomplished on delicate materials.

9. Inaccessible areas or even encapsulated materials can easily be reached with laser beam.

10. Higher power per unit area can be delivered by laser beam as compared to that by any other thermal source.

11. No vacuum is required. For most applications the work can be done in any atmosphere, although for some reactive metals a shielding atmosphere may be desirable.

1.2.3 Disadvantages of Laser Machining

There are also some disadvantages as follows:

1. The main disadvantage is that it is a thermal process which limits its use to only particular applications.

2. The control of size and tolerances on laser-produced holes is not perfect.

3. The sizes of the pieces that can be welded are relatively small and the depth of penetration is limited, except for multi-kilowatt lasers.

4. The depth of penetration for laser-produced holes is limited, although repeated shots can increase the depth.

5. Re-condensation of vaporized material occurs on the walls and on the lip of the hole, forming a raised rim around the entrance.

6. The walls of the holes are sometimes rough.

7. The cross-sections of laser-produced holes are not completely round, and the holes taper from the entrance to the exit sides.

8. In laser welding, careful control of the pulse parameters is required to prevent vaporization of the surfaces.

9. In some cases the costs are high.

1.2.4 Formation of Jet and the Use of Assisting Gas During Laser Heating

In the case of non-conduction limited heating process, an assisting gas is used; provided that assisting gas has two fold effects *i*) shields the laser irradiated region from the oxidation reaction, and *ii*) results in high temperature exothermic reaction enhancing the energy available at the irradiated region. When modeling the heating process, therefore, the effect of assisting gas should be considered. Moreover, during the non-conduction limited heating process, a cavity is formed due to the recession of

the surface. Consequently, the size of the cavity increases as the heating progresses. In this case, change of molten state into a vapor state results in vapor molecules with excessive velocity departing from the cavity wall. This in turn generates an excessive recoil pressure in the cavity. The mass removed from the cavity, due to the departure of the evaporated molecules, enhances the recession velocity of the cavity wall, which in turn enlarges the cavity size. As this process evolves, a drilled through-hole or a cut is resulted. Consequently, when modeling the evaporation process, the flow of vapors from the cavity should be included in the analysis.

1.3 Scope of the Present Study

Laser heating of solid substrate surface results in evaporated vapor jet, which emanates from the surface. Depending upon the magnitude of laser beam intensity, the evaporated vapor jet develops transiently, which implies that the jet properties including the velocity profile of the jet vary spatially and temporally. In practical laser heating process an assisting gas jet coaxial with the laser beam impinges onto the transiently developing vapor jet. In the present study, a high temperature transiently developing helium jet, imitating the vapor ejection from a laser induced cavity, and an opposing steady air jet, resembling the assisting gas jet, are modeled numerically. Since the thermophysical properties of the evaporating surface are not known in the open literature, helium at high temperature is considered as the transiently developing jet. In order to predict the flow, temperature and mass fraction fields, the governing equations are solved numerically using the finite volume method. The

grid independent solution will be assured by laying the physical domain onto a properly oriented and spaced mesh system. To validate the present computational model, the simulation conditions are changed and the predictions are compared with the experimental results available in the literature.

Chapter 2

LITERATURE SURVEY

2.1 Introduction

There is a great variety of jet flows in nature. Examples of such flows of paramount importance are jet impingement on the surface, free-jets, jets in cross-flow, opposing jets, etc. The literature on jet impingement on the surface, free-jets and jets in cross-flow is large except on developing transient turbulent jet. As will become evident in this survey, the type of free jet and opposing jet considered in the present study has not been adequately investigated either experimentally or theoretically. Nevertheless, limited literature does exist and will be mentioned. One of the main reasons why these developing transient turbulent jet and opposing jets are important in the present study is as follows; the former is actually the outcome of laser ablation of the metal surface and the latter is the result of applying the assisting cool gas jet (with different material composition, say air, from that of developing transient turbulent jet evolving from the ablated metal surface) impinging onto the high-temperature transient jet. With the perception of the idea that impingement process will take place in the present work, though impingement of two opposing jets, it will not be irrelevant if some background regarding the jet impingement on various types of surfaces is given in the literature

survey. Therefore, in the literature survey the relevant and the logical way is to describe jet impingement first, then the free-jets, and finally the opposing jets.

The laser heating process in which the material does not undergo phase change is known as conduction limited heating process. The conduction limited heating is, of course, not the issue in the present study and therefore the focus of the study is limited to the other type of laser heating process known as non-conduction limited laser heating process. In non-conduction limited laser heating process, such as drilling, material undergoes solid heating, melting and evaporation. The evaporating front forms a transient jet emanating from the surface of the substrate material. Consequently, laser non-conduction limited heating process is involved with melting and cavity formation inside the substrate material and expansion of the evaporated surface. Considerable research studies were carried out to examine the physical processes involved during non-conduction limited heating process and a few are presented in the last section of this survey.

2.1.1 Jet Impingement

The flow and heat transfer characteristics of impinging laminar jets issuing from rectangular slots of different aspect ratios were investigated numerically by Sezai and Mohamad [1] through the solution of three-dimensional Navier-Stokes and energy equations in steady state. The three-dimensional simulation revealed the existence of pronounced stream-wise velocity off-center peaks near the impingement plate. Furthermore, they also investigated the effect of these off-center velocity peaks on the

Nusselt number distribution. They detected interesting three-dimensional flow structures that could not be predicted by two-dimensional simulations.

Numerical investigation of heat transfer under confined impinging turbulent slot jets was carried out by Tzeng et al [2]. They employed eight turbulence models, including one standard and seven low-Reynolds-number $k-\varepsilon$ models, and tested them to predict the heat transfer performance of multiple impinging jets. Their validation results indicated that the prediction by each turbulence model depended on grid distribution and numerical scheme used in spatial discretization. Besides, they set spent fluid between the impinging jets to reduce the cross-flow effect in degradation of the heat transfer of downstream impinging jets. They showed that the overall heat transfer performance could be enhanced by proper spent fluid removal.

Seyedein et al [3] presented results of numerical simulation of the steady turbulent flow field and impingement heat transfer due to three and five turbulent heated slot jets discharging normally into a confined channel. They used both the Lam-Bremhorst low Reynolds number and the standard high Reynolds number versions of $k-\varepsilon$ turbulence models to model the turbulent multi-jet flow. They found that Lam-Bremhorst model over-estimated the normalized heat transfer coefficient, while the standard high Reynolds number model under-estimated it.

Yang and Shyu [4] presented numerical predictions on the fluid flow and heat transfer characteristics of multiple impinging slot jets with an inclined confinement surface. They used two turbulence models to describe the turbulent structure: the standard $k-\varepsilon$ turbulent model associated with wall function and the Lam-Bremhorst

version of the low-Re $k-\varepsilon$ model. The numerical results showed that the maximum local Nusselt number and maximum pressure on the impinging surface moved downstream while the inclination angle was increased. The maximum local Nusselt number decreased while the value of the local Nusselt number downstream increased with increasing inclination angle. They also noted the calculated streamline contours, in that the entrance Reynolds number had little effect on the size of the re-circulation region but the inclination angle had a significant effect on the re-circulation zones. They found inclination of the confined surface to accelerate the fluid flow leveled the local Nusselt number distribution on the impingement surface.

Numerical simulation of transient cooling of a hot solid by an impinging free surface jet was carried out by Fujimoto et al [5]. They predicted numerically thermal fields in the liquid as well as the temperature distributions in the hot solid. Initially they examined the steady flow and compared it with experimental data. They found the predicted flow structures agreed reasonably well with the experimental data. Furthermore, they studied the transient cooling of the hot solid and found the heat flux between the liquid and the solid was very large near the stagnation point because the temperature gradient at the surface was large. The heat flux in the stagnation region decreased as the cooling process progressed. The liquid film thickness varied with time due to the temperature dependent viscosity and the heat flux increased with Reynolds number.

Numerical simulation of a free jet of a high Prandtl number fluid impinging perpendicularly on a solid substrate of finite thickness containing electronics on the

opposite surface was carried out by Rahman et al [6]. They developed numerical model considering both solid and fluid regions and solved it as a conjugate problem. They investigated the influence of different operating parameters such as jet velocity, heat flux, plate thickness, nozzle height, and plate material. They validated the computed results with the available experimental data. They found that the local Nusselt number was the maximum at the center of the disk and decreased gradually with radius as the flow moved downstream. The average Nusselt number and the maximum temperature in the solid varied significantly with impingement velocity, disk thickness, and thermal conductivity of the disk material.

A study that examined jet impingement on a surface having a constant heat flux over a limited area was carried out by Shuja et al [7]. In this study, they took air as the impinging gas and simulated the process with a two-dimensional form of the governing conversation equations. They introduced four turbulence models, including standard $k-\varepsilon$, low-Reynolds-number $k-\varepsilon$, and two Reynolds stress models to account for the turbulence. They compared the predicted flow properties with the previously experimental data and found that the RSTM model predictions of the flow field close to the surface agreed better with the experimental findings as compared to the standard $k-\varepsilon$ and low-Re $k-\varepsilon$ models. However, they obtained similar temperature fields from RSTM and low-Re $k-\varepsilon$.

Numerical simulation of three-dimensional laser heating of steel substrate when subjected to impinging gas was also carried out by Shuja et al [8] They considered the gas jet impinged onto the workpiece surface co-axially with the laser beam. They

tested the $k-\varepsilon$ model with and without corrections and the Reynolds stress model under conditions of constant heat flux introduced from the solid wall. They selected the low-Re- $k-\varepsilon$ model to account for the turbulence whereas they used the transient Fourier heat conduction equation to compute the temperature profiles in the solid substrate. They extended their study to include four gas jet velocities, and they found that the impinging gas jet velocity had a considerable effect on the resulting gas side temperature. Moreover, the temperature at the surface decreased rapidly as the radial distance from the heated spot center increased. In addition, the temperature profiles inside the solid substrate were not influenced considerably by the assisting gas jet velocity.

Impinging jet studies for turbulence model assessment were carried out by Craft et al [9]. They applied four turbulence models to the numerical prediction of turbulent impinging jets discharged from a circular pipe measured by Cooper et al [10]. These included one $k-\varepsilon$ eddy viscosity model and three second-moment Reynolds stress closure models. The numerical predictions indicated that the $k-\varepsilon$ model and one of the Reynolds stress models led to far too large levels of turbulence near the stagnation point. This excessive energy in turn induced much too high heat transfer coefficients and turbulent mixing with the ambient fluid. The other two second-moment closure models, adopting new schemes for accounting for the wall's effect on pressure fluctuations, did much better; though one of them was clearly superior in accounting for the effects of the height of the jet discharged above the plate. However, none of the schemes was entirely successful in predicting the effects of Reynolds number. They

suggested the main cause of the failure was the two-equation eddy viscosity scheme adopted in all cases to span the near-wall sub-layer rather than the outer layer models on which their study was focused.

The cooling of a heated pedestal mounted on a flat plate was numerically simulated by Parneix et al [11]. They adopted normal velocity relaxation turbulence model (V2F model) in an axisymmetric geometry and they obtained results for a range of Reynolds numbers and jet-to-pedestal distances. They showed that the local heat transfer coefficient exhibited a minimum in the stagnation region, which was rather different from the behavior of an impinging jet on a flat plat. They concluded that complex features like separation and re-attachment on the plate strongly influenced the wall temperature distribution and heat transfer. For comparison, they also obtained results with the widely used $k - \varepsilon$ turbulence model and found that the agreement with the data was poor.

An experimental study of flow field of an axisymmetric, confined and submerged turbulent jet impinging normally on a flat plate was carried out by Fitzgerald and Garimella [12, 13] using Laser-Doppler Velocimetry. Experiments were conducted with two different nozzle diameters, with a range of nozzle-to-target spacing and with a range of Reynolds number. They mapped the toroidal re-circulation pattern in the out flow region, characteristic of confined jets, and presented velocities and turbulence levels over a fine measurement grid in the pre-impingement and wall-jet regions.

Studies on vortex structure and heat transfer in the stagnation region of an impinging plane jet were conducted by Sakakibara et al [14]. They measured velocity

and temperature field in the stagnation region of an impinging jet simultaneously by digital particle image velocimetry and laser-induced fluorescence. They observed counter-rotating vortex pairs in the stagnation region which swept cold fluid toward the wall and ejected high-temperature fluid toward the outer region. The weighed probability distribution function (pdf) of the turbulent heat flux indicated that the contribution of this ejection mechanism to the net heat flux was dominant. The stream-wise vortex pair was transported from the free-jet region to the stagnation region, and the vorticity was amplified by the main stream of what in the vicinity of the wall.

An experimental study was carried by Chung et al [15] to investigate the flow and heat transfer characteristics by jets impinging upon the rib-roughened convex surface. They found similar Nusselt number distributions for both smooth and roughened surfaces. However, after the first rib position, the Nusselt numbers on the rib-roughened surface were higher than Nusselt number on the smooth surface. They found heat transfer rate increased due to flow separation and re-attachment for pitch to height ratio of the rib greater or equal to 10. Beyond the region corresponding to the ratio of stream-wise distance from the stagnation point to the pipe nozzle diameter, the rib roughness did not affect the heat transfer.

2.1.2 Free Jets

The fully developed flow field farther away from the tube exit is well described by the Schlichting's similarity solution [16]. However, the similarity assumption failed

to hold in the developing region of the jet close to the exit. Analytical solutions for the developing jet from a fully developed laminar tube flow were conducted by Lee et al [17]. Their work proposed two approximate methods to analytically calculate the developing jet velocity field from a fully developed laminar (parabolic) axisymmetric tube flow.

Three-dimensional turbulent jets with rectangular cross-section were simulated numerically by Wilson and Demuren [18]. They performed computations for different inlet conditions, which represented different types of jet forcing within the shear layer. They observed the phenomenon of axis-switching in some cases; and at low Reynolds numbers, it was based on self-induction of the vorticity field, whereas at higher Reynolds numbers, the turbulent structure became the dominated mechanism in natural jets. Budgets of the mean stream-wise velocity showed that convection was balanced by gradients of the Reynolds stresses and the pressure.

A pdf (Probability Density Function) approach to explain the turbulent axisymmetric free jet flow was adopted by Chen and Hong [19]. Their computational results revealed that the pdf approach gave consistency in the higher-order moments and radial budget of third moments of velocity, and that the neglect of the mean-strain production, the rapid part of the pressure correction and the dissipation were responsible for deviations between moment-closure models and experiments. Hence, the pdf models appeared to be more suitable than conventional moment-closure models in terms of revealing turbulence structure.

Numerical predictions of mean and turbulent characteristics of the axisymmetric

vertical jet (momentum-dominated) and plume (buoyancy-dominated) were reported by Pereira and Rocha [20]. They used an algebraic stress and flux model to close the time-averaged Navier-Stokes and energy equations and gave special attention to the numerical model, which was based on a finite-volume discretization of the elliptic form of flow equations. They used special procedure to treat free boundaries and to compute the flow up to the similarity regime. Their results showed that the essential characteristics of the flows, especially for the plumes, were correctly reproduced. However, some discrepancies arose from the comparison of predicted and experimental results.

A numerical study was performed by Riopelle et al [21] to determine the influence of weak ambient motion and of the associated pressure field on the flows of free plane vertical turbulent jets and plumes. A nested grid control volume technique with buoyancy-extended $k - \varepsilon$ model plane was used to model turbulent jets and plumes issuing into open spaces as well as into two-dimensional rooms of various sizes. The results indicated that slight variations in the ambient pressure distribution affected jet and plume development and similarity relationships.

Near-wall modeling of plane turbulent wall jets was done by Gerodimos and So [22]. After its failure to predict the jet spreading correctly, they investigated the appropriateness of two-equation modeling; particularly the importance of near-wall modeling and the validity of the equilibrium turbulence assumption. They analyzed an improved near-wall model and three others, and compared predictions of these with measurements of plane wall jets. They calculated the jet spread correctly by the

improved model, which was able to replicate the mixing behavior between the outer jet-like and inner wall layer and was asymptotically consistent. They obtained good agreement with other measured quantities. However, other near-wall models tested were incorrect to predict the jet spread.

Numerical simulation of turbulent jet flow and combustion was carried out by Zhou et al [23]. Their work applied $k - \varepsilon$ turbulent model, with pressure boundary condition for the entrainment atmosphere surface, to calculate the steady free jet flow. Based on the fulfillment of the above isothermal jet flow, they simulated combusting jet flows of diffusion flame and partial premixed-flame using the assumption of fast chemical reaction and Eddy-Dissipation Concept (EDC) model, respectively. They compared their numerical results with the experimental and theoretical results. Their numerical results of isothermal jet and diffusion jet flame agreed well with tests by Panchapahesan and Lumley [24], and Lockwood and Moneib [25]. They found that EDC model had some errors in modeling partial premixed jet flames.

Numerical simulations of two-dimensional laminar methane/air premixed jet flames with a detailed chemical kinetics mechanism were also conducted by Zhou et al [26]. The focal point of the work was to demonstrate the sensitivity of the modeling of the detailed chemical kinetics on the flame temperature and concentrations of major components for three different equivalence ratios. They found the temperature and major species distributions were in good agreement with the experimental measurements by Nguyen et al. [27], but some radical species profiles still deviated from experiments. They obtained the typical flame structure of the steady jet.

Numerical modeling of turbulent jet diffusion H_2/air flame with detailed chemistry was carried out by Zhou et al [28]. Their focus was on the investigation of an axisymmetric turbulent hydrogen/air diffusion flame using a time-dependent numerical model with a detailed chemical mechanism. They used an algebraic correlation closure (ACC) model to couple turbulence and chemistry. They found temperature and major species distributions were in good agreement with experimental measurements. They showed that the numerical results obtained from the detailed chemistry calculations depended on how the turbulent diffusion coefficients were selected for species and energy equations.

Studies on transient turbulent gaseous fuel jets for diesel engines were carried out by Hill and Ouellette [29]. They determined the conditions under which transient turbulent jets were self-similar, quantified the appropriate similarity parameter and tested the assumption of self-similarity even with under expansion and with jet injection near a boundary wall. They used the idea of Turner [30] that the transient turbulent jet could be modeled as a steady jet headed by a spherical vortex to evaluate the constant of proportionality used to establish the direct relationship between the jet penetration distance well downstream of the virtual origin with the square root of the time and the fourth root of the ratio of nozzle exit momentum flow rate to chamber density. Using incompressible transient jet observations to determine the asymptotically constant ratio of maximum jet width to penetration distance, and the steady jet entrainment results of Ricou and Spalding [31], they established the penetration constant. They showed this constant was also true for compressible flows

with substantial thermal and species diffusion, and even with transient jets from highly under-expanded nozzles. They made observations of transient jet injection in a chamber in which, as in diesel engine chambers with gaseous fuel injection, they directed the jet at a small angle to one wall of the chamber. In those tests with under-expanded nozzles they found that at high nozzle pressure ratios, depending on the jet injection angle, the jet penetration could be consistent with the established penetration constant. At low-pressure ratios the presence of the wall noticeably retarded the penetration of the jet.

Turbulent transient gas injections were also studied by Ouellette and Hill [32]. They used multi-dimensional simulations to analyze the penetration, mixing, and combustion of such gaseous jets. They evaluated the capability of multi-dimensional numerical simulations based on $k - \varepsilon$ turbulence model to reproduce the experimentally verified penetration rate of free transient jets. Their model was found to reproduce the penetration rate dependencies on momentum, time, and density but was more accurate when they modified one of the $k - \varepsilon$ coefficients. They used the simulation to determine the impact of chamber turbulence, injection duration, and wall contact on transient jet penetration. They showed gaseous jets and evaporating diesel sprays with small droplet size mixed at much the same rate when injected with equivalent momentum injection rate.

Entrainment characteristics of transient gas jets were proposed by Abraham [33]. He presented results of theoretical analysis and computation of transient gas jets in a quiescent ambient environment, with injected to three ambient density ratios.

He used $k - \varepsilon$ model for turbulence and showed that the entrainment rate varied linearly with axial penetration and the total mass entrained had cubic dependence on axial penetration of the gas jet. He found that the actual values of these quantities depended on a constant whose value obtained from measurements and quoted in the literature varied by as much as a factor of 2.

A numerical scheme for the transient simulation of incompressible turbulent confined jet flow of variable density was developed by Singh et al [34]. Their scheme was capable of capturing the essential flow features of confined jet flows and it predicted the level of ambient fluid entrainment fairly accurately. They found that aspect ratio and density ratio were the main factors that influenced entrainment and mixing. These factors were also responsible for causing jet instability and re-circulation within the mixing tube. They showed that Reynolds number had a negligible effect over the entrainment ratio. Moreover, as the jet moved away from the tube inlet, the level of entrainment increased for short distances and vice-versa. On the other hand, mixing between the jet and the entrained fluid improved if they moved the jet away from the tube inlet.

The turbulent exponential jet was studied by Breidenthal [35]. He postulated a new self-similar flow when nozzle exit velocity employed was exponentially increasing in time. He argued that the acceleration of the jet would imply a lower entrainment rate.

The jet characteristics of CNG injector with MPI system were studied by Boyan et al [36]. They developed a theoretical model that assumed the natural gas transient

jet could be characterized as a spherical vortex interacting with a steady jet. They employed Schlieren photographs that revealed a low-pressure gas jet's starting and extending process from the nozzle. They compared the model with the experimental results for the tip penetration of round jet and found the results had similar characteristics. The results showed that the tip penetration was proportional to the square root of time. Moreover, the tip penetration of the gas jet was longer than that of gasoline provided that the per unit time calorific values of the injecting fuel were the same.

Experimental investigations of the development of transient jets and evolving jet diffusion flames were carried out by Park and Shin [37] using a high-speed Schlieren photography. They measured the jet tip penetration velocities and normalized jet widths of the primary vortex. They showed that the development behavior in the presence of a flame was greatly different from that in a transient jet. The discernible differences were the delay of the roll-up of the primary vortex, the faster spreading after the roll-up due to the exothermic expansion, and the survival of only a primary vortex. They reported that the jet tip penetration velocity varied with downstream distance and an increase in Reynolds number gave rise to a higher tip penetration velocity.

The velocity field of fully pulsed air jets (no mass flow in between pulses) was studied experimentally in detail by Bremhorst and Hollis [38]. They found the entrainment in fully pulsed air jets was much higher than the steady or partially pulsed jets. Even though the jet spreading and volumetric entrainment were increased in

these pulsatile jet flows, the basic structure of the jet did not change. The velocity profiles were self-similar; the spreading rate was linear with the downstream distance; and most importantly, the entrainment scaled with the square root of the aggregate jet momentum flux. The results were consistent, except for the proportionality constants, with Taylor's entrainment hypothesis [39].

Experimental investigation of unsteady submerged axisymmetric jets was carried out by Fang and Sill [40]. They measured the centerline velocities of linearly accelerating turbulent jets. The results of the experiment indicated that significant deviations (lower normalized velocities) from the steady case existed in the linearly accelerating jets. These aberrations were observed even in the far field. This was interesting since the majority of the pulsed jets were effective only in the near field. However, in this study of unsteady jets carried out by Fang and Sill [40], neither the spreading rates nor the entrainment rates were reported for these monotonically changing unsteady jets.

Kouros et al [41] measured the spreading rate of an unsteady turbulent jet. They reported the penetration length and spreading rate of a non-harmonic unsteady jet. They found the visible spreading rate of an unsteady jet produced by their experimental set up was less than half of the steady jet value.

The experimental investigation of round, incompressible, impulsively started turbulent jets was carried out by Johari et al [42].They found that the flow was comprised of a starting vortex that separated from the rest of the jet in the near field. The starting vortex and the flow immediately behind it were in unsteady motion. They found

the penetration of the jet tip scaled with the square root of time, normalized by the nozzle diameter and velocity, and the celerity of the jet tip was approximately one-half of the centerline velocity of a steady jet, with the same nozzle exit velocity, at the same location. Results of chemically reactive experiments indicated that the fluid in the vicinity of the jet tip mixed with the ambient fluid faster than the rest of the jet. Their findings revealed that the extent of the region near the jet tip with improved mixing became larger as the jet traveled further downstream. They found the more rapid mass mixing at the jet tip implied faster momentum diffusion, which corroborated the slowing down of the jet tip in comparison of the steady jet.

Detailed measurements of the centerline-mixing behavior in the near field of variable-density jets were performed by Papadopoulos and Pitts [43]. They made real-time measurements of jet fluid concentration for a propane jet and a methane jet issuing into still air utilizing Rayleigh light scattering. They used fully developed turbulent conditions as initial conditions and made testing for flow rates yielding Reynolds numbers in the range $3.3 \times 10^3 - 2.3 \times 10^4$, based on average discharge velocity, exit diameter and initial fluid properties. They found that the centerline decay characteristics in the near field exhibited a downstream shift with increasing Reynolds number, which was attributed to the initial velocity distribution at the jet exit. The investigation of the mean and turbulent characteristics of the initial velocity distribution yielded a proposed near-field scale variable that effectively captured this dependence on Reynolds number. They achieved the collapse of the near-field centerline velocity and concentration distribution using the proposed scaling. More-

over, they extended their analysis for a constant density jet to the intermediate and self-similar far fields further downstream using a dynamic length scale based on the local centerline turbulent intensity [44]. The normalized mean velocity distributions of an air jet collapsed over the entire flow distance investigated when they normalized the axial distance by the proposed length scale, thus scaling the virtual origin shift and effectively incorporating the Reynolds number dependence.

Mi and Nathan [45] experimentally investigated the effect of small vortex-generators (tabs) placed at the exit plane of an axisymmetric smooth contraction on scalar mixing in the developing region of a turbulent jet. They showed that the presence of tabs profoundly distorted the jet flow field and consequently modified the scalar mixing characteristics significantly. They found that tabs caused the mean temperature to decrease more rapidly with the downstream distance, implying an increased mixing rate. Furthermore, they found that two tabs distorted the jet from axisymmetric state more dramatically than four tabs.

Natural coherent structures in the near field of an axisymmetric jet was educed and their dynamics studied experimentally by Aydore and Disimile [46] using hot-wire anemometry. They positioned the jet, originating from a fully developed turbulent pipe flow, four jet diameters upstream from an impingement plate. Based on the pipe diameter, they maintained a jet Reynolds number of 1.3×10^4. Using the life cycle method for coherent structure eduction, they obtained phased-averaged vorticity contours in the jet near field, within 2.3 diameters of the pipe exit. Vorticity contours suggested that large coherent structures existed in the middle of the shear

layer at approximately one jet diameter downstream from the pipe exit. Their size was the maximum at this location. A decay region was also observed 1.6 diameters downstream from the pipe exit. Moreover, they evaluated individual terms in the coherent vorticity equation and examined significant terms.

Turbulent flow and heat transfer characteristics of a two-dimensional oblique wall attaching offset jet (a two-dimensional slot jet issued into quiescent surroundings above an inclined plate) were experimentally investigated by Song et al [47]. They measured the local Nusselt number using liquid crystal as a temperature sensor, the jet men velocity, turbulent intensity and wall static pressure coefficient profiles. They observed that the time-averaged re-attachment point nearly coincided with the maximum Nusselt number point for all oblique angles, but the maximum pressure point did only for zero inclination. They found the decay of the maximum jet velocity in the stream-wise direction obeyed the conventional $-1/2$ power law of the wall attaching offset jet for the inclination angle (oblique angle) less than or equal to 30°. They well correlated the re-attachment length and maximum pressure point with offset ratio (height of the jet/diameter of the jet) and oblique angle. They presented correlations between the maximum Nusselt number and Reynolds number for all oblique angles tested.

2.1.3 Opposing Jets

Hosseinalipour and Mujumdar [48, 49] dealt with the numerical simulation of the flow, mixing, and thermal characteristics of a symmetric steady laminar two-

dimensional confined opposing jet configuration for the case when the two jets were equal and unequal. They presented results for two boundary conditions; constant wall temperature and insulated walls. They made an extensive parametric study to investigate the effects of geometric, hydrodynamic, and thermal parameters on the flow and heat transfer characteristics of such systems. They showed that mixing of two oppositely directed confined jets caused major hydrodynamic distortions, which persisted in the merged flow in the exit channel. The results for three different configurations showed that the decaying disturbances and the flow re-development that occurred affected significantly the heat transfer in the exit channel. Their findings showed that unequal jet configuration with different width jets caused more distortion in the flow field compared to equal jet and unequal jet with equal jet width configurations. They found these distortions affected the Nusselt number distribution on both top and bottom more than those for the equal jet and unequal jet with equal jet width.

Johnson [50] examined impingement of laminar fluid jets in a confined cylindrical chamber using flow visualization, Laser Doppler Anemometry (LDA) measurements and steady and unsteady three-dimensional finite volume numerical simulations using boundary fitted non-orthogonal coordinates. He presented results that dealt with the cases of flow imbalance issuing from the nozzles. His measurements and flow visualization of unequal flow cases with ∼3:1 flow rate ratios in an opposed two jet configuration indicated an asymmetric flow field with significant downward recirculation from the region away from the nozzles to the nozzle region and a jet-to-jet

impingement point very close to the low flow rate nozzle. Steady and unsteady numerical simulations he made confirmed the asymmetry of the flow field at these conditions and he found reasonable agreement for the jet-to-jet impingement point. He showed large areas of re-circulation in the mix chamber would lead to poor mixing due to the possibility of unmixed fluid leaving the chamber and the increase in the residence time of the mixing fluids. Subsequent to the above study, the author's results herein [51] dealt with modifying an existing flow imbalance and suggested alternative momentum arrangements to improve the flow characteristics.

Hosseinalipour and Mujumdar [52] investigated numerically to predict and to compare the fluid flow and heat transfer characteristics of two-dimensional turbulent confined and opposing jet flows. They used five low-Reynolds-number $k - \varepsilon$ models and the standard high-Reynolds-number model. They also tested the newly proposed Yap correction with low-Reynolds-number models in order to investigate its effect on the heat transfer predictions for the impinging jet case. They found that in some models this correction improved the heat transfer predictions. They compared the simulation results with the available data for fluid flow and heat transfer for a single slot jet impingement on a flat plate. They presented only numerical results for the opposing jet case due to lack of experimental data. They performed a parametric study for flow and heat transfer characteristics in the opposing jet configuration.

Heat transfer between two opposed, non-isothermal jets under corotation was investigated numerically by Sheu and Liou [53]. They analyzed the efficiencies of heat transfer between two jets under various system conditions. They also included

the problem in the limit of zero rotating speed on one side in their work. They found a critical rotating speed in this limit at which the efficiency of heat transfer was minimum. They made a comparison of efficiencies of heat transfer among typical cases. Furthermore, they interpreted relevant results physically.

Lam and Chan [54] investigated the penetration and spreading of a round jet into an ambient counter-flow using the planer laser-induced fluorescence (LIF) technique. The LIF images enabled them to obtain the instantaneous concentration field of the penetrating jet effluent. They observed large-scale wandering of jet penetration, which led to significant temporal and spatial fluctuations in the location of the dividing interface between jet effluent and ambient fluid. They found that the penetration distance and the lateral spreading width of the jet exhibited fluctuations with covering ranges as large as their corresponding time-averaged values. They found the degree of fluctuations in these penetration and spreading parameters increased with the jet-to-current velocity ratio, but essentially scaled with the mean penetration distance. They also attempted to predict the mean penetration distance by considering the decay of centerline jet velocity under a hypothesis that the counter-flow affected the jet via a simple compression of the axial coordinates of the jet flow.

A two impinging jet mixer for precipitation process was investigated by means of the laser induced fluorescent technique by Benet et al [55]. They used neutralization reactions with a fluorescent PH-indicator to reveal the mixing process up to the molecular level. They derived a phenomenological mixing model on the basis of experimental results. The mixing model involved a macro-dilution process and a

coalescence-redispersion process through which the fluids were contacted at the molecular level. They applied the mixing model to the precipitation of barium sulfate and found predictions were very close to experimental results.

Witze and Dwyer [56] used a hot-film anemometer to investigate the mean velocity and turbulence intensity distributions in turbulent radial jets. They showed a geometric parameter termed as the constrained ratio (nozzle diameter to separation distance) to characterize radial-jet behavior. They defined constrained radial jet as one for which the nozzle walls constrained the flow leaving the orifice to be parallel if the constraint ratio was large. They also defined a small constraint ratio which was representative of two opposing free axisymmetric jets, the collision of which produced an impinged radial jet. They found that the well-behaved constraint radial jet spread at the same rate as did the familiar plane jet, whereas the impinged radial jet spread at a rate more than three times as fast. They demonstrated that neither type of radial jet was amenable to a self-similar analytic solution and they showed the impinged radial jet required numerical solution technique. They demonstrated an empirical solution for the constrained radial jet.

An experimental investigation of a conical flow formed by the interaction of two asymmetric turbulent curved wall jets past a circular cone was presented by Jarrah et al [57]. They made measurements of velocity and turbulence intensity profiles of the two jets in the wall jet, the interaction, and the merged jet regions. They found the location of the interaction region of the two opposing curved wall jets and flow direction of the merged jet depended primarily on the ratio of the slot exit velocities

of the two jets. The mean velocity and stream-wise turbulence intensity profiles of the merged jet were similar to those in a turbulent free jet. Self-similar mean velocity profiles for different values of downstream location prevailed up to the beginning of the interaction region, regardless of jet exit velocity ratios. They showed that stream-wise and lateral turbulence intensities increased with increasing the stream-wise distance up to the interaction region, where the turbulence behavior became random and was characterized by larger peak values of the turbulence intensity compared to the wall jet region. Moreover, they showed that the maximum velocity decay and jet half-width growth increased parabolically with stream-wise distance and observed no significant effect of the conical shape. They carried out flow visualization for several exit jet velocity ratios and saw three-dimensionality to be reduced as the secondary jet momentum increased.

2.1.4 Non-Conduction Limited Laser Heating

Gonsalves and Duley [58] presented the results of a quantitative investigation into the interdependence of the parameters, the incident power, the radius of the focused spot on the target, the cutting speed, the cut width and the sheet thickness. They also showed how these results could be generalized to provide a prediction of the power required to achieve a certain cutting velocity or cut width with predetermined focal area on thin sheets of arbitrary composition.

Modest and Abakians [59] considered partial vaporization of a semi-infinite medium caused by a moving Gausian laser irradiation (across the vaporization surface). They

used a simple integral method for the evaluation of temperature distribution, assuming relatively minor thermal losses due to convection, conduction and radiation. They solved the relevant non-linear partial differential equation numerically and presented the results for the groove depth, width and shape for variety of laser and solid parameters. Their results clearly indicated that surface heat losses were nearly always negligible. It was seen that, for a Gaussian beam, the bottom of the groove might have a sharp apex. The model was also able to predict quantitatively groove depths accurately for a few situations.

Bang and Modest [60] analyzed numerically multiple reflection and beam guiding effects during laser machining. They considered that the surface of the treated material reflected the laser irradiation in a fully diffuse fashion, limiting the analysis to bodies that had a rough surface during laser evaporation (e.g. micro-explosive removal, violent surface boiling). For local irradiation calculations the material surface was divided into a number of triangular elements with liner interpolation functions. The net radiative flux for these elements was obtained from standard view factor theory. The irradiation calculations were combined with a simple integral method governing conduction losses into the medium, and the resulting groove shape and depth were found through an iterative procedure. They concluded that beam guiding played an important role in forming the fully developed groove, resulting in an increased effective absorptivity. Due to channeling from the upstream wall as well as the side walls, the evaporation zone extended farther down-stream and the fully developed groove cross-sections had steeper groove walls with a flatter center region

as compared to that predicted by the previous model without reflection effects. For materials with relatively large reflectivity, the material removal rate was increased significantly, resulting in an increased effective absorptivity. Generally, the beam guiding effects became significant for high reflectivity materials and/or deep groove cases. The groove depth could be increased by using lenses with larger focal lengths focused slightly inside the material. Larger focal length lenses had larger minimum beam radii at the focal plane, but with a lower beam divergence focused near the surface. On the other hand, flatter grooves with steeper walls could be obtained by using lenses with shorter focal lengths.

Roy and Modest [61] developed a three dimensional conduction model to predict the temperature distribution inside the solid and the shape of a groove formed by partial evaporation of a semi-infinite body using a moving CW laser with a Gausian beam profile. This had application in laser machining where material was removed by repeated scanning of a focused beam on the work piece surface. They solved the governing equation using a finite difference method on an algebraically generated boundary-fitted coordinate system. They presented the groove shape and temperature distribution in the solid for both constant properties and variable properties, for different speeds, for various laser power levels and for different beam profiles. The groove shapes for constant thermal properties were compared with three-dimensional boundary element conduction model solution and a quasi-one-dimensional conduction model solution, in which the conduction losses were approximated using a simple integral method. Their model compared well with the three-dimensional boundary

element model for all ranges of laser parameters, and, when thermal losses due to conduction were minor, the one-dimensional results were also in good agreement with the three-dimensional boundary element predictions. They concluded that heat loss by conduction could be between 25 to 45% of absorbed laser power, at higher power losses were lower. They obtained experimental results for material removal rates and groove shapes on silicon nitride, which were found to agree well with theoretical predictions for shallow grooves.

Bang et al [62] analyzed theoretically the beam guiding effects during laser machining for ceramics due to multiple reflections in the groove for two extreme cases—-purely specular and purely diffuse reflections. Specular reflections were valid for materials that had a smooth surface during laser evaporation (small optical roughness as compared to the laser wavelength). For such cases the material surface was divided into a number of rectangular patches using a bicubic surface representation method. The net radiative flux for these patch elements was obtained by ray tracing methods. The resulting radiative flux due to specular reflections was combined with the three dimensional conduction equation governing conduction losses into the medium, and the resulting groove shape and depth were found through an iterative procedure. Diffuse reflections were valid for materials that had a very rough surface during material removal. To address beam coupling due to diffuse reflections, irradiation calculations employing view factor were combined with three-dimensional calculation model. Considering multiple reflections resulted in an increased absorptivity and deeper grooves, accompanied by a flatter profile near the centerline and

steeper slopes in the other parts of the groove cross-section. They predicted for the tested set of parameters, material removal rates were increased up to 40% by specular reflections and up to 70% by diffuse reflections. They compared their results with experiments, hot-pressed silicon nitride ceramic showed increased beam coupling for deeper grooves (high power and/or slow scanning speeds) as predicted by considering multiple reflections. The agreement between theoretical calculations and experimental data for material removal rate and groove shape was good, if multiple reflections were assumed to be diffuse.

Modest [63] developed a three-dimensional conduction model to predict the transient temperature distribution inside a thick solid that was irradiated by a moving laser source, and the changing shape of a groove carved into it by evaporation of material. The laser might operate in CW or in pulsed mode with arbitrary temporal as well as spatial intensity distribution. He solved the governing equations using a finite-difference method on an algebraically generated boundary-fitted coordinate system. He verified this transient model with three-dimensional codes that were limited to quasi-steady CW operation. He presented the groove shapes and temperature distribution, as well as their transient development, for various machining conditions, demonstrating the differences in the ablation process between CW, pulsed and Q-switched (or other pulses of extremely short duration) laser operation. The results showed that during short-pulsed laser ablation conduction losses were essentially negligible, resulting in substantially larger removal rates than for CW operation. Ablation with normally pulsed lasers, on the other hand, resulted in removal rates,

which approached those of a Q-switched laser, but the thickness of the heat-affected layer was much larger, approaching that of the CW laser. The calculation further indicated that, during short-pulsed laser ablation, the material cooled off rapidly after the end of the pulse, returning to ambient conditions well before the beginning of the subsequent pulse.

Modest [64] developed a model of full three-dimensional transient through-cutting in thin sheets. He also developed a two-dimensional axisymmetric version to model and predict results for drilling. He solved three-dimensional conduction equation numerically using boundary-fitted coordinates. Using his model he found that under all circumstances even the maximum possible convection and radiation losses could have only a negligible effect on temperature and groove development.

Yilbas and Yilbas [65] studied the interaction mechanism of vapor generated by laser beam over the surface of work piece. The vapor heated the work piece surface and absorbed some fraction of incident energy. They developed a computer program to model gas dynamic equations in one-dimension with additional terms for absorption of laser beam, radiation losses and conduction. They assumed that vapor was comprised of heavy particles and free electrons, each species behaving as a perfect gas. They found that the evaluation of the expansion of vapor plug was sensitive to variations in initial conditions. The vapor temperature increased from initial value to 10000 K in 10^{-7}—10^{-6} sec after which further increment occurred relatively slowly. The leading edge of the vapor had velocity of the order of 4000-7000 m/s.

Yilbas et al [66] examined the absorption of a laser beam at different wavelengths

by a partially ionized vapor during the interaction mechanism. They distinguished the interaction of the high and low power laser beam with plasma. They showed that different metal vapors at similar temperatures and densities had absorption depths, which might differ by an order of magnitude. They also showed that the free electron temperature became significantly different from the heavy particle temperature for power intensities above critical level which was typically greater than 10^{14} W/m^2.

Wei and Ho [67] determined energy transfers and penetration velocity during a high-energy drilling or welding process. The beam energy of a Gaussian distribution incident on the free surface of a liquid layer that separated unmelted solid and vapor was balanced with the heat conduction and latent heats for melting and evaporation. They examined the effects of the beam power and the energy distribution on the high energy beam drilling. The normal pressure condition at the vapor-liquid interface was used to determine the shape of the vapor-liquid interface. The heat conduction in both the axial and radial directions, heat of evaporation and melting were taken into account. The fusion line, however, was calculated by using the enthalpy method. They developed a quasi-steady, axisymmetric heat conduction model to investigate the penetrating process of the cavity produced by high energy beam. The shape of the fusion zone and the penetration velocity were determined as a function of energy distribution parameters and the beam power, rather than specified a priori. They showed that the energy distribution parameter had stronger effects than the beam power on the high-energy beam drilling or welding process. The penetration velocity increased with increasing beam power or decreasing energy distribution parameter.

Increasing the energy flux resulted in a slight increase in radial conduction loss. Since the sensible heat of raising the liquid from the melting temperature to the base temperature was small, the energy transferred to the liquid-solid interface became larger for a higher energy flux. This resulted in a non-linear and significant increase in the penetration velocity at a high beam power or a small energy distribution parameter. High temperature occurred near the cavity base.

Ganesh et al [68, 69] developed a comprehensive model to study the laser drilling process and used volume of flow technique to track the position of moving vapor front and recession of surface.

Zhang and Faghri [70] investigated the melting and vaporization phenomena during the laser drilling process. The locations of the solid-liquid and liquid-vapor interfaces were obtained by solving energy conservation equations at interfaces. The dependence of saturation temperature on the back pressure was taken into account by using the Clausius/Clapeyron equation. They also included the conduction heat loss to the work piece and solved it using an integral approximation method. The predicted material removal rate agreed well with the experimental data. The amount of heat loss through conduction was found to be very small and its effect on the vaporization was not significant. However, the location of melting front was significantly affected by conduction heat loss especially for lower laser intensity and longer pulse. The existence of sub-cooling in the solid was helpful in reducing the thickness of recast layer.

A two-step gas-dynamic model of laser ablation in an ambient gas atmosphere

was proposed by Gusarov et al [71]. The initial one dimensional stage was related to obtain plume formation and described heating, melting and evaporation of the target, the target-vapor interaction in the boundary layer, and vapor dynamics. The final two-dimensional stage was responsible for the formation of energy and angular distributions of the ablated material. Interaction between the vapor and ambient gas was taken into account by two-component gas-dynamic equations. Numerical analysis of laser ablation in ambient gas atmosphere and the analysis revealed that both kinetic energy of ablated atoms and width of their angular distribution deceased with ambient pressure. They compared the dynamics of ablated material expansion and its energy distribution with the experiment.

Kar et al [72] developed a simple mathematical model for the cutting of thick-section stainless steel using a high power chemical oxygen iodine laser. The model was based on an overall energy balance, and it related the cutting depth with various process parameters that could be used to predictively scale the laser materials processing performance to very thick sections. They examined the effects of absorptivity and the velocity of the cutting gas jet on the kerf depth and width. The study indicated that thick metal cutting performance might be improved by producing narrow kerf widths. The scaling law for cut depth per unit power closely agreed with the experimental data at low cutting speeds since it was obtained by assuming a large conduction heat loss that held good at low cutting speeds. The laser-plume interaction and effective absorptivity played an important role in the cutting performance of a laser beam.

Semak and Matsunawa [73] carried out a theoretical analysis of the energy balance

in the laser-metal interaction zone. They considered the heat transfer due to the recoil-pressure-induced melt flow. The results of numerical simulations showed the recoil pressure play a significant role in ejection of the melt from the interaction zone even for low melt surface temperatures close to the melting point. High-velocity melt flow was generated in the interaction zone for beam intensities typically used in laser cutting/welding; thus, the melt-flow pattern could not be considered as the motion of a cylinder in an infinite liquid pool. Under typical industrial cutting/welding conditions about 70-90% of laser intensity absorbed in the beam interaction zone was carried away from the interaction zone by the metal flow; thus, the convection-related terms could not be ignored neither in calculations of the energy balance in the interaction zone nor in calculations of the thermal field in the weld pool or in the vicinity of the cutting front. The velocity of the keyhole-wall front or cutting front was determined by the absorbed laser intensity and could be either smaller or higher than the beam's translation velocity.

Chapter 3

MATHEMATICAL MODELLING

3.1 Mean-Flow Equations

In the present study two cases are considered; *i*) a high temperature air/helium jet and *ii*) a high temperature helium jet and the opposing air jet at ambient temperature is/are entering the initially stagnant and air ambient. Consequently, a mixture of helium and air is formed, which is denoted as He-air mixture. Moreover, the gas mixture in the present study is considered non-reacting and the resulting flow field is compressible, unsteady, two-dimensional, axisymmetric and turbulent. The governing *Favre-Averaged Transport Equations* can be given in the following form [26, 28, 74]:

Continuity Equation:

$$\frac{\partial \overline{\rho}}{\partial t} + \frac{\partial}{\partial x_j}(\overline{\rho}\widetilde{u}_j) = 0 \tag{3.1}$$

Species Continuity Equation:

$$\frac{\partial}{\partial t}(\overline{\rho}\widetilde{Y}_i) + \frac{\partial}{\partial x_j}(\overline{\rho}\widetilde{u}_j\widetilde{Y}_i) = \frac{\partial}{\partial x_j}\left\{\left(\overline{\rho}D_{im}\frac{\partial \widetilde{Y}_i}{\partial x_j} - \overline{\rho u_j'' Y_i''}\right)\right\} + \overline{R}_i \tag{3.2}$$

Where $\widetilde{Y}_i$ is the Favre-averaged mass fraction of the i^{th} species (here including three

species: helium (He), nitrogen (N_2) and oxygen (O_2) for He-air non-reacting mixture); D_{im} is the diffusion coefficient of the i^{th} species in the mixture; $\overline{R}$ is the net rate of creation of the i^{th} species due to chemical reaction, which is neglected here for non-reacting gaseous mixture. The above Eq. (3.2) is not required for single species (air jet into ambient air).

Momentum Equation:

$$\frac{\partial}{\partial t}(\overline{\rho}\widetilde{u}_i) + \frac{\partial}{\partial x_j}(\overline{\rho}\widetilde{u}_j\widetilde{u}_i) = -\frac{\partial \overline{p}}{\partial x_i} + \frac{\partial}{\partial x_j}\left[(\overline{\tau}_{ij} - \overline{\rho u_j'' u_i''})\right] \tag{3.3}$$

Where $\overline{\tau}_{ij}$ is a time-averaged stress tensor and is given as:

$$\overline{\tau}_{ij} = \overline{\mu\left(\frac{\partial u_i}{\partial x_j} + \frac{\partial u_j}{\partial x_i}\right) - \frac{2}{3}\mu\frac{\partial u_k}{\partial x_k}\delta_{ij}} \tag{3.4}$$

Energy Equation:

$$\begin{aligned} & \frac{\partial}{\partial t}(\overline{\rho}E) + \frac{\partial}{\partial x_j}(\overline{\rho}\widetilde{u}_j H) \\ = \; & \frac{\partial}{\partial x_j}\left[\left(\frac{\mu}{\sigma}\right)\left(\frac{\partial \widetilde{h}}{\partial x_j}\right) - \overline{\rho u_j'' h''}\right] + \frac{\partial}{\partial x_j}\left[\widetilde{u}_i\left(\overline{\tau}_{ij} - \overline{\rho u_i'' u_j''}\right)\right] \\ & + \frac{\partial}{\partial x_j}\left\{\sum_{k=1}^{N_s}\widetilde{h}_k\left[\left(\overline{\rho}D_{km} - \frac{\mu}{\sigma}\right)\frac{\partial \widetilde{Y}_k}{\partial x_j} + \left(\overline{\rho u_j'' h''}\left(\frac{\frac{\partial \widetilde{Y}_k}{\partial x_j}}{\frac{\partial \widetilde{h}}{\partial x_j}}\right) - \overline{\rho u_j'' Y_k''}\right)\right]\right\} \\ & + \overline{S_h} \end{aligned} \tag{3.5}$$

Where $N_s(=3)$ is the total number of species in the gas mixture. The quantities E and H are the total specific internal energy and total specific enthalpy of a mixture

which include the kinetic energy of the fluctuating turbulent field known as *Turbulence Kinetic Energy (k)*, i.e.,

$$E = \widetilde{e} + \frac{1}{2}\widetilde{u}_i\widetilde{u}_i + k \tag{3.6}$$

$$H = \widetilde{h} + \frac{1}{2}\widetilde{u}_i\widetilde{u}_i + k \tag{3.7}$$

Where $\widetilde{e}$ and $\widetilde{h}$ are the Favre-averaged specific internal energy and Favre-averaged specific enthalpy of a mixture respectively, which are given by:

$$\widetilde{e} = c_v\widetilde{T} \tag{3.8}$$

$$\widetilde{h} = c_p\widetilde{T} = \widetilde{e} + \frac{\overline{p}}{\overline{\rho}} \tag{3.9}$$

Where c_v and c_p are the specific heat of the mixture at constant volume and constant pressure respectively. Eq. (3.5) is valid for $k \ll \widetilde{h}$.

Sensible enthalpy for ideal gas mixture (compressible) is given as [26, 28]:

$$\widetilde{h} = \sum_{k=1}^{N_s} \widetilde{Y}_k\widetilde{h}_k \tag{3.10}$$

Where $\widetilde{h}_k$ is the specific enthalpy of the k^{th} species and is given as:

$$\widetilde{h}_k = h_k^o + \int_{T_{ref.}}^{T} c_{p_k} dT \tag{3.11}$$

Where T_{ref} $(= 298.15\ K)$ is the mixture reference temperature, c_{p_k} is the specific

heat at constant pressure for the k^{th} species and h_k^o is the specific enthalpy of the k^{th} species at T_{ref}.

The first three terms on the right hand side of Eq. (3.5) represent energy transfer due to conduction, viscous dissipation and species diffusion respectively. Moreover, the last term on the right hand side of Eq. (3.5) is the time-average source term (neglected in the present study for non-reacting gaseous mixture with no heat generation due to any cause), which may be due to chemical reaction and/or any other defined cause. In case of single species (air jet into ambient air), the species diffusion term will be neglected. Furthermore, there is no need of Eqs. (3.10) & (3.11) in this case.

State Equation:

$$\overline{p} = \overline{\rho} R \widetilde{T} \tag{3.12}$$

Where R is a gas constant.

3.2 Turbulence Equations

3.2.1 Eddy-Viscosity and Eddy-Diffusivity Concept

The term $-\overline{\rho u_i'' u_j''}$ in Eqs. (3.3) & (3.5) are *Favre-Averaged-Reynolds Stresses*. It was proposed by Boussinesq that modelling these stresses may be performed by analogy with viscous stresses in laminar flows, i.e., these stresses like viscous stresses

can also be put in the following form [74]:

$$-\overline{\rho u_i'' u_j''} = \mu_t \left(\frac{\partial \widetilde{u}_i}{\partial x_j} + \frac{\partial \widetilde{u}_j}{\partial x_i} \right) - \frac{2}{3} \left(\mu_t \frac{\partial \widetilde{u}_k}{\partial x_k} + \overline{\rho} k \right) \delta_{ij} \tag{3.13}$$

By analogy with Favre-averaged-Reynolds stresses, $-\overline{\rho u_j'' Y_i''}$ in Eqs. (3.2) & (3.5) and $-\overline{\rho u_j'' h''}$ in Eq. (3.5) are respectively the turbulent transport of i^{th} species and turbulent transport of enthalpy and are given in their respective order by:

$$-\overline{\rho u_j'' Y_i''} = \frac{\mu_t}{\sigma_{\widetilde{Y}}} \left(\frac{\partial \widetilde{Y_i}}{\partial x_j} \right) \tag{3.14}$$

$$-\overline{\rho u_j'' h''} = \frac{\mu_t}{\sigma_t} \left(\frac{\partial \widetilde{h}}{\partial x_j} \right) \tag{3.15}$$

Where σ_t, $\sigma_{\widetilde{Y}}$ and μ_t are turbulent Prandtl number, turbulent Schmidt number and eddy viscosity of a mixture respectively. The ratios $\frac{\mu_t}{\sigma_{\widetilde{Y}}}$ and $\frac{\mu_t}{\sigma_t}$, by analogy with eddy viscosity, are eddy mass diffusivity and eddy thermal diffusivity. Since turbulent transport of momentum and scalar property (enthalpy/mass fraction) are due to the same mechanism—eddy mixing— it is expected that the value of eddy thermal diffusivity and eddy mass diffusivity are close to that of the eddy viscosity [75]. The turbulent viscosity, μ_t, can be defined by the following relation [76]:

$$\mu_t = C_\mu \overline{\rho} k^2 / \epsilon \tag{3.16}$$

Where C_μ is an empirical constant, k is the *Turbulence Kinetic Energy* and ϵ is the *Turbulence Dissipation Rate.* These turbulence quantities may be computed by *the standard $k-\epsilon$ model.*

3.2.2 The Standard $k-\epsilon$ Model

The conservation equations for the turbulence kinetic energy (k) and its dissipation rate (ϵ) are modelled in the standard $k-\epsilon$ model. The modelled equation for the *Turbulence Kinetic Energy (k)* is given by:

$$\frac{\partial}{\partial t}(\overline{\rho}k) + \frac{\partial}{\partial x_j}(\overline{\rho}\widetilde{u}_j k) = \frac{\partial}{\partial x_j}\left[(\frac{\mu_t}{\sigma_k})\frac{\partial k}{\partial x_j}\right] + G - \overline{\rho}\epsilon + PD \tag{3.17}$$

and the modelled equation for the *Energy Dissipation (ϵ)* is given by:

$$\frac{\partial}{\partial t}(\overline{\rho}\epsilon) + \frac{\partial}{\partial x_j}(\overline{\rho}\widetilde{u}_j \epsilon) = \frac{\partial}{\partial x_j}\left[(\frac{\mu_t}{\sigma_\epsilon})\frac{\partial \epsilon}{\partial x_j}\right] + C_1\frac{\epsilon}{k}(G + PD) - C_2\overline{\rho}\frac{\epsilon^2}{k} \tag{3.18}$$

Where G is the rate of generation of turbulence kinetic energy, $\rho\epsilon$ is its destruction rate and PD is the pressure-dilatation which is due to the compressibility effect. G and PD are approximated respectively by the following relationships [74]:

$$G = -\overline{\rho u_i'' u_j''}\frac{\partial \widetilde{u}_i}{\partial x_j} \tag{3.19}$$

$$PD = \alpha_1\overline{\rho}\left(-\overline{\rho u_i'' u_j''}\right)\left(\frac{\partial \widetilde{u}_i}{\partial x_j}\right)M_t + \alpha_2\overline{\rho}\epsilon M_t^2 \tag{3.20}$$

Where the values of α_1 and α_2 (closure constants) are 0.15 and 0.2 respectively and M_t is the turbulence Mach number which is defined as:

$$M_t = \left(\frac{2k}{c^2}\right)^{1l2} \tag{3.21}$$

Where c is the speed of sound and is given as:

$$c = \left(\gamma R\widetilde{T}\right)^{1/2} \tag{3.22}$$

The standard $k-\epsilon$ model contains empirical constants which are assigned the following values:

C_μ	C_1	C_2	σ_k	σ_ϵ	σ_t	$\sigma_{\tilde{Y}}$
0.09	1.44	1.92	1.00	1.30	0.7	0.7

In general, the standard $k-\epsilon$ model is valid in regions where the flow is entirely turbulent. Close to the solid walls, viscous effects become dominant and such a model does not lead to acceptable predictions. Therefore, either low Reynolds number model is used to solve the whole flow field or wall functions discussed in boundary conditions are used near solid walls with high Reynolds number model for rest of the flow domain.

3.2.3 Low Reynolds Number $k-\epsilon$ Model

The standard $k-\epsilon$ model is not applicable when low Reynolds number regime ($\mathrm{Re}_t < 100$) prevails. In this case, modifications to standard $k-\epsilon$ model make possible to cope with low Reynolds number flows. Wall damping is required to be

applied to ensure that viscous stresses take over from turbulent Reynolds stresses at low Reynolds numbers and in the viscous sublayer adjacent to solid walls. The equations of the low Reynolds number $k-\epsilon$ model, which replace Eq. (3.16) through Eq. (3.18), are given as:

$$\mu_t = C_\mu \overline{\rho} f_\mu k^2/\epsilon \tag{3.23}$$

$$\frac{\partial}{\partial t}(\overline{\rho}k) + \frac{\partial}{\partial x_j}(\overline{\rho}\widetilde{u}_j k) = \frac{\partial}{\partial x_j}\left[(\mu + \frac{\mu_t}{\sigma_k})\frac{\partial k}{\partial x_j}\right] + G - \overline{\rho}\epsilon + PD \tag{3.24}$$

$$\frac{\partial}{\partial t}(\overline{\rho}\epsilon) + \frac{\partial}{\partial x_j}(\overline{\rho}\widetilde{u}_j \epsilon) = \frac{\partial}{\partial x_j}\left[(\mu + \frac{\mu_t}{\sigma_\epsilon})\frac{\partial \epsilon}{\partial x_j}\right] + f_1 C_1 \frac{\epsilon}{k}(G + PD) - f_2 C_2 \overline{\rho}\frac{\epsilon^2}{k} \tag{3.25}$$

The most obvious modifications, which is universally made, is to include a viscous contribution in the diffusion terms in Eq. (3.23) through Eq. (3.25). The constants C_μ, C_1 and C_2 in the standard $k-\epsilon$ model are multiplied by wall-damping functions, f_μ, f_1 and f_2 respectively. These functions may be given by Lam and Bremhorst wall damping functions [77]:

$$f_\mu = [1 - \exp(-0.0165\,\mathrm{Re}_{x_i})]^2 \left(1 + \frac{20.5}{\mathrm{Re}_t}\right) \tag{3.26}$$

$$f_1 = \left(1 + \frac{0.05}{f_\mu}\right)^3 \tag{3.27}$$

$$f_2 = 1 - \exp(-\mathrm{Re}_t^2) \tag{3.28}$$

Where

$$\mathrm{Re}_{x_i} = k^{1/2} x_i/\nu; \qquad \mathrm{Re}_t = \vartheta l/\nu = k^2/(\nu\epsilon) \tag{3.29}$$

3.3 Solution Domains

There are two cases to be dealt with here in the present study and both of them have separate boundary details. These include:

- Free transient turbulent gas jet.
- Unsteady opposing jets.

3.3.1 Free Transient Turbulent jet

The solution domain of transient turbulent gas (air/helium) jet emanating from the inlet and emerging into the initially stationary air surrounding is shown in Figure 3.1. The solution domain is rectangular with 30 d in the axial direction and 15 d in the radial direction.

3.3.1.1 Boundary Details

The solution domain consists of the following boundaries:

- *Inlet:* This is the physical boundary through which the vapors resembling the laser-produced vapor emanate into the initially quiescent air surrounding. This region ranges 0 $m \leq r \leq 0.000522$ m at $x = 0$ m.
- *Outlet (Pressure Outlet):* At the right extreme in Fig. 3.1 there is a pressure

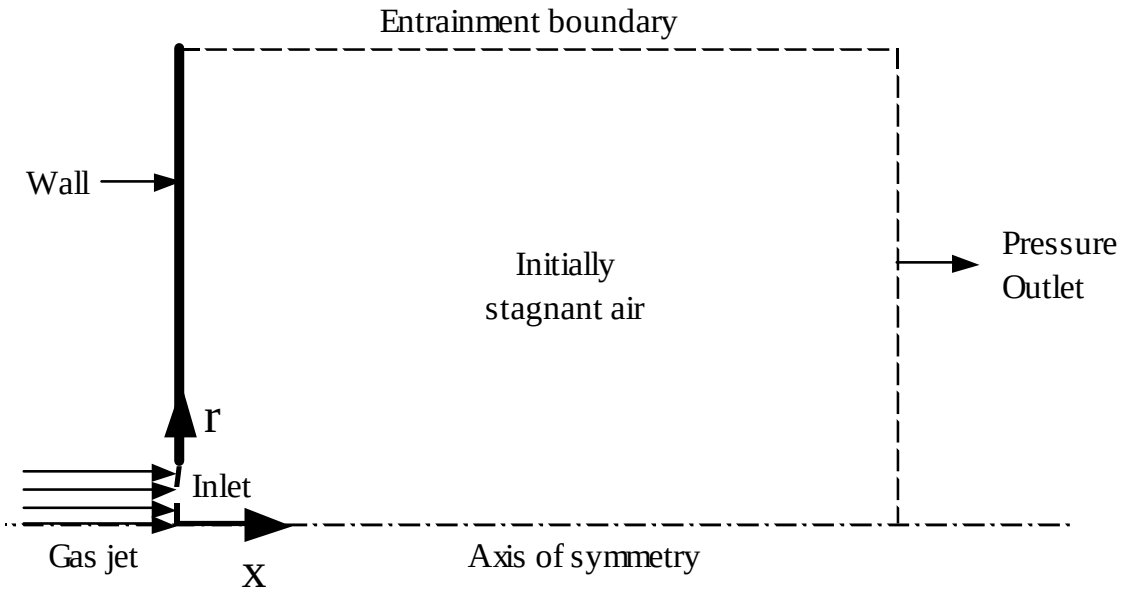

Figure 3.1: The solution domain of an axisymmetric transient turbulent air/helium jet emanating from the inlet and emerging into initially stagnant air.

boundary, which behaves like an outlet, through which the jet leaves the domain. It ranges 0 $m \leq r \leq 0.02$ m at $x = 0.03$ m.

• *Entrainment Boundary:* At the upper extreme in Fig. 3.1 there is an entrainment boundary through which the stagnant ambient air is entrained into the domain such that it moves along with the jet due to the friction between the jet edge and the stagnant ambient air. It ranges 0 $m \leq x \leq 0.03$ m at $r = 0.02$ m.

• *Symmetry Axis:* The domain has the axisymmetric boundary that ranges 0 $m \leq x \leq 0.03$ m at $r = 0$ m.

• *Wall:* This is the surface of the work-piece and it ranges 0.000522 $m \leq r \leq 0.02$ m at $x = 0$ m.

3.3.2 Unsteady Opposing Jets

The solution domain of transient turbulent helium jet emanating from inlet 1 and interacting with the opposing steady air jet issuing from inlet 2 is shown in Figure 3.2. The solution domain is 40 d in the axial direction and 50 d in the radial direction.

3.3.2.1 Boundary Details

The solution domain consists of the following boundaries:

• *Inlet 1:* This is the physical boundary through which helium vapors resembling the laser-produced vapor emanate and interact with the opposing steady air jet, which ensues from inlet 2. This region ranges 0 $m \leq r \leq 0.000522$ m at $x = 0$ m.

• *Inlet 2:* This is the physical boundary through which the steady air jet emanates

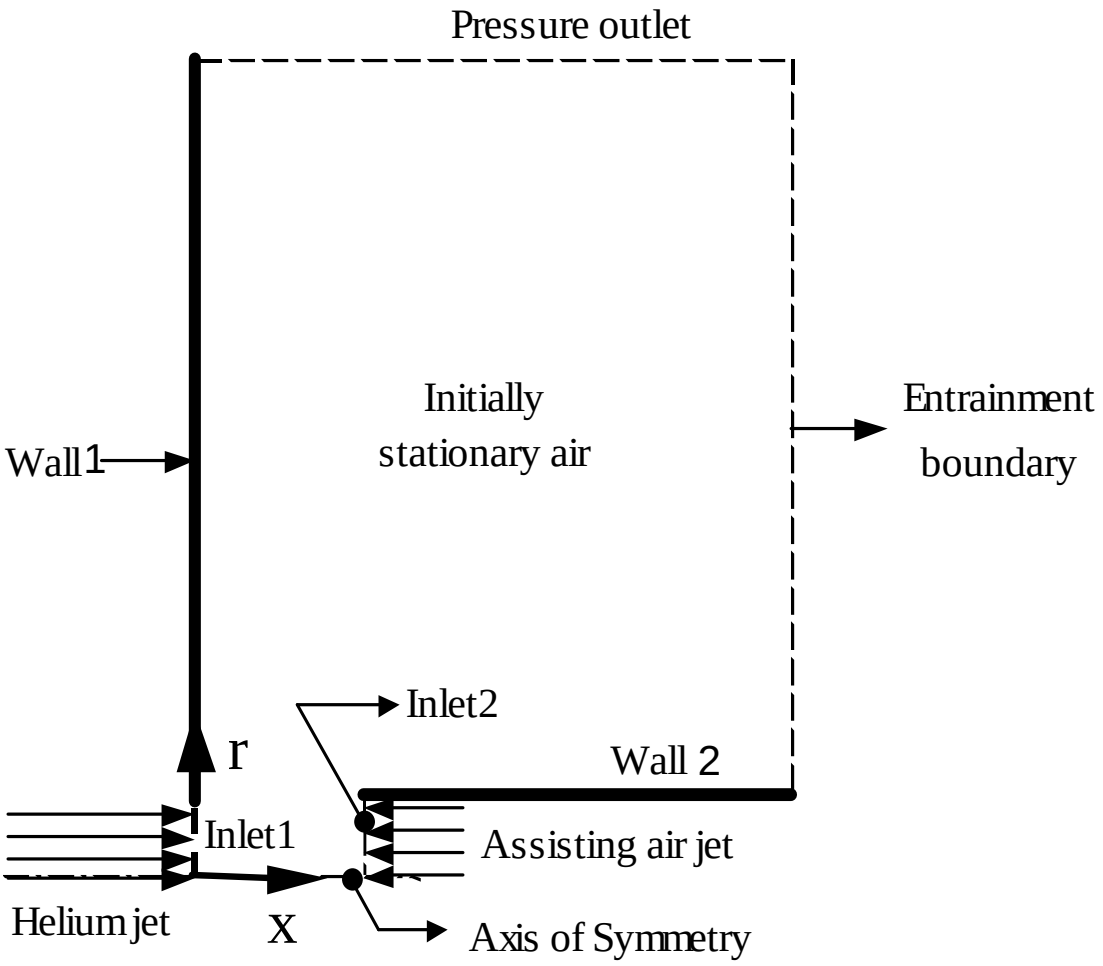

Figure 3.2: The solution domain of a transiently developing helium jet emanating from inlet 1 and opposing the steady air jet emanating from inlet 2.

and interacts with the opposing transient helium jet, which ensues from inlet 1. This region ranges 0 $m \leq r \leq 0.000522$ m at $x = 0.002$ m.

- *Outlet (Pressure Outlet):* At the upper extreme in Fig. 3.2 there is a pressure boundary, which behaves as an outlet, through which the two jets after interaction leave the domain. It ranges 0 $m \leq x \leq 0.04$ m at $r = 0.05$ m.

- *Entrainment Boundary:* At the right extreme in Fig. 3.2 there is an entrainment boundary through which the stagnant ambient air is entrained into the domain such that it moves along with the flow due to the friction between the edge of the flow and the stagnant ambient air. It ranges 0.000522 $m \leq r \leq 0.05$ m at $x = 0.04$ m.

- *Symmetry Axis:* The domain has the axisymmetric boundary that ranges 0 $m \leq x \leq 0.002$ m at $r = 0$ m.

- *Wall 1:* This is the surface of the work-piece and it ranges 0.000522 $m \leq r \leq 0.05$ m at $x = 0$ m.

- *Wall 2:* This is the wall of the tube through which the assisting air emanates and it ranges 0.002 $m \leq x \leq 0.04$ m at $r = 0.000522$ m.

3.4 Boundary Conditions

With reference to Figures 3.1 & 3.2, five boundary conditions need to be considered, including: *gas inlet, unbounded air outlet (pressure boundary), symmetry axis, entrainment boundary, and the solid wall.* These are given as follows:

3.4.1 Inlet Conditions

3.4.1.1 Transient Jet Inlet (Inlet 1)

The velocity profile at the control volume inlet varies spatially and temporarily due to the resembling of the vapor front velocity generated during the laser heating process. Therefore, the velocity profiles obtained from a previous study [78] are employed at the inlet boundary. Since, the emerging jet is involved with a compressible flow, a mass flux (mass flow rate per unit area) is considered at the inlet, i.e.,

$$\dot{m}_{in} = \overline{\rho} u_{in} = \overline{\rho} u_o \left(1 - \frac{r}{r_o}\right)^n \qquad 0 \le r \le r_o \tag{3.30}$$

Where u_o, r_o and n are functions of time (t) and are given as:

$$u_o = -3 \times 10^8 \times t^2 - 215718 \times t + 131.25 \qquad 0\mu s \le t \le 376.92\mu s \tag{3.31}$$

$$r_o = \begin{cases} 444470 \times t^2 - 0.684 \times t + 10^{-4} & 0\mu s \le t \le 23.07\mu s \\ 0.000522 & 30.76\mu s \le t \le 353.84\mu s \\ 50055 \times t^2 - 29.165 \times t + 0.0035 & 361.53\mu s \le t \le 376.92\mu s \end{cases} \tag{3.32}$$

$$n = 2 \times 10^7 \times t^2 - 7693.1 \times t + 0.9473 \qquad 0\mu s \le t \le 376.92\mu s \tag{3.33}$$

In order to resemble the high temperature of the evaporating surface, the emerging jet temperature is considered as 1500 K and remains constant, i.e.,

$$\widetilde{T} = T_{in}\ (1500\ K)$$

Since the jet at the inlet to control volume consists of helium only, the mass fraction of helium is given as:

$$\widetilde{Y}_{He} = 1.0$$

Values of k and ϵ are not known at the inlet, but some reasonable assumptions can be made. Applying the assumption of local equilibrium (rates of production and dissipation are both in balance) at the inlet gives the following relationships [76, 79]:

$$k_{in} = \frac{1}{\mathrm{C}_\mu} l_m^2 \left(\frac{\partial u_{in}}{\partial r}\right) \tag{3.34}$$

$$\epsilon_{in} = \mathrm{C}_\mu^{1/2} k \left|\frac{\partial u_{in}}{\partial r}\right| \tag{3.35}$$

Where l_m is the mixing length and is given by the following *Nikuradse Formula* [76,79]:

$$\frac{l_m}{r_o} = 0.14 - 0.08\left(\frac{r}{r_o}\right)^2 - 0.06\left(\frac{r}{r_o}\right)^4 \qquad 0 \le r \le r_o \tag{3.36}$$

The radial velocity component (v_{in}) at this inlet is set to zero.

3.4.1.2 Steady Air Jet Inlet (Inlet 2)

The assisting gas jet impinging onto the transiently developing jet, resembling the laser produced vapor jet, is a steady jet and obeys $\frac{1}{7}$ power law. Therefore. the mass flux at this inlet is given by:

$$\dot{m}_{in} = \overline{\rho} u_{in} = \overline{\rho} u_o \left(1 - \frac{r}{r_o}\right)^{1/7} \qquad 0 \leq r \leq r_o \tag{3.37}$$

Where u_o and r_o are independent of time at this inlet.

The assisting gas jet temperature is considered as 300 K and remains constant, i.e.,

$$\widetilde{T} = T_{in}\ (300\ K)$$

Since the assisting gas jet is forcing against the transient jet resembling the vapor jet, the helium content will hardly reach there at inlet 2 and hence the following conditions for mass fraction are satisfied:

$$\widetilde{Y}_{N_2} = 0.77; \quad \& \quad \widetilde{Y}_{O_2} = 0.23$$

Values of k and ϵ are not known at the inlet, making similar assumptions as before

one can write:

$$k_{in} = \frac{1}{\mathrm{C}_\mu} l_m^2 \left(\frac{\partial u_{in}}{\partial r}\right) \tag{3.38}$$

$$\epsilon_{in} = \mathrm{C}_\mu^{1/2} k \left|\frac{\partial u_{in}}{\partial r}\right| \tag{3.39}$$

Where l_m is the mixing length and is given by the following *Nikuradse Formula*:

$$\frac{l_m}{r_o} = 0.14 - 0.08\left(\frac{r}{r_o}\right)^2 - 0.06\left(\frac{r}{r_o}\right)^4 \qquad 0 \le r \le r_o \tag{3.40}$$

The radial velocity component (v_{in}) at this inlet is set to zero.

3.4.2 Outlet (Pressure Boundary)

It is considered that the flow extends over a sufficiently long domain so that;

$$\overline{p} = p_{amb}; \qquad \widetilde{T} = T_{amb}; \qquad \widetilde{Y}_{N_2} = 0.77; \quad \& \quad \widetilde{Y}_{O_2} = 0.23$$

Zero values of turbulence properties (k and ϵ) and mean velocities ($\widetilde{u}$ & $\widetilde{\mathrm{v}}$) are used.

3.4.3 Entrainment Boundary

The pressure and temperature at this boundary are the same as ambient condition. Zero values of turbulence properties (k and ϵ) and mean-velocity gradients

$\left(\frac{\partial \widetilde{u}_i}{\partial x_j}\right)$ are used [7, 75]. However, the boundary is far enough to satisfy the following conditions for mass fraction:

$$\widetilde{Y}_{N_2} = 0.77; \quad \& \quad \widetilde{Y}_{O_2} = 0.23$$

3.4.4 Symmetry Axis

Here the radial derivatives for all mean variables $\left(\frac{\partial \phi}{\partial r}\right)$ except the radial velocity ($\widetilde{\mathrm{v}} = 0$) are set to zero. Also $\frac{\partial k}{\partial r}$ and $\frac{\partial \epsilon}{\partial r}$ and are set to zero at the symmetry axis [7,75].

3.4.5 Solid Wall

3.4.5.1 The Standard $k - \epsilon$ Model

At a solid boundary the no-slip condition applies so that both mean and fluctuating velocities (u, v, u'', v'') as well as fluctuating temperature and fluctuating mass fraction (T'', Y_k'') are zero but the dissipation rate (ϵ) is finite. The equations need to be integrated through the viscous sublayer when the boundary conditions are specified at the wall. However, this process requires many grid points in the viscous sublayer because the velocity gradients are very sharp here and this means additional computational load. Furthermore, since the Eqs. (3.17) & (3.18) assume high Reynolds number (because the laminar viscosity (μ) is neglected from these equations), they are not applicable in the viscous sublayer where μ is not insignificant. Therefore, the *Universal Law of the Wall* is introduced to avoid integration in the viscous sublayer.

This law connects the wall conditions such as wall shear stress and heat flux, and temperature to the dependent variables just outside the viscous sublayer. This law gives the following logarithmic relationship between the resultant tangential velocity (u_p) and the dimensionless normal distance (y_p^+) from point p to the solid wall:

$$u_p = \frac{u_\tau}{\kappa} Ln(E_w y_p^+) \qquad\qquad 30 < \ y_p^+ \ < 500 \tag{3.41}$$

Where κ ($= 0.41$) is von Karman's constant, E_w ($= 9.8$ for smooth wall) is the wall roughness parameter and u_τ are the resultant friction velocity. u_τ and y_p^+ are given in their respective order by the following relations:

$$u_\tau = \left(\frac{\tau_w}{\overline{\rho}}\right)^{1/2} \tag{3.42}$$

$$y_p^+ = \frac{\overline{\rho}\tau_w y_p}{\mu} \tag{3.43}$$

Where y_p is the normal distance from point p to the solid wall and τ_w is the wall shear stress.

In addition, measurements of turbulence kinetic energy budgets indicate that the production of turbulence kinetic energy is equal to the dissipation in the log-law region (local equilibrium). Using this assumption and eddy-viscosity equation, Eq. (3.16), one can develop the following wall functions [75]:

$$k = \frac{u_\tau^2}{\sqrt{C_\mu}} \ , \qquad\qquad \epsilon = \frac{u_\tau^3}{\kappa y_p} \tag{3.44}$$

For heat transfer the universal near wall temperature distribution at high Reynolds number is used [75]:

$$T_p^+ = -\frac{(T_p - T_w)c_p\overline{\rho}u_\tau}{q_w} = \sigma_t \left[u^+ + P\left(\frac{\sigma}{\sigma_t}\right)\right] \tag{3.45}$$

Where T_p^+ is the dimensionless temperature at near wall point y_p, T_p is the temperature at near wall point y_p, T_w is the wall temperature, q_w is the wall heat flux, $u^+ \left(= \frac{u_p}{u_\tau}\right)$ is dimensionless resultant tangential velocity and P is the *Pee-Function*, a correction function dependent on the ratio of laminar to turbulent Prandtl numbers [75]. Similar to Eq. (3.45) there are laws available for species mass transfer, relating the mass flux at the wall to the difference between the mass fraction at the wall and the mass fraction just outside the viscous sublayer [80]. However, in the present study the wall is insulated with respect to species mass transfer, i.e.,

$$\frac{\partial \widetilde{Y_i}}{\partial x_j} = 0$$

3.4.5.2 Low Reynolds Number $k - \epsilon$ Model

At a solid boundary the no-slip condition applies so that both mean and fluctuating velocities (u, v, u'', v$''$) as well as fluctuating temperature and fluctuating mass fraction (T'', Y_k'') are zero. In the present study, the following conditions regarding the turbulence kinetic energy, the dissipation rate of turbulence kinetic energy and

species mass fraction are applied:

$$k = 0; \quad \frac{\partial \epsilon}{\partial x_j} = 0; \quad \& \quad \frac{\partial \widetilde{Y_i}}{\partial x_j} = 0$$

The solid wall is assumed to remain at constant temperature ($T_w = 400\ K$) with no radiation losses taken into account in the simulation. This condition is valid for both high and low Reynolds number models.

Boundary conditions associated with species mass fraction are not applicable to the transient air jet expanding into an initially stagnant air.

3.5 Initial Conditions

The initial conditions are imposed before the air/helium jet emerges into the control volume. Therefore, initially stagnant air at ambient temperature (300 K) and pressure (atmospheric pressure) is considered in the control volume. Moreover, the ambient air has no helium content initially.

3.6 Properties

The density of air is considered to vary according to the ideal gas law depending on the local pressure and temperature. The compressibility effect is accommodated during the simulations.

3.7 General Form of the Differential Equations

The general form of transport equation governing the flow examined herein is compactly represented by the following non-linear partial differential equation:

$$\frac{\partial}{\partial t}\left(\overline{\rho}\phi\right) + \frac{\partial}{\partial x_j}\left(\overline{\rho}\widetilde{u}_j\phi - \Gamma_\phi\frac{\partial\phi}{\partial x_j}\right) = \overline{S}_\phi \tag{3.46}$$

The purpose of writing all the transport equations in one compact form is to provide ease in numerical computation; in this case, only one transport equation rather than all will be sufficient to deal with while performing computation.

Chapter 4

NUMERICAL METHOD AND ALGORITHM

4.1 Introduction

In the previous chapter the mathematical modeling of turbulence to simulate the physics of the evaporation process in non-conduction limited laser heating process is described. This modeling process results in partial differential equations that do not yield an analytical solution due to mathematical complexities involved and hence some other methods of solution are required. To solve these equations numerical methods can be employed, which are able to handle the problem of any degree of complexity. A preliminary idea about the task of a numerical method can be obtained by considering a heat flow situation. A number of grids is drawn to cover the whole domain. With a sufficiently fine grid distribution, the complete distribution of the temperature can be expressed in terms of its values at neighboring grid points. Thus the task of the numerical method is to evaluate temperature at each grid point. In a numerical scheme, a set of algebraic equations is derived from the governing differential equations for the grid-point values of the temperature. The detail and

accuracy of the answer obtained depend mainly upon the proper selection of grids and time increments. But detail and accuracy somehow require computational effort (calculation time and computer memory). Hence, in developing a numerical scheme, the primary consideration is a trade-off between model detail and computational effort.

4.2 Numerical Method

Several techniques of numerical analysis exist. Among them most famous are finite difference, finite volume, finite element, spectral and pseudo-spectral methods. The finite volume technique is used in the present simulation for its simplicity and accuracy [81]. Before proceeding to the finite volume method, it is appropriate to define basic properties of numerical solutions that determine their level of accuracy. These properties include:

- *Convergence*
- *Consistency*
- *Stability*

Convergence is the property of a numerical method to produce a solution which approaches the exact solution as the grid spacing, control volume size or element size is reduced to zero.

Consistency is the property of a numerical method to produce systems of algebraic equations which can be demonstrated to be equivalent to the original governing partial differential equations as the grid spacing tends to zero.

Stability is associated with the growth or damping of errors as the numerical method proceeds and hence it describes whether or not the dependent variable is bounded. For transient analysis, the dependent variable is unstable if the solution oscillates with an amplitude that increases with time. If a technique is not stable even round-off errors in the initial data can cause wild oscillations or divergence.

Convergence is usually very difficult to establish theoretically and in practice *Lax's Theorem* is used, which states that for linear problems a necessary and sufficient condition for convergence is that the method is both consistent and stable. In *CFD* methods this theorem is of limited use since the governing equations are non-linear. In such problems consistency and stability are necessary conditions for convergence, but not sufficient.

The inability to prove conclusively that a numerical solution scheme is convergent is perhaps somewhat unsatisfying from a theoretical standpoint, but there is no need to be too concerned since the process of making the mesh spacing very close to zero is not feasible on computing machines with a finite representation of numbers. Round-off errors would swamp the solution long before a grid spacing of zero is actually reached. In *CFD*, there is a need of codes that produce physically realistic results with good accuracy in simulations with finite (sometimes quite coarse) grids. Patankar [81] has formulated rules which yield robust finite volume calculation schemes. The three crucial properties of robust methods include:

- *Conservativeness*
- *Boundedness*

- *Transportiveness*

Conservativeness is the property of a numerical scheme which is associated with the consistent expressions for fluxes of the fluid property through the cell faces of adjacent control volumes.

Boundedness is akin to stability and requires that in a linear problem without sources the solution is bounded by the maximum and minimum boundary values of the flow variable. Boundedness can be achieved by placing restrictions on the magnitude and signs of the coefficients of the algebraic equations. Although flow problems are non-linear it is important to study the boundedness of a finite volume scheme for closely related but linear, problems.

Finally all flow processes contain effects due to convection and diffusion. In diffusive phenomena, such as heat conduction, a change of temperature at one location affects the temperature in more or less equal measure in all directions around it. Convective phenomena involve influencing exclusively in the flow direction so that a point only experiences effects due to changes at upstream locations. *Transportiveness* must account for the directionality of influencing in terms of the relative strength of diffusion to convection.

Conservativeness, boundedness and transportiveness are now commonly accepted as alternatives for the more mathematically rigorous concepts of convergence, consistency and stability [75].

4.3 The Finite Volume Method

In this method, the calculation domain is divided into a number of non-overlapping control volumes such that there is one control volume surrounding each grid point. The differential equation is integrated over each control volume. Profiles (such as step-wise and piecewise-linear profiles), expressing the variation of field variable (temperature, pressure, velocity, species mass fraction, etc.) between the grid points, are used to evaluate the required integrals. The result is the discretization equation containing the values of field variable for a group of grid points. The discretization equation thus obtained in this manner expresses the conservation principle of the field variable for the finite control volume, just as the differential equation expresses it for an infinitesimal control volume.

4.3.1 Discretization

The finite difference counterpart of the general partial differential equation (3.46) is derived by supposing that each variable is enclosed in its own control volume and then by integrating the partial differential equation (3.46) over the control with some suitable assumption of field-variable profile within the control volume.

For the purpose of solution the flow domain is overlaid with a number of grids whose center points or nodes denote the location at which all variables except velocities are calculated. The latter are computed at locations midway between the two pressure points. Thus the normal velocity components are directly available at

the control volume faces, where they are needed for the scalar transport -convection-diffusion-computations. The nodes of a typical grid cluster for two dimensions are labeled as P, N, S, E, and W. This is shown in Figure 4.1.

The integration of each term in Eq. (3.46) can be obtained with reference to the control volume for a typical node P with its four nearest neighbors, N, S, E, and W, in the spatial domain and P_o in the time domain. The integration yields

$$\int_t^{t+\Delta t} \left\{ \int_{CV} \left(\frac{\partial}{\partial t} \left(\overline{\rho}\phi \right) - \overline{S}_\phi \right) d\forall + \oint_{CS} \left[\widehat{n}. \left(\overline{\rho}\widetilde{u}_j \phi - \Gamma_\phi grad\phi \right) \right] dA \right\} dt = 0 \qquad (4.1)$$

Divergence theorem gives

$$\int_t^{t+\Delta t} \left\{ \int_{CV} \left(\frac{\partial}{\partial t} \left(\overline{\rho}\phi \right) - \overline{S}_\phi \right) d\forall + \int_{CV} \left[\frac{\partial}{\partial x_j} \left(\overline{\rho}\widetilde{u}_j \phi - \Gamma_\phi \frac{\partial \phi}{\partial x_j} \right) \right] d\forall \right\} dt = 0 \qquad (4.2)$$

or

$$\int_t^{t+\Delta t} \left\{ \left(\frac{\partial}{\partial t} \left(\overline{\rho}\phi \right) - \overline{S}_\phi \right) \Delta\forall + \left[\left(\overline{\rho}\widetilde{u}_j \phi - \Gamma_\phi \frac{\partial \phi}{\partial x_j} \right) \Delta A_j \right]_{L_1}^{L_2} \right\} dt = 0 \qquad (4.3)$$

or

$$\int_t^{t+\Delta t} \left\{ \left(\frac{\partial}{\partial t} \left(\overline{\rho}\phi \right) - \overline{S}_\phi \right) \Delta\forall + \left[J_j \Delta A_j \right]_{L_1}^{L_2} \right\} dt = 0 \qquad (4.4)$$

Where L_1 denotes w or s, L_2 e or n and J_j the total flux (convection plus diffusion) across the face 'j'.

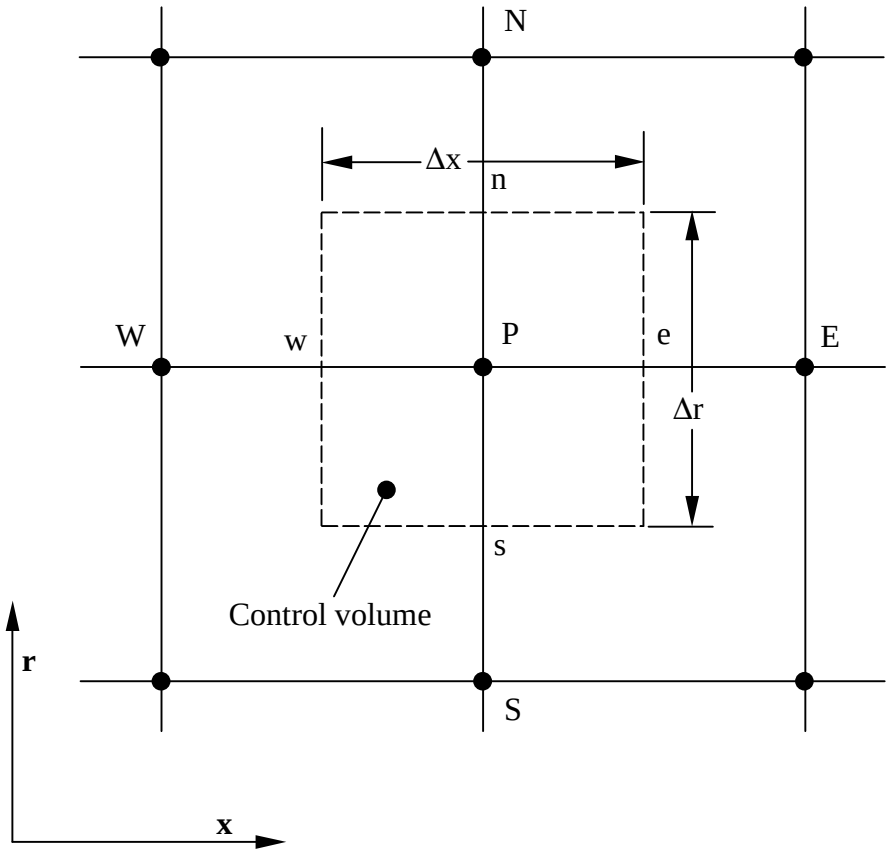

Figure 4.1: Control volume for the two-dimensional situation.

If $\overline{S}_\phi$ is independent of time then Eq. (4.4) becomes

$$\left[\frac{\overline{\rho}_P\phi_P - \overline{\rho}_P^o\phi_P^o}{\Delta t} - \overline{S}_\phi\right]\Delta\forall + J_e - J_w + J_n - J_s = 0 \tag{4.5}$$

Where J_e, J_w, J_n, and J_s are the integrated total fluxes over the control volume faces; i.e., J_e stands for $J_x\Delta A_x$ over the interface e, and so on. Where the superscript 'o' is used for old values (i.e., the values at previous time step).

The linearization of the source term gives

$$\overline{S}_\phi = S_o + S_P\phi_P \tag{4.6}$$

Now Eq. (4.5) becomes

$$\left(\frac{\overline{\rho}_P\phi_P - \overline{\rho}_P^o\phi_P^o}{\Delta t}\right)\Delta\forall + J_e - J_w + J_n - J_s = (S_o + S_P\phi_P)\,\Delta\forall \tag{4.7}$$

Now integration of the continuity equation (3.1) in a similar manner to Eq. (3.46) gives

$$\int_t^{t+\Delta t}\left\{\int_{CV}\left[\frac{\partial\overline{\rho}}{\partial t} + \frac{\partial}{\partial x_j}(\overline{\rho}\widetilde{u}_j)\right]d\forall\right\}dt = 0 \tag{4.8}$$

or

$$\int_t^{t+\Delta t}\left\{\frac{\partial\overline{\rho}}{\partial t}\Delta\forall + [\overline{\rho}\widetilde{u}_j\Delta A_j]_{L_1}^{L_2}\right\}dt = 0 \tag{4.9}$$

or

$$\int_t^{t+\Delta t} \left\{ \frac{\partial \overline{\rho}}{\partial t} \Delta \forall + [F_j \Delta A_j]_{L_1}^{L_2} \right\} dt = 0 \tag{4.10}$$

or

$$\left(\frac{\overline{\rho}_P - \overline{\rho}_P^o}{\Delta t} \right) \Delta \forall + F_e - F_w + F_n - F_s = 0 \tag{4.11}$$

Where F_j is the mass flux through the face 'j'; F_e, F_w, F_n, and F_s are the mass flow rates through the faces of the control volume; i.e., F_e stands for $F_x \Delta A_x$ over the interface e, and so on.

Multiplying Eq. (4.11) by ϕ_P, subtracting the resulting equation from Eq. (4.7) and knowing that;

$$J_e - F_e \phi_P = a_E(\phi_P - \phi_E) \tag{4.12}$$

$$J_w - F_w \phi_P = a_W(\phi_W - \phi_P) \tag{4.13}$$

$$J_n - F_n \phi_P = a_N(\phi_P - \phi_N) \tag{4.14}$$

$$J_s - F_s \phi_P = a_S(\phi_S - \phi_P) \tag{4.15}$$

one can develop the following algebraic equation [81]:

$$a_P \phi_P = a_E \phi_E + a_W \phi_W + a_N \phi_N + a_S \phi_S + b \tag{4.16}$$

Where

$$a_P = a_E + a_W + a_N + a_S + a_P^o - S_P \Delta\forall \tag{4.17}$$

$$\begin{aligned}
a_P^o &= \frac{\overline{\rho}_P^o \Delta\forall}{\Delta t} && (4.18)\\
b &= a_P^o \phi_P^o + S_o \Delta\forall && (4.19)\\
a_E &= D_e A(|P_e|) + [[-F_e, 0]] && (4.20)\\
a_W &= D_w A(|P_w|) + [[F_w, 0]] && (4.21)\\
a_N &= D_n A(|P_n|) + [[-F_n, 0]] && (4.22)\\
a_S &= D_s A(|P_s|) + [[F_s, 0]] && (4.23)
\end{aligned}$$

and P_e, P_w, P_n, and P_s are the Peclet numbers: i.e., P_e stands for $\frac{F_e}{D_e}$ and so on; D_e, D_w, D_n, and D_s are the diffusion conductances; i.e., D_e stands for $\frac{\Gamma_e \Delta y}{(\delta x)_e}$ and so on. The values of $A(|P|)$ are given in [81] for different schemes. In the present study, first order upwind scheme is employed for which $A(|P|)$ is unity.

Equation (4.16) is written for each of the variables, $\widetilde{u}$, $\widetilde{\mathrm{v}}$, k, ϵ, $\widetilde{\rho}$, $\widetilde{Y_i}$ and $\widetilde{T}$ at every cell. Although the control volumes adjacent to the boundary are treated differently from the interior ones and need different algebraic formulation, it is possible to have a unified formulation to calculate the field variable in the near boundary region through the use of source term [75].

4.4 Computation of the Flow Field

The solution of the general transport equation (3.46) presents two new problems:

- The convective term of Eq. (3.46) contains non-linear inertia terms.
- The continuity, momentum, energy, species and turbulence equations, represented by Eq. (3.46), are intricately coupled because every velocity component appearing in each equation. The most complex issue to resolve is the role played by pressure. It appears in the momentum equations, but there is evidently no transport equation for pressure.

If the pressure gradient is known, the process of obtaining and solving discretized equations for velocities from momentum equations is similar to that for any other scalar (e.g. temperature, species mass fraction, etc.) and developed schemes such as central differencing, upwind, hybrid schemes, etc. are applicable. In general purpose flow computations the pressure field is calculated as a part of the solution so its gradient is normally not known beforehand. If the flow is compressible the continuity equation may be used as a transport equation for density, and the pressure may be obtained from the density and temperature by using the equation of state. However, if the flow is incompressible the density is constant and hence by definition not linked to the pressure. In this case coupling between pressure and velocity introduces a constraint on the solution of the flow field: if the correct pressure field is applied in the momentum equations the resulting velocity field should satisfy continuity.

Both the problems associated with the non-linearities in Eq. (3.46) and the

pressure velocity linkage can be resolved by adopting an iterative solution strategy such as *SIMPLE (Semi-Implicit Method for Pressure-Linkage Equations)* algorithm of Patankar and Spalding [75].

Before outlining the algorithm it is very important to explain the grid staggering, which is the first step to the SIMPLE algorithm. The finite volume method starts, as always, with the discretization of the flow domain and of the general transport equation (3.46). First there is a need to decide where to store the velocities. It seems logical to define these at the same locations where the scalar variables, such as pressure, temperature etc., are defined. However, if the velocities and pressure are both defined at the nodes of an ordinary control volume, a highly non-uniform pressure field can act like a uniform field in the discretized momentum equations [75]. For instance, if velocities and pressure are both defined at the nodes of an ordinary control volume and the pressure gradient terms in the momentum equations are discretized by central differencing scheme in a uniformly discretized flow field, it is found that all the discretized pressure terms in axial and radial directions are zero at all nodal points even though the pressure field exhibits spatial oscillation in both directions of a two dimensional flow field [75]. As a result, this pressure field would give the same (zero) momentum source in the discretized equations as a uniform pressure field. This behavior is obviously non-physical.

It is clear that, if the velocities are defined at the scalar nodes (at which scalars, such as pressure and temperature, are defined), the influence of pressure is not properly represented in the discretized momentum equations. A remedy for this problem

is to use a staggered grid for the velocity components. The idea is to evaluate scalar variables, such as pressure, density, temperature, species concentration, turbulence kinetic energy and turbulence dissipation, at ordinary nodal points but to calculate velocity components on staggered grids centered around the cell faces. The arrangement for two-dimensional flow calculation with staggered grid arrangement is shown in Figure 4.2. In Figure 4.2 unbroken lines (grid lines) are numbered by means of capital letters $..., I-1, I, I+1, ...$ and $..., J-1, J, J+1, ...$ in the axial and radial directions respectively whereas the dashed lines that construct the scalar cell faces are denoted by lower case letters $..., i-1, i, i+1, ...$ and $..., j-1, j, j+1, ...$ in the axial and radial directions respectively. A subscript system based on this numbering allows us to define the locations of grid nodes and cell faces with precision. Scalar nodes, located at the intersection of two grid lines, are identified by two capital letters: e.g. point P in Figure 4.2 is denoted by (I, J). The axial velocities are stored at the e- and w-cell faces of a scalar control volume. These are located at the interaction of a line defining a cell boundary and a grid line and are, therefore, defined by a combination of a lower case letter and a capital: e.g. the w-face of the cell around point P is identified by (i, J). For the same reasons the storage locations for the radial velocities are combinations of a capital and a lower case letter: e.g. the s-face is given by (I, j).

The staggering of the velocity avoids the unrealistic behavior of the discretized momentum equation for spatially oscillating pressures. A further advantage of the staggered grid arrangement is that it generates velocities at exactly the locations

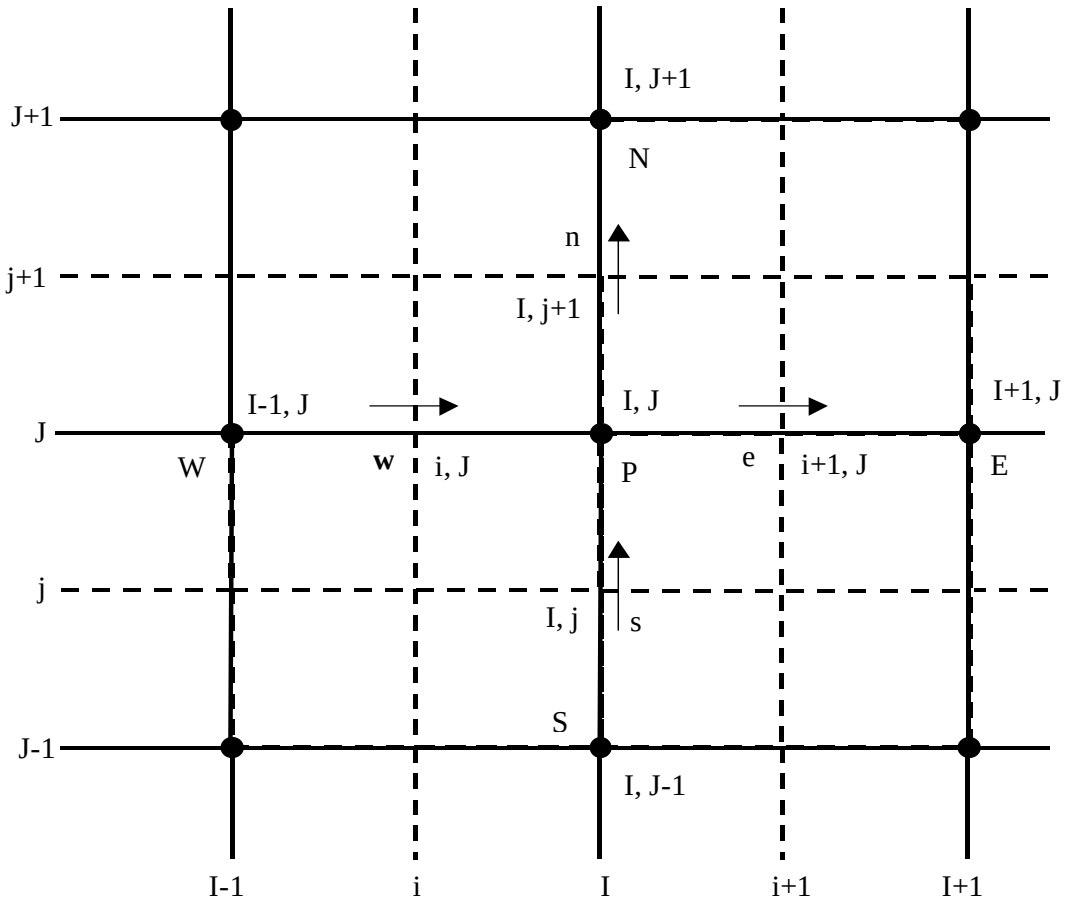

Figure 4.2: Staggered grid arrangement for velocity components.

where they are required for the scalar transport—convection-diffusion—computations. Hence, no interpolation is needed to calculate velocities at the scalar (eg. pressure and temperature) cell faces.

4.4.1 The SIMPLE Algorithm

The discretized momentum equations for $\widetilde{u}$ an $\widetilde{\mathrm{v}}$ using Eq. (4.16) are:

$$a_{i,J}\widetilde{u}_{i,J} = \Sigma a_{nb}\widetilde{u}'_{nb} + (\overline{p}_{I-1,J} - \overline{p}_{I,J})A_{i,J} + b_{i,J} \tag{4.24}$$

$$a_{I,j}\widetilde{\mathrm{v}}_{I,j} = \Sigma a_{nb}\widetilde{\mathrm{v}}'_{nb} + (\overline{p}_{I,J-1} - \overline{p}_{I,J})A_{I,j} + b_{I,j} \tag{4.25}$$

To initiate the *SIMPLE* calculation process the coefficients are calculated from the so-called guessed velocity components and then pressure field p^* is guessed [75]. Discretized momentum equations (4.24) and (4.25) are solved using the guessed pressure field to yield velocity components $\widetilde{u}^*$and $\widetilde{\mathrm{v}}^*$ as follows:

$$a_{i,J}\widetilde{u}^*_{i,J} = \Sigma a_{nb}\widetilde{u}^*_{nb} + (\overline{p}^*_{I-1,J} - \overline{p}^*_{I,J})A_{i,J} + b_{i,J} \tag{4.26}$$

$$a_{I,j}\widetilde{\mathrm{v}}^*_{I,j} = \Sigma a_{nb}\widetilde{\mathrm{v}}^*_{nb} + (\overline{p}^*_{I,J-1} - \overline{p}^*_{I,J})A_{I,j} + b_{I,j} \tag{4.27}$$

If $\overline{p}\,'$ is the correction pressure and $\overline{p}^*$ the guessed pressure then the correct pressure field $\overline{p}$ is:

$$\overline{p} = \overline{p}^* + \overline{p}\,' \tag{4.28}$$

Similarly if $\widetilde{u}'$ and $\widetilde{\mathrm{v}}'$ are the velocity corrections and $\widetilde{u}^*$ and $\widetilde{\mathrm{v}}^*$ the guessed velocities then the correct velocities $\widetilde{u}$ and $\widetilde{\mathrm{v}}$ are:

$$\widetilde{u} = \widetilde{u}^* + \widetilde{u}' \tag{4.29}$$

$$\widetilde{\mathrm{v}} = \widetilde{\mathrm{v}}^* + \widetilde{\mathrm{v}}' \tag{4.30}$$

After subtracting Eqs. (4.26) and (4.27) from (4.24) and (4.25) respectively, using correction formulae (4.28—4.30), omitting the terms $\Sigma a_{nb}\widetilde{u}'_{nb}$ and $\Sigma a_{nb}\widetilde{\mathrm{v}}'_{nb}$ from the equations resulting from subtraction and then using again Eqs. (4.29) and (4.30), the following expressions for correct velocities at nodes w (i, J) and s (I, j) are obtained:

$$\widetilde{u}_{i,J} = \widetilde{u}^*_{I,J} + d_{i,J}(\overline{p}'_{I-1,J} - \overline{p}'_{I,J}) \tag{4.31}$$

$$\widetilde{\mathrm{v}}_{I,j} = \widetilde{\mathrm{v}}^*_{I,J} + d_{I,j}(\overline{p}'_{I,J} - 1 - \overline{p}'_{I,J}) \tag{4.32}$$

Similar expressions for velocities $\widetilde{u}_{i+1,J}$ and $\widetilde{\mathrm{v}}_{I,j+1}$ exist:

$$\widetilde{u}_{i+1,J} = \widetilde{u}^*_{i+1,J} + d_{i+1,J}(\overline{p}'_{I,J} - \overline{p}'_{I+1,J}) \tag{4.33}$$

$$\widetilde{\mathrm{v}}_{I,j+1} = \widetilde{\mathrm{v}}^*_{I,j+1} + d_{I,j+1}(\overline{p}'_{I,J} - 1 - \overline{p}'_{I,J+1}) \tag{4.34}$$

Where

$$d_{i,J} = A_{i,J}/a_{i,J} \tag{4.35}$$

$$d_{I,j} = A_{I,j}/a_{I,j} \tag{4.36}$$

$$d_{i+1,J} = A_{i+1,J}/a_{i+1,J} \tag{4.37}$$

$$d_{I,j+1} = A_{I,j+1}/a_{I,j+1} \tag{4.38}$$

Using correct velocity in the discretized continuity equation, the following discretized equation for the pressure correction $\overline{p}\,'$ is obtained:

$$a_{I,J}\overline{p}'_{I,J} = a_{I+1,J}\overline{p}'_{I+1,J} + a_{I-1,J}\overline{p}'_{I-1,J} + a_{I,J+1}\overline{p}'_{I,J+1} + a_{I,J-1}\overline{p}'_{I,J-1} + b'_{I,J} \tag{4.39}$$

Where

$$a_{I,J} = a_{I+1,J} + a_{I-1,J} + a_{I,J+1} + a_{I,J-1} \tag{4.40}$$

$$a_{I+1,J} = (\overline{\rho}dA)_{i+1,J} \tag{4.41}$$

$$a_{I-1,J} = (\overline{\rho}dA)_{i,J} \tag{4.42}$$

$$a_{I,J+1} = (\overline{\rho}dA)_{I,j+1} \tag{4.43}$$

$$a_{I,J-1} = (\overline{\rho}dA)_{I,j} \tag{4.44}$$

$$b'_{I,J} = (\overline{\rho}\widetilde{u}^*A)_{i,J} - (\overline{\rho}\widetilde{u}^*A)_{i+1,J} + (\overline{\rho}\widetilde{\mathrm{v}}^*A)_{I,j} - (\overline{\rho}\widetilde{\mathrm{v}}^*A)_{I,j+1} \tag{4.45}$$

As soon as the starred velocity components are obtained the pressure correction

equation (4.39) is solved for $\overline{p}\,'$ at all scalar nodes. Once the pressure correction field is known, the correct pressure field may be obtained using formula (4.28) and correct velocity components through formulae (4.31—4.34).

Afterwards, the discretization equations for the scalar variables; such as temperature, species mass fraction, and turbulence quantities are solved if they influence the flow field through fluid properties, source terms, etc. If a particular scalar variable does not influence the flow field, it is better to calculate it after a converged solution for the flow field has been obtained.

If the solution is not converged the correct pressure $\overline{p}$ is treated as a new guessed $\overline{p}^*$ and the corrected velocity components as new guessed velocity components but not the starred values and the whole procedure is repeated as discussed above. This sequence of operation will be repeated over and over until a converged solution is obtained.

The pressure correction equation is susceptible to divergence [75] unless some under-relaxation is used during the iterative process, and new (improved) pressures $\overline{p}^{\,new}$ are obtained with

$$\overline{p}^{\,new} = \overline{p}^* + \alpha_{\overline{p}}\overline{p}\,' \tag{4.46}$$

Where $\alpha_{\overline{p}}$ is the pressure under-relaxation factor.

The velocities $\widetilde{u}^*$ and $\widetilde{\mathrm{v}}^*$, and $\widetilde{u}$ and $\widetilde{\mathrm{v}}$ are also under-relaxed as follows:

$$\widetilde{u}^{*\,new} = \alpha_{\widetilde{u}}\widetilde{u}^* + (1-\alpha_{\widetilde{u}})\widetilde{u}^{n-1} \tag{4.47}$$

$$\widetilde{\mathrm{v}}^{*\,new} = \alpha_{\widetilde{v}}\widetilde{\mathrm{v}} * + (1-\alpha_{\widetilde{v}})\widetilde{\mathrm{v}}^{n-1} \tag{4.48}$$

$$\widetilde{u}^{new} = \alpha_{\widetilde{u}}\widetilde{u} + (1-\alpha_{\widetilde{u}})\widetilde{u}^{n-1} \tag{4.49}$$

$$\widetilde{\mathrm{v}}^{new} = \alpha_{\widetilde{v}}\widetilde{\mathrm{v}} + (1-\alpha_{\widetilde{v}})\widetilde{\mathrm{v}}^{n-1} \tag{4.50}$$

$\alpha_{\widetilde{u}}$ and $\alpha_{\widetilde{v}}$ are under relaxation factors for x and y velocity components. $\widetilde{u}^*$ and $\widetilde{\mathrm{v}}^*$ are the velocity components obtained from solving the momentum equations (4.26) and (4.27) whereas $\widetilde{u}$ and $\widetilde{\mathrm{v}}$ are the corrected velocity components obtained from velocity correction formulae (4.31—4.34). $\widetilde{u}^{n-1}$ and $\widetilde{\mathrm{v}}^{n-1}$ are the velocity components obtained in the previous iteration.

The pressure correction equation is also affected by velocity under-relaxation and it can be shown that the d-terms of pressure correction equation (4.39) will be multiplied by the velocity under-relaxation. The second terms of the velocity correction formulae (4.31—4.34) will also be multiplied by the velocity under-relaxation.

The whole steps followed can be well described by the flow chart (Fig. 4.3).

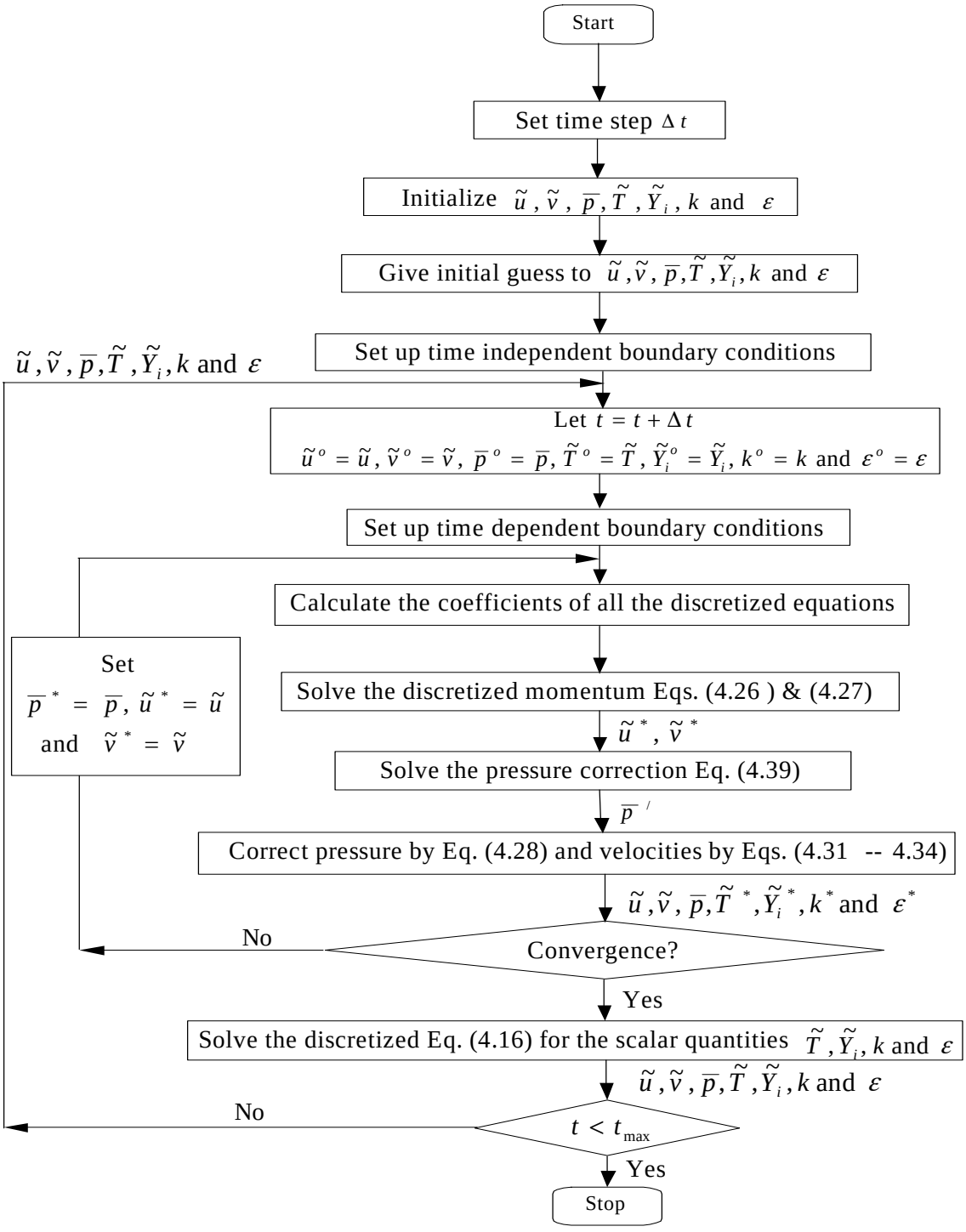

Figure 4.3: The SIMPLE algorithm.

4.5 Grid Details and Computation

4.5.1 Free Transient Turbulent jet

Along the radial direction fine uniform grid spacing is allocated at the inlet (inlet to control volume) while gradually increased spacing is considered away from it. Along the axial direction grid spacing is fine near the inlet and the wall but it is gradually increasing. The grid generated in this case is shown in Figure 4.4. The number of grid planes used in the radial direction is 40 while 50 grid planes are used in the axial direction, thus making a total of 2000 grid points. The grid independence test results for pressure and velocity in case of single species are shown in Figures 4.5 & 4.6 respectively whereas these results for pressure in case of multiple species are shown in Figures 4.7. It may be observed that for 55 $\times$ 45 grid points the results are almost in agreement with the results of 50 $\times$ 40 grid points, i.e., the maximum pressure and velocity magnitude differences are less than 0.1%.

Six variables in case of single species and nine variables in case of multiple species are computed at all grid points; these are: either the two velocity components, local pressure, two turbulence quantities and temperature or two velocity components, three species mass fractions, local pressure, temperature and two turbulence quantities.

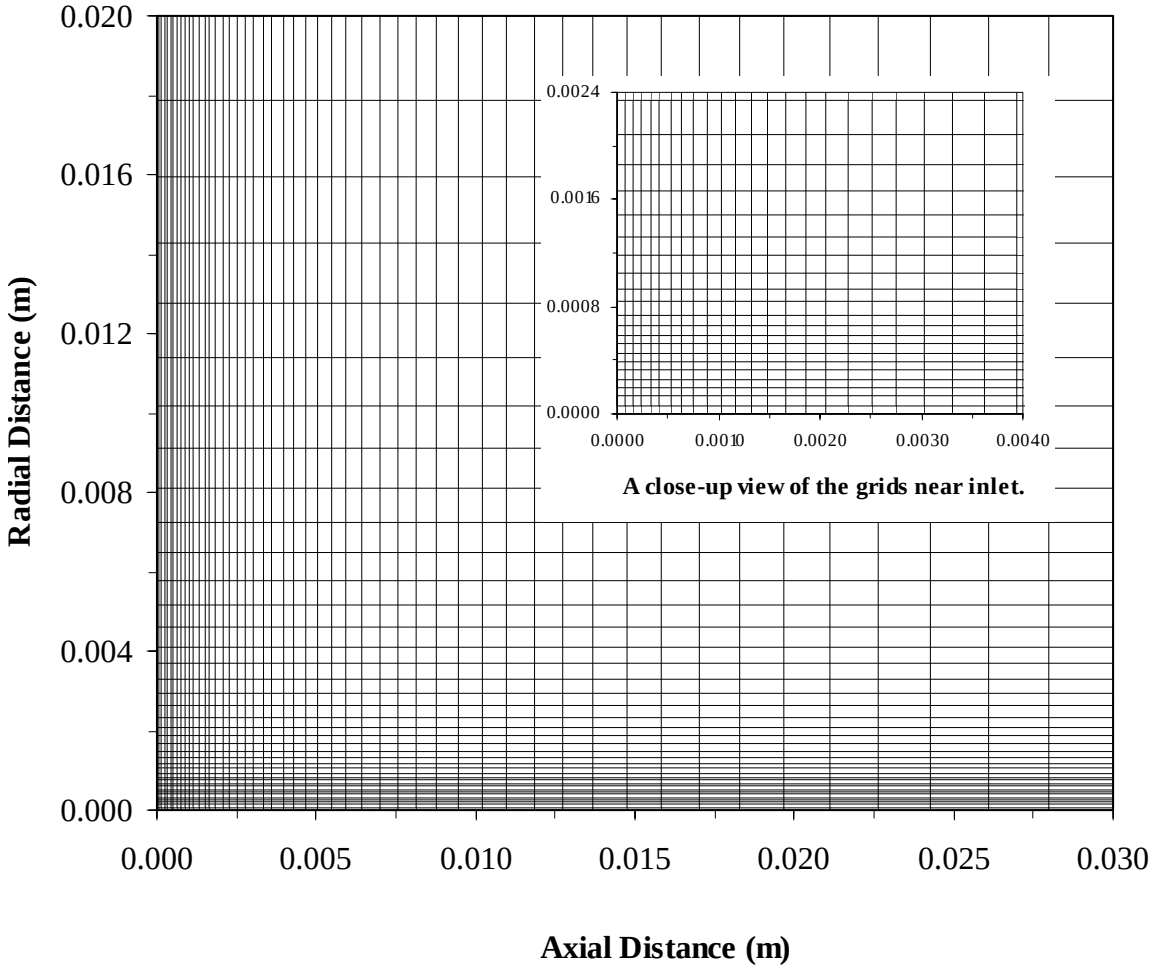

Figure 4.4: Computational domain for grid independent solution of an axisymmetric transient turbulent air/helium jet expanding into initially stagnant air (grid size: 50x40).

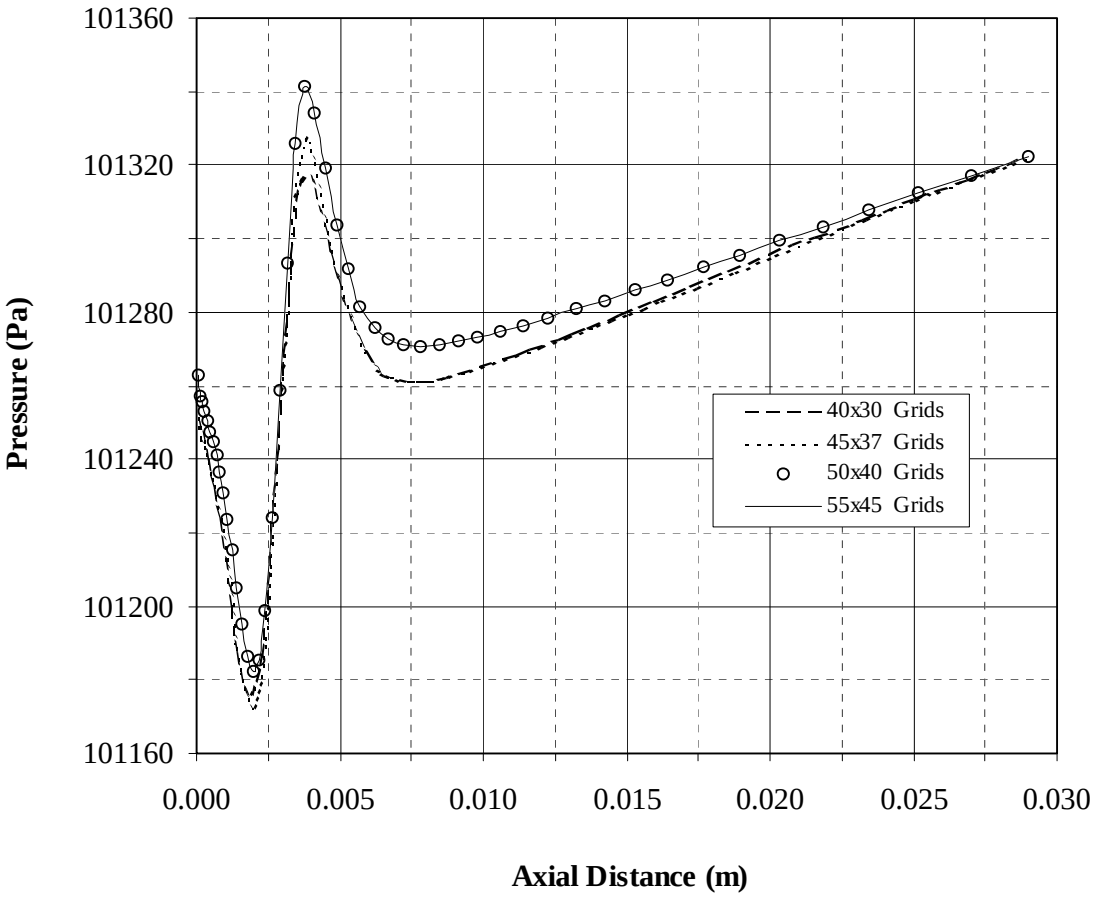

Figure 4.5: Grid independent test for pressure along the symmetry axis at r = 0 m and t =192.30 microseconds for air jet expanding into initially stagnant air.

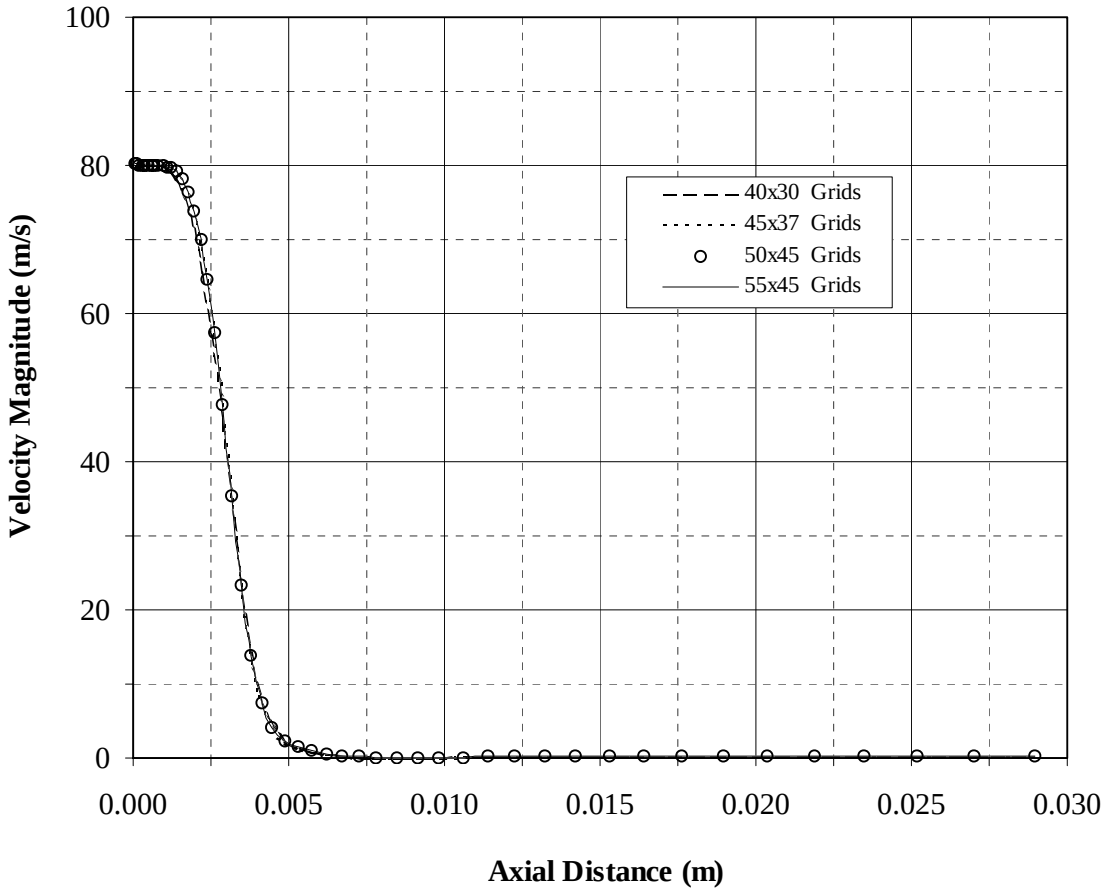

Figure 4.6: Grid independent test for velocity magnitude along the symmetry axis at r = 0 m and t = 192.30 microseconds for air jet expanding into initially stagnant air.

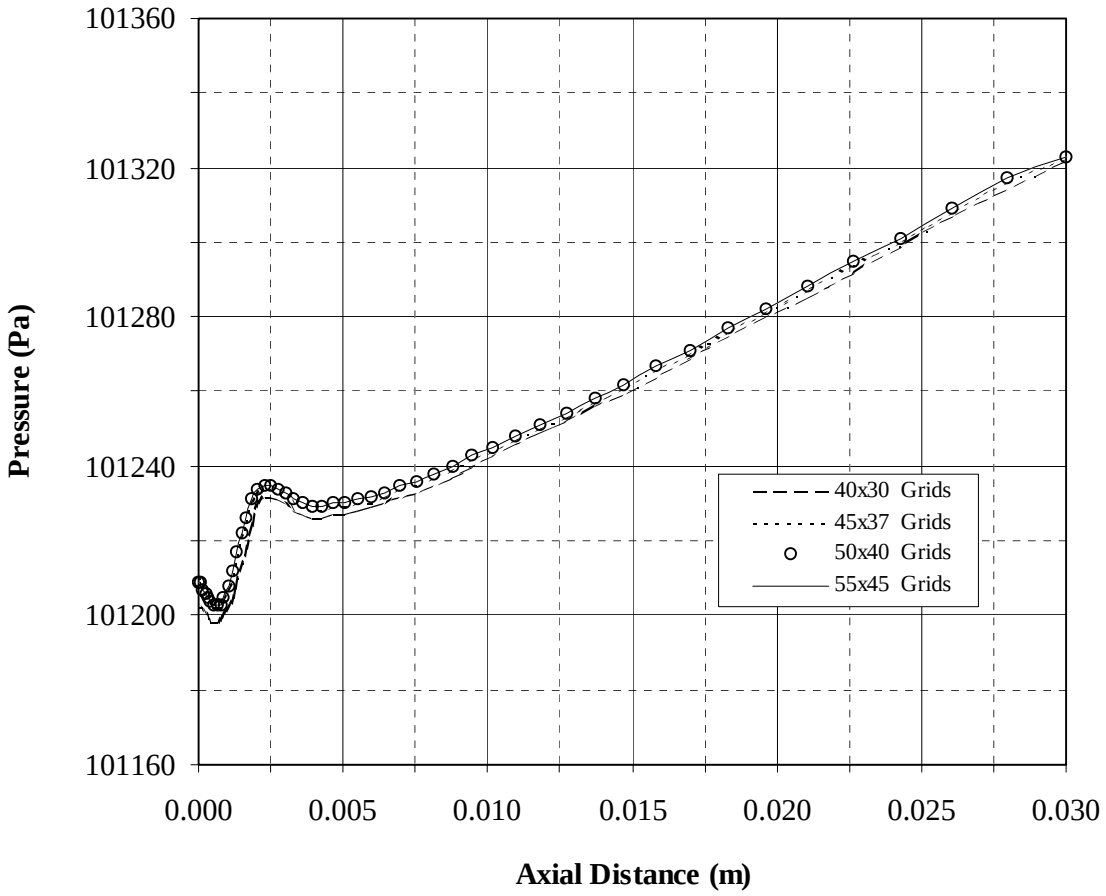

Figure 4.7: Grid independent test for pressure along the symmetry axis at r = 0 m and t = 192.30 microseconds for helium jet expanding into initially stagnant air.

4.5.2 Unsteady Opposing Jets

Along the radial direction fine uniform grid spacing is allocated at the inlets (inlets to control volume) while gradually increasing spacing is considered away from them so that still there is a fine grid distribution near the wall (*Wall 2*) next to the steady air jet inlet. Along the axial direction grid spacing is fine near inlets and the wall (*Wall 1*) next to the transiently developing jet inlet but it is gradually increasing. The grid generated in this case is shown in Figure 4.8. The number of grid planes used in the radial direction is 76 while 57 grid planes are used in the axial direction, thus making a total of 3996 grid points. The grid independence test results for pressure and axial velocity are shown in Figures 4.9 and 4.10 respectively. It may be observed that for 62×84 grid points the results are almost in agreement with the results of 57×76 grid points, i.e., the maximum pressure and axial velocity magnitude differences are less than 0.1%.

Nine variables are computed at all grid points; these are: two velocity components, three species mass fractions, local pressure, temperature and two turbulence quantities.

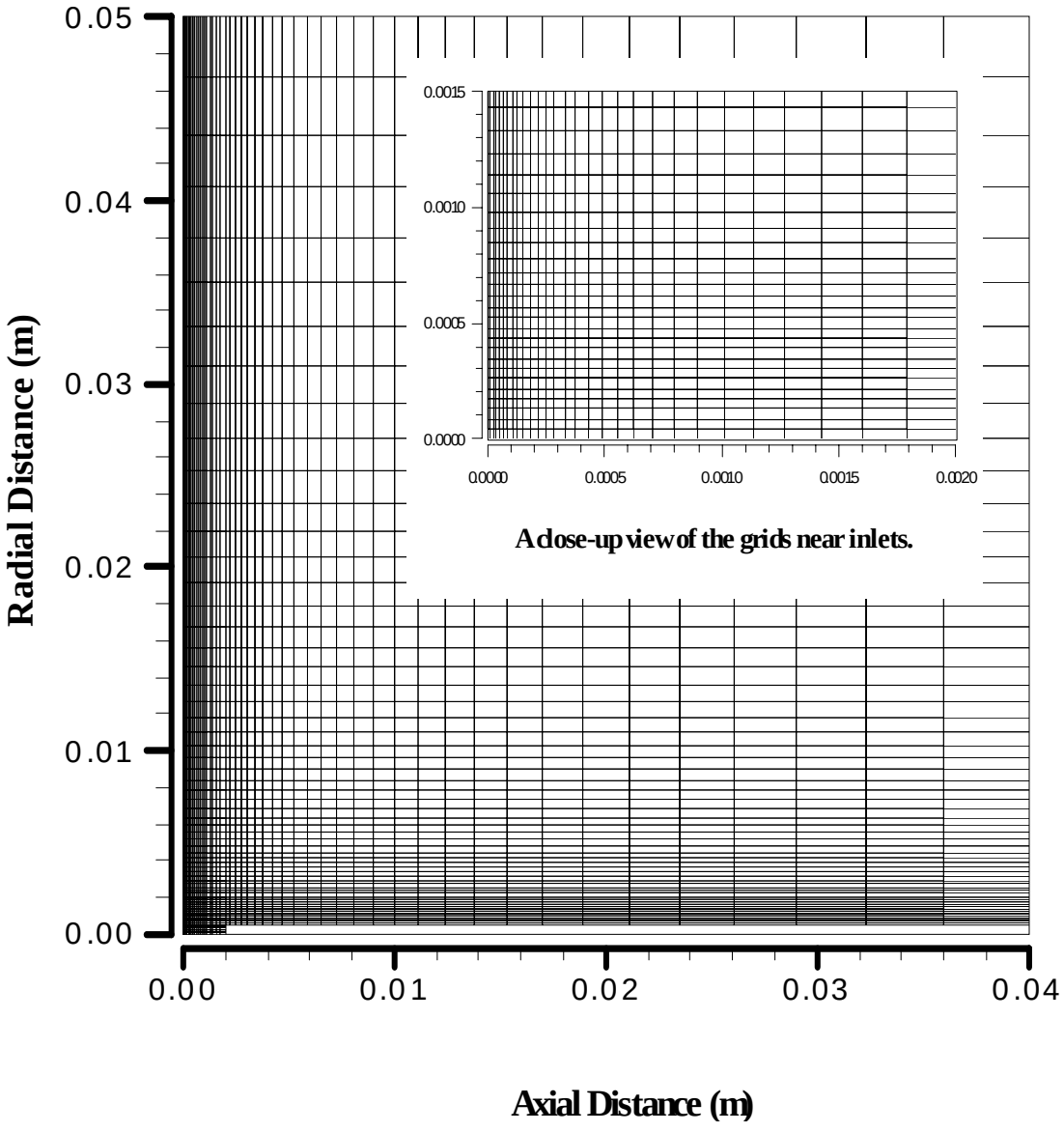

Figure 4.8: Computational domain for grid independent solution of a transiently developing turbulent helium jet opposing the steady turbulent air jet (grid size: 57x76).

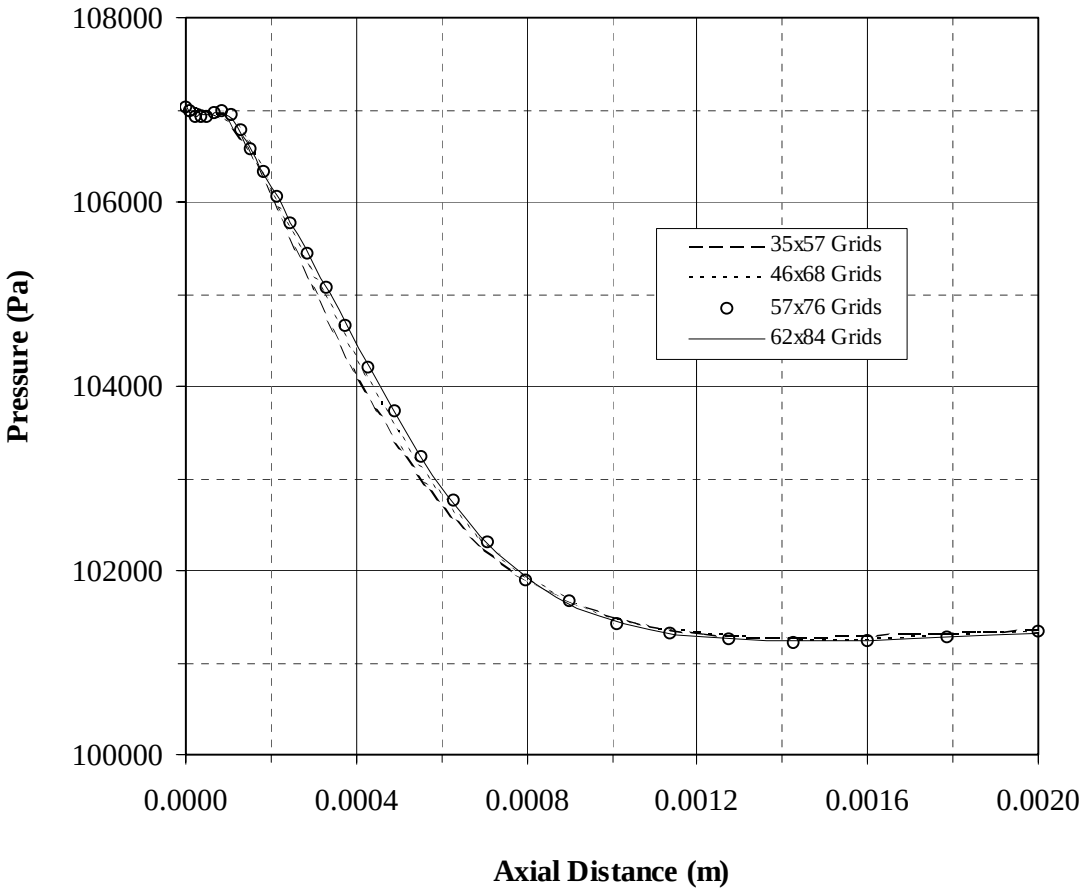

Figure 4.9: Grid independent test for pressure along the symmetry axis at r = 0 m and t = 192.30 microseconds for helium jet opposing the steady turbulent air jet.

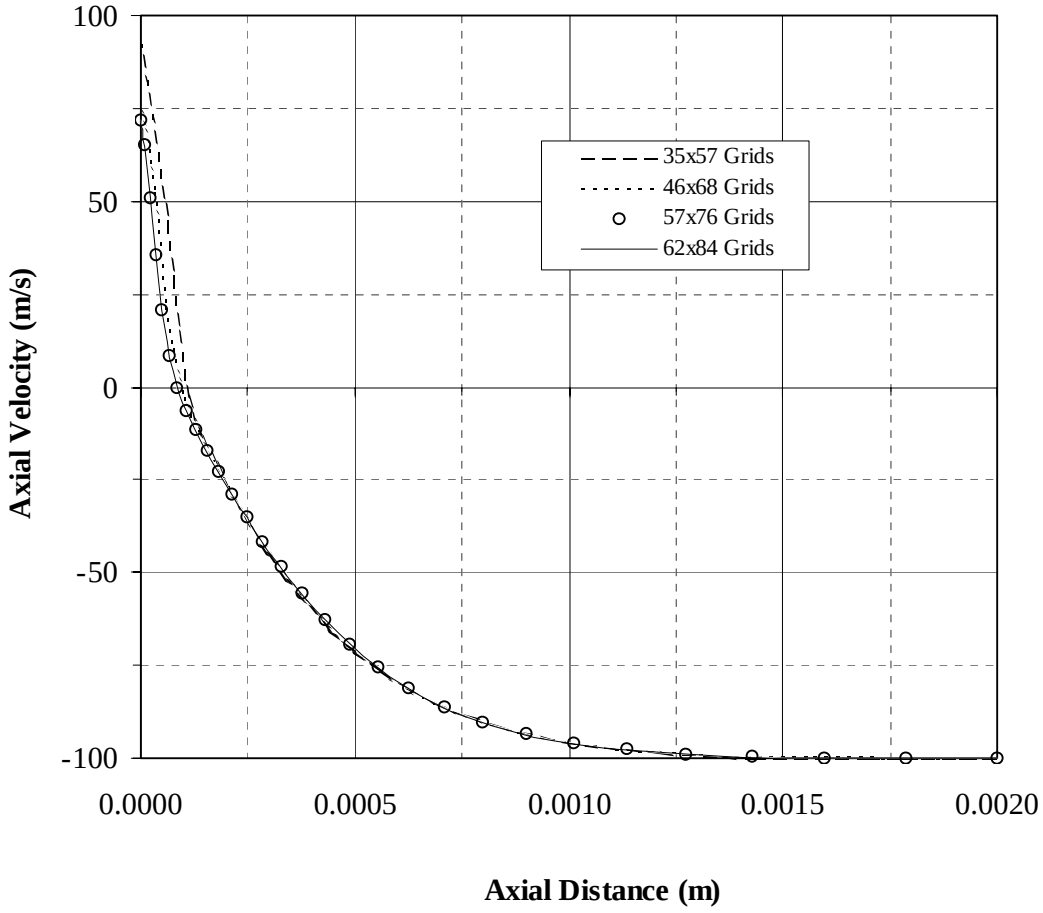

Figure 4.10: Grid independent test for axial velocity along the symmetry axis at r = 0 m and t = 192.30 microseconds for helium jet opposing the steady turbulent air jet.

Chapter 5

RESULTS AND DISCUSSIONS

5.1 Validation of the Model

Since the flow field presented in the present study resembles laser induced vapor expansion from the cavity, there are no experimental and theoretical studies to validate the present predictions. Therefore, in order to secure the validity of the present computational model, the simulation conditions are changed in accordance with the experiment of Kouros et al [41] to justify the capability of the model used in the present study to predict reasonably. However, the comparison of the prediction with the result of the above-mentioned experiment will be made after a brief look on the experimental set-up and the conditions involved in the experiment.

In Figure 5.1 a transparent tank having dimensions $1.2 \times 1.2 \times 1.5$ m deep is shown, in which the jet flow field is generated by a simple apparatus consisting of a 1.2 m long round clear acrylic tube held in place by a PVC plate at one end. At the other end, the tube is connected to a fluid feed line and a solenoid valve. The tube, which has a 28.6 mm inner diameter, is set vertically above the tank such that the tube exit is just below the water surface. Initially a rubber stopper is placed at the tube exit (inside the water tank) and dyed fluid is fed into the tube from a reservoir.

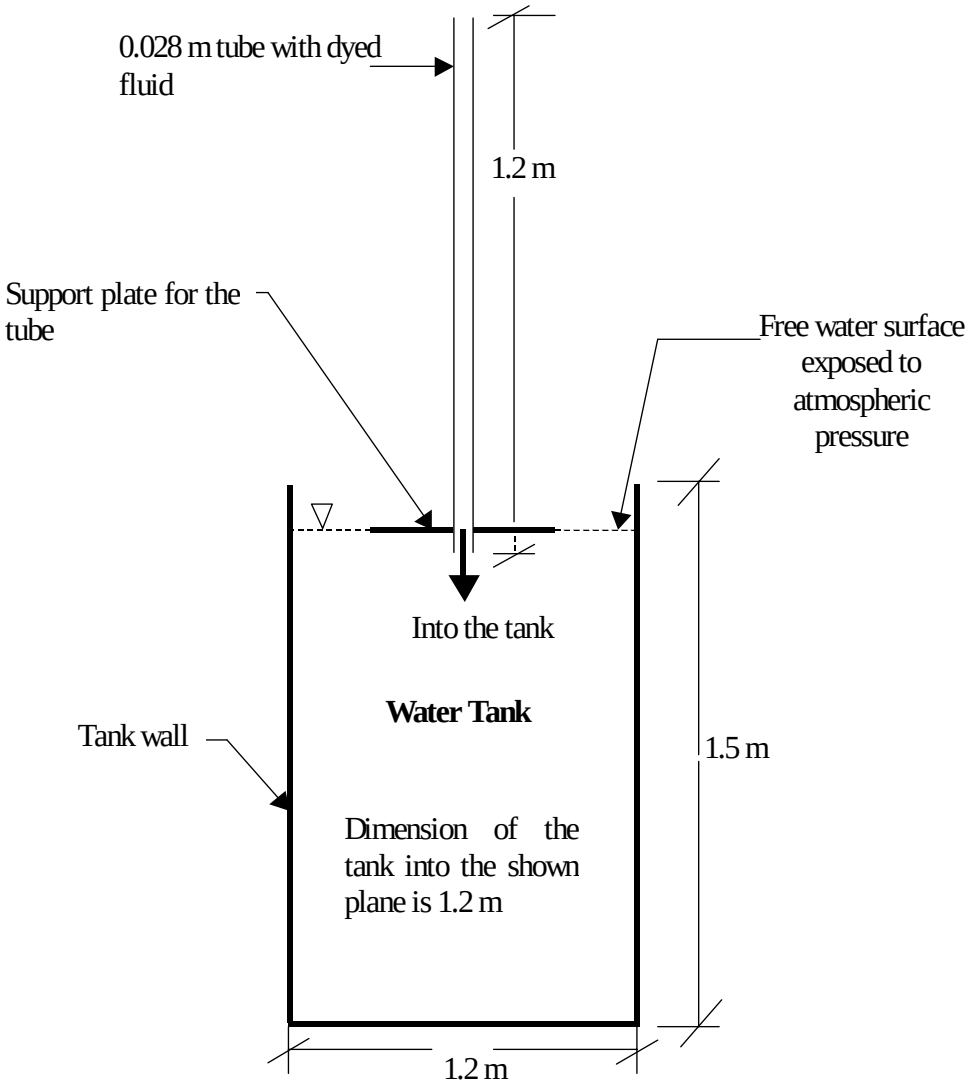

Figure 5.1: Sketch of the experimental set-up [41].

Once the tube is filled, the solenoid valve is closed and the fluid is allowed to become quiescent ($1 - 2min.$). The rubber stopper is then removed carefully. A minimal amount of dye ($\backsim 5cc$) diffused out of the tube prior to the start of the run. The fluid remains in place by means similar to those which keep a liquid inside a straw when one end is held airtight. Runs are started when the valve is rapidly opened. Gravity forces the dyed fluid into the water tank, thus dropping the dyed fluid height in the tube and as a result generating an unsteady velocity profile at tube exit. The variations in instantaneous fluid height and unsteady velocity with time obtained by Kouros et al [41] are shown in Figure 5.2. The maximum tube velocity was found as 1.86 m/s, resulting in a jet Reynolds number (based on the tube diameter) of 5.3×10^4. Hence based on this Reynolds number the jet flow field generated within the tank is considered turbulent (the instability of the free jets takes place at any Reynolds number [75]). Since the density difference between the jet dyed fluid and the tank water is less than 0.1% so the buoyancy effect can be neglected.

Capturing the images of the resulting flow field using the LIF photograph, the penetration of the tip of the jet was measured at various instants of time and is plotted against time, which is reproduced in Figure 5.3. In order to compare the variation of penetration length with time, the standard $k - \epsilon$ model is used. The comparison of results obtained numerically with the measured values is shown in Figure 5.4. It can be observed that both results are in good agreement. The error bars are associated with the experimental errors, which was reported as 3.5%.

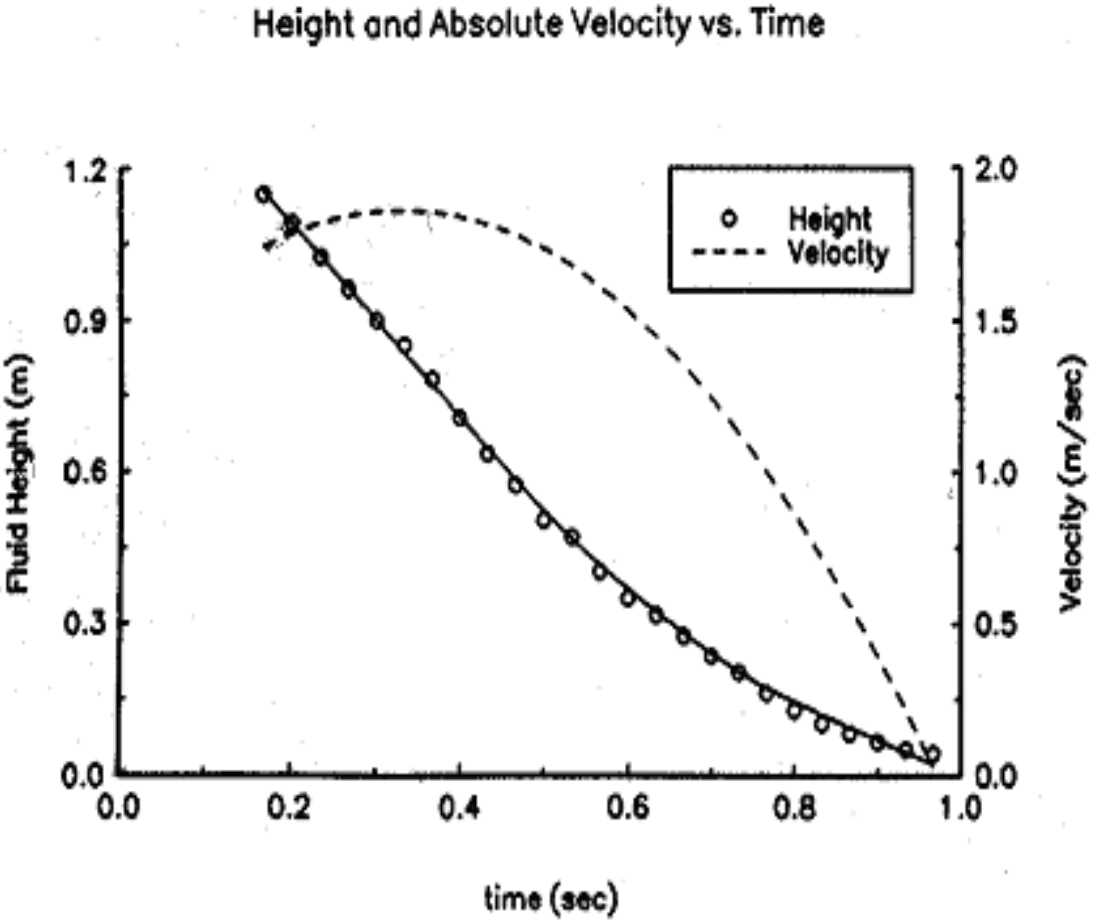

Figure 5.2: Measured fluid height and calculated velocity of the fluid inside the tube [41].

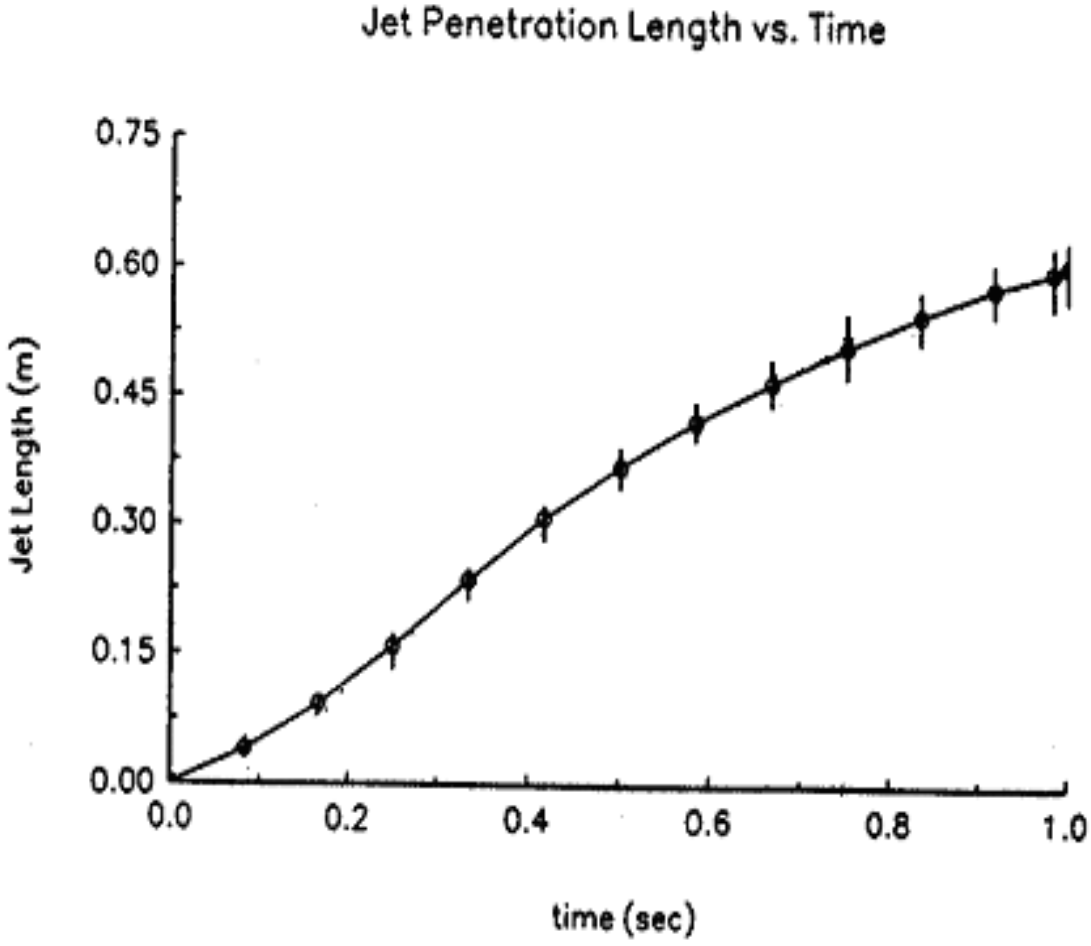

Figure 5.3: Ensembled averaged penetration length of the jet starting vortex vs time [41]. Maximum and minimum values are represented by the vertical bars.

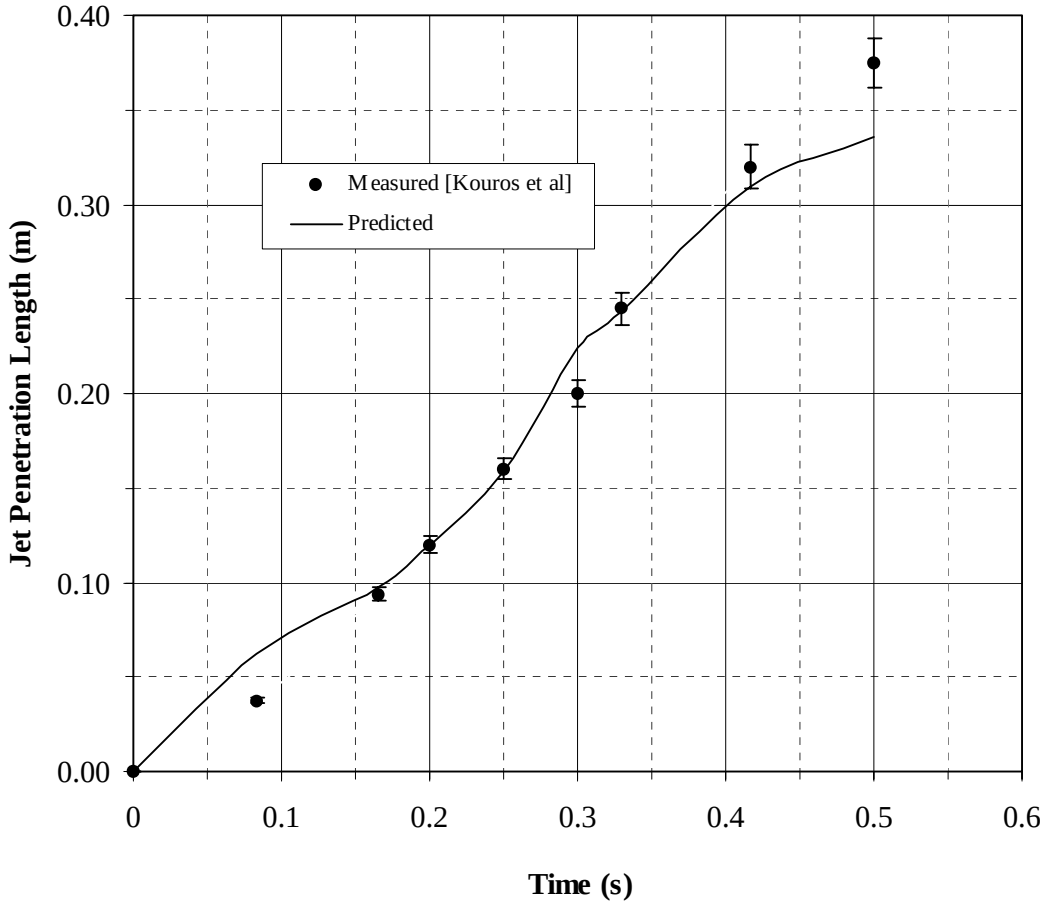

Figure 5.4: Comparison of numerical predictions with the experimental data for the case of unsteady turbulent jet entering the water tank [41]. The error bars are associated with the experimental error (3.5%) as indicated in the previous study [41].

5.2 Transient Jet Expansion into Stagnant Air

A transiently developing vapor jet emanating from the solid surface, which is exposed to laser irradiation, and expanding into an initially stagnant ambient, in practical applications the ambient is normally air, is simulated to resemble the laser induced evaporation process. Since the actual vapor properties are not known, the quantitative results become almost impossible. Therefore, in the first phase of the present study two gases; air and helium, at 1500 K (imitating the evaporating temperature of the laser-irradiated solid) are employed to resemble the laser-induced vapor jet expanding into an initially stagnant air ambient. This enforces the assumption that the two gas jets behave like perfect gases. Using the two different gases, i.e., helium and air, as perfect gases may not give the complete answer; however, it enables to demonstrate the quantitative behavior of the evaporating front (ejecting jet). Moreover, the evaporation of the solid surface causes the vapor jet which develops spatially and transiently, which implies that the velocity profile of the jet varies spatially and temporally. In the present study, this velocity profile of the vapor jet measured previously by Yilbas et al [78] is used as jet exit (inlet to the control volume) conditions to accommodate in the simulations. Figure 5.5 shows the jet exit (inlet to the control volume) profiles. Furthermore, since the flow field is actually generated by high velocity jet expanding into an initially stagnant air, therefore it is considered turbulent. In order to accommodate turbulence, the standard $k-\epsilon$ model is used.

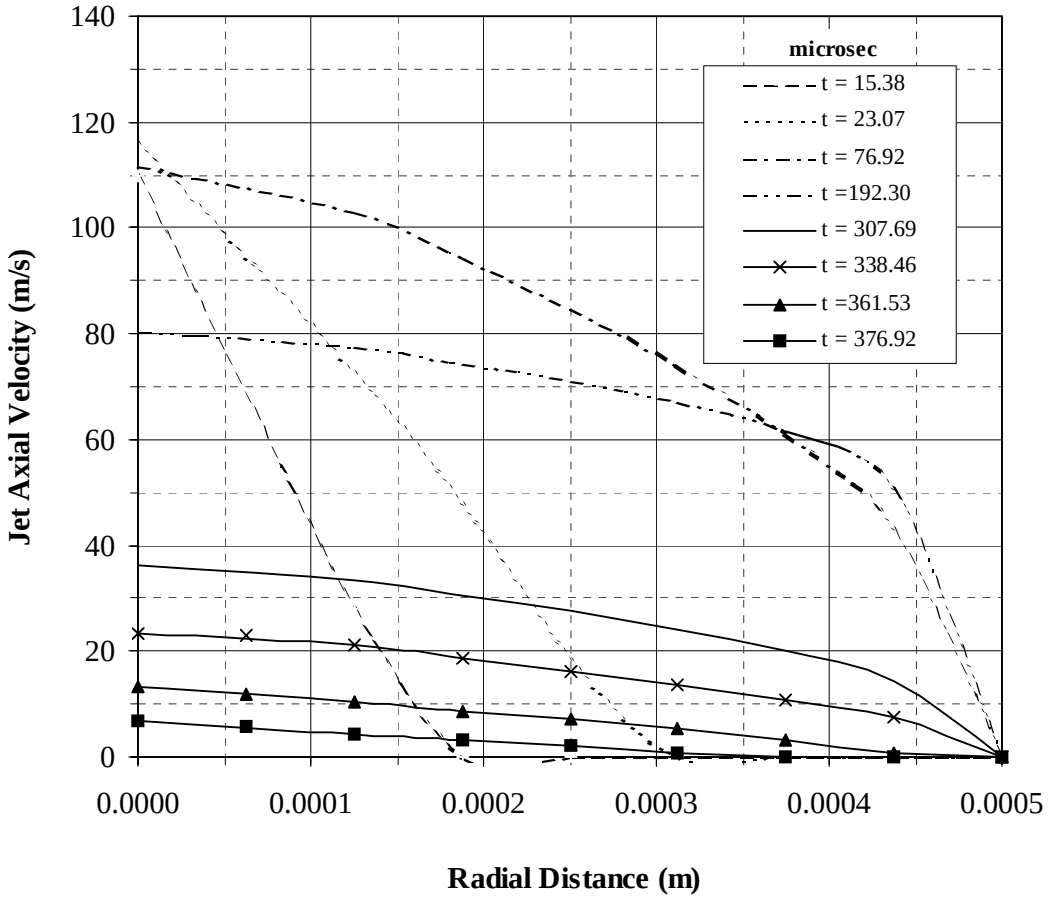

Figure 5.5: Profiles of jet axial velocity at the transiently developing jet inlet for various times [78].

5.2.1 Transient Air Jet into Stagnant Air

Figure 5.6 and 5.7 show velocity vectors in the region close to the jet inlet-expansion region as well as in the radially extended and axially contracted region at different times. The jet expansion results in the development of the circulation cell in the region next to the jet outer surface. This is because of the flow entrainment in this region. The orientation of the circulation cell changes as jet expansion progresses. This is mainly because of the jet inlet velocity profile, which changes spatially with time (Fig. 5.5). Therefore, the fluid entrainment varies with time. In the early period ($t \leq 76.92\ \mu s$), jet expands radially more than it does axially; however, as the time progresses axial expansion dominates over the radial expansion. This is due to: *i*) the pressure which builds up close to the jet front region, and *ii*) the jet inlet velocity profile which develops radially with time (Fig. 5.5). In this case, as the jet velocity profiles become almost similar, the axial expansion of the jet is considerable.

Figure 5.8 shows the velocity magnitude contours while Figure 5.9 shows its variation along the symmetry axis as time variable. In the early period, jet expansion is not considerable and as the time progresses jet expands radially first and then expands further along the axial direction. This is because of the jet exit velocity profile, which develops radially with time, as well as still air resistance opposing the jet expansion in the axial direction. Flow entrainment is evident after $t = 23.07\ \mu s$, in this case, the outer velocity contours differ than those corresponding to earlier time period. Although the jet penetration extends in the axial direction, velocity

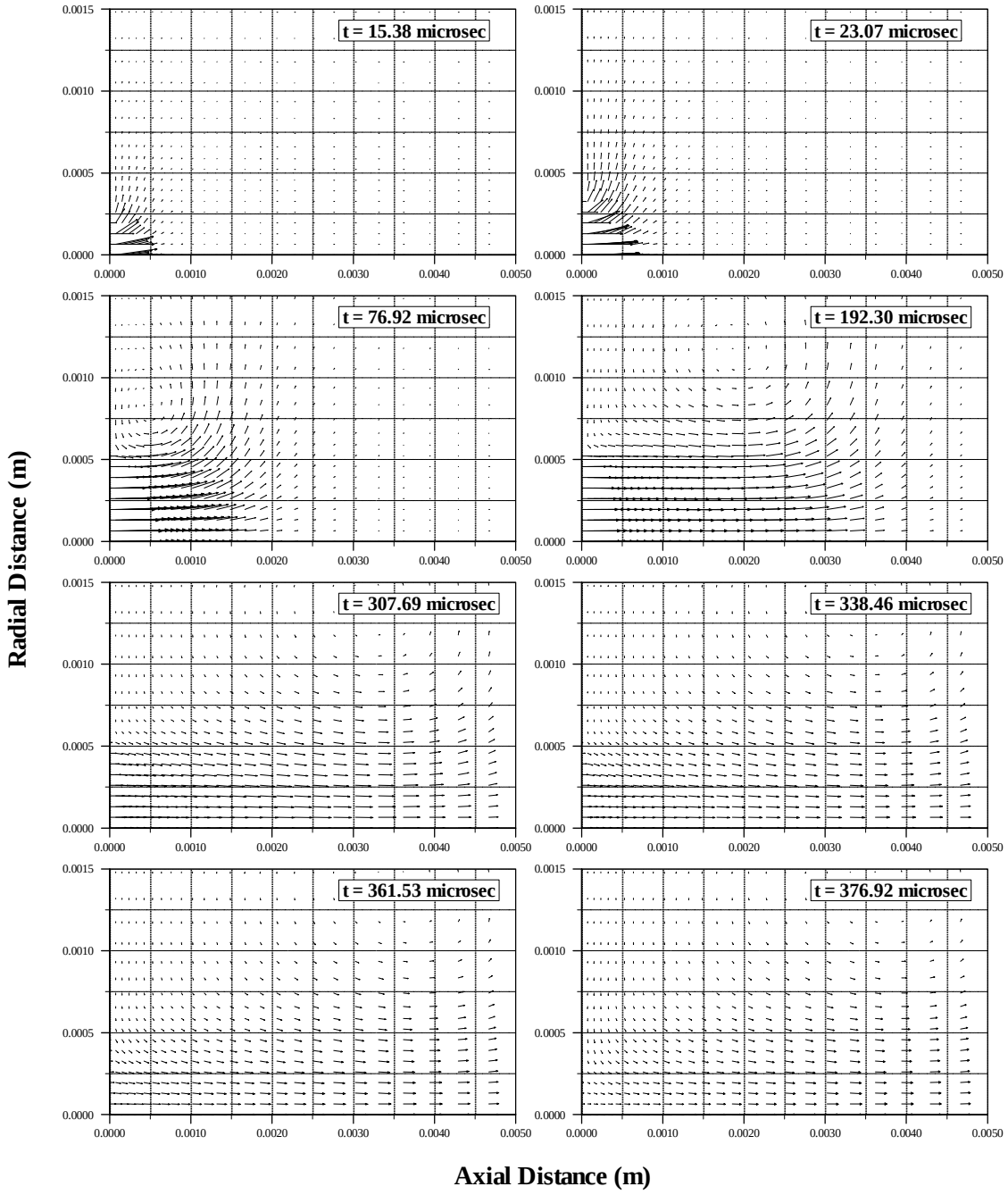

Figure 5.6: Time development of velocity vector plots for an axisymmetric transient turbulent air jet close to the jet inlet-expansion region.

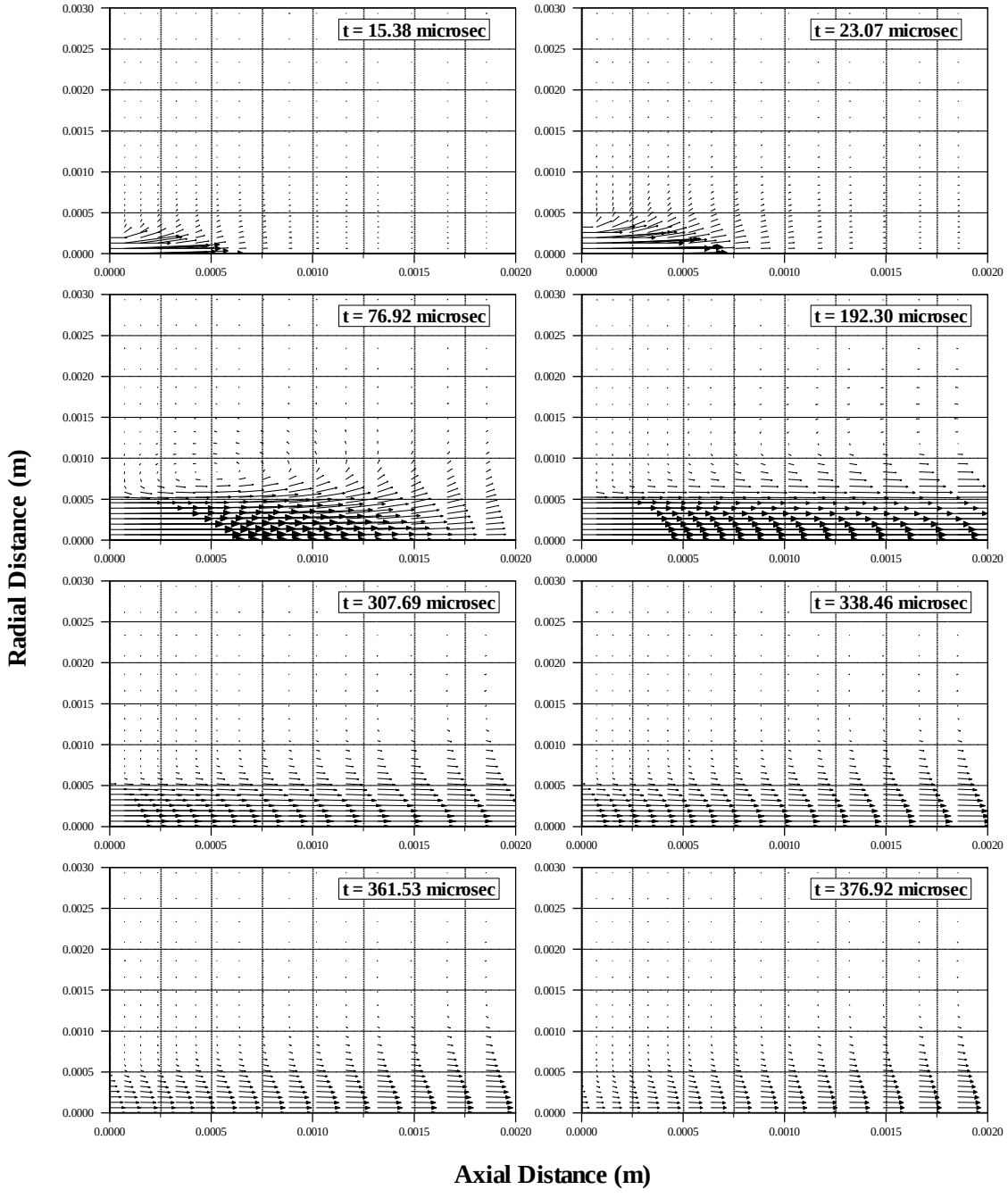

Figure 5.7: Time development of velocity vector plots for an axisymmetric transient turbulent air jet in the radially extended and axially contracted region.

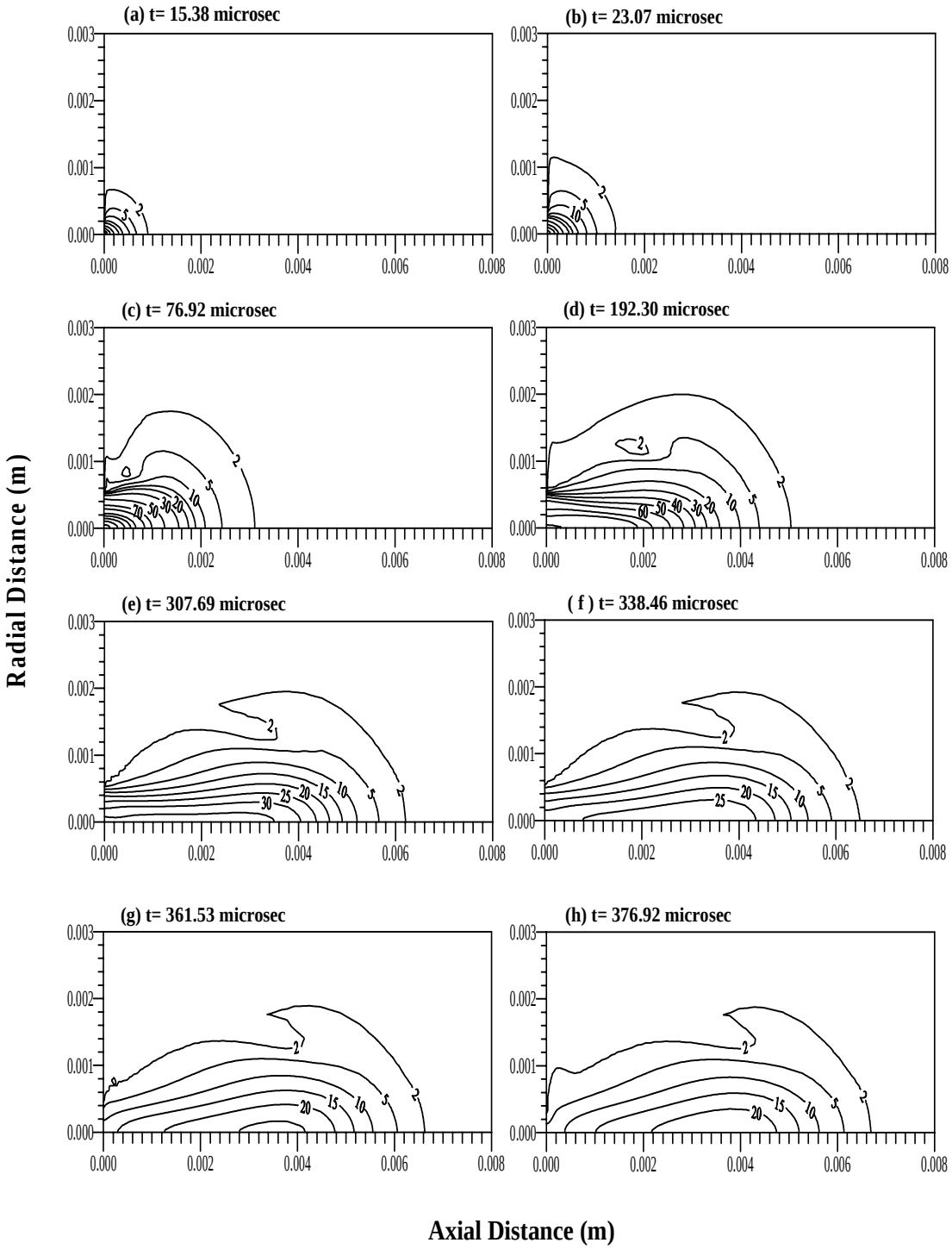

Figure 5.8: Time development of velocity magnitude (m/s) contours for an axisymmetric transient turbulent air jet expanding into initially stagnant air.

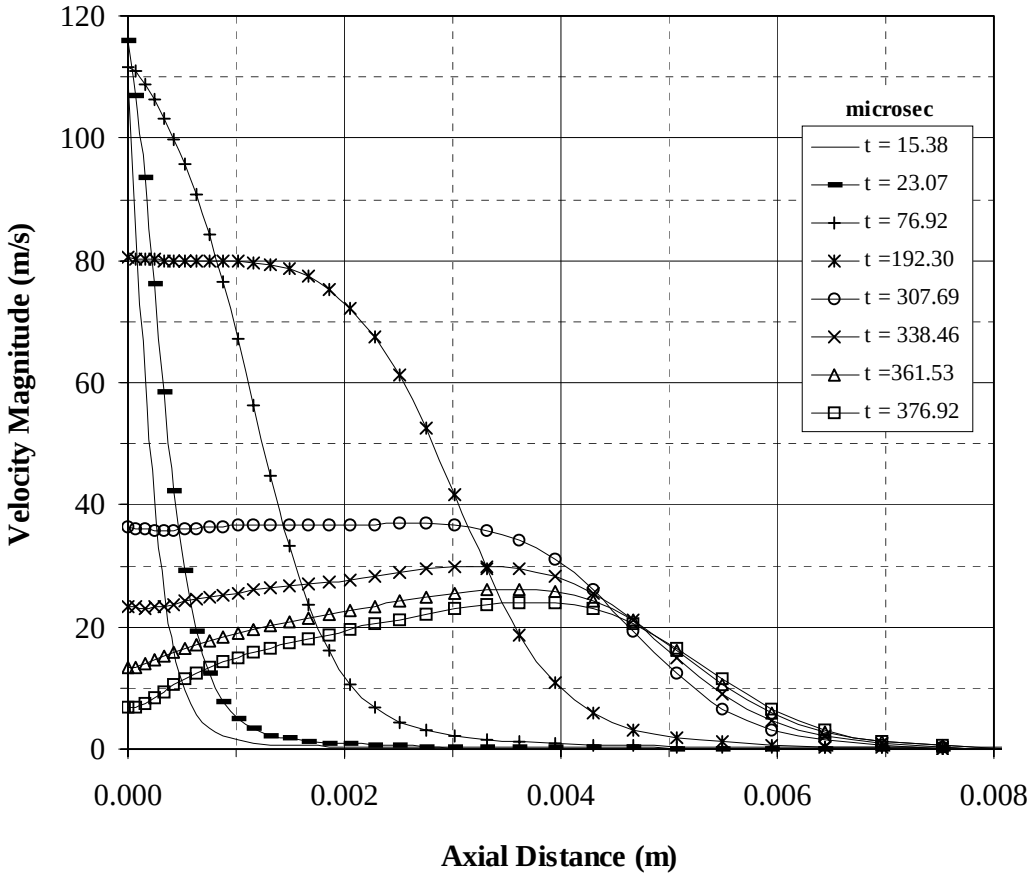

Figure 5.9: Temporal variation of velocity magnitude along the jet symmetry axis at r = 0 m for air jet expanding into initially stagnant air.

magnitude reduces considerably with progressing time (Fig. 5.9). This occurs because of the jet exit velocity profile, where the mean velocity reduces significantly (Fig. 5.5). The turbulence kinetic energy is high at the jet exit in the early period. This can be observed from Figure 5.10, in which turbulence kinetic energy along the symmetry axis is shown. This is because of the jet exit velocity profile. It should be noted that the turbulence kinetic energy is associated with the jet exit velocity profile (Eq. (3.34)). The turbulence kinetic energy reduces at jet exit; however, it attains relatively high values along the symmetry axis during $76.92 \leq t \leq 192.30 \mu s$. As the time progresses, its magnitude reduces and does not alter much along the symmetry axis. This indicates that initial jet expansion results in high degree of turbulence and once the jet penetration is progressed, the degree of turbulence reduces significantly. Moreover, changes in jet exit velocity profile results in changes in velocity magnitude along the symmetry axis. This, in turn, causes large variation in turbulence kinetic energy, which was also observed in the previous study [82].

Figure 5.11 shows the pressure contours in the region close to the jet expansion and Figure 5.12 shows the pressure distribution along the symmetry axis. The flow entrainment and formation of circulation cell is evident from the pressure contours, which is more visible after $t = 76.92\ \mu s$. In the early period, jet radial expansion is more than its axial expansion due to the pressure which builds up close to the jet inlet region and as time reaches $t = 192.30\ \mu s$ axial expansion of the jet becomes significant, in which case, the pressure in the jet front region becomes higher than the jet inlet. This implies the shifting of the pressure peak along the symmetry axis

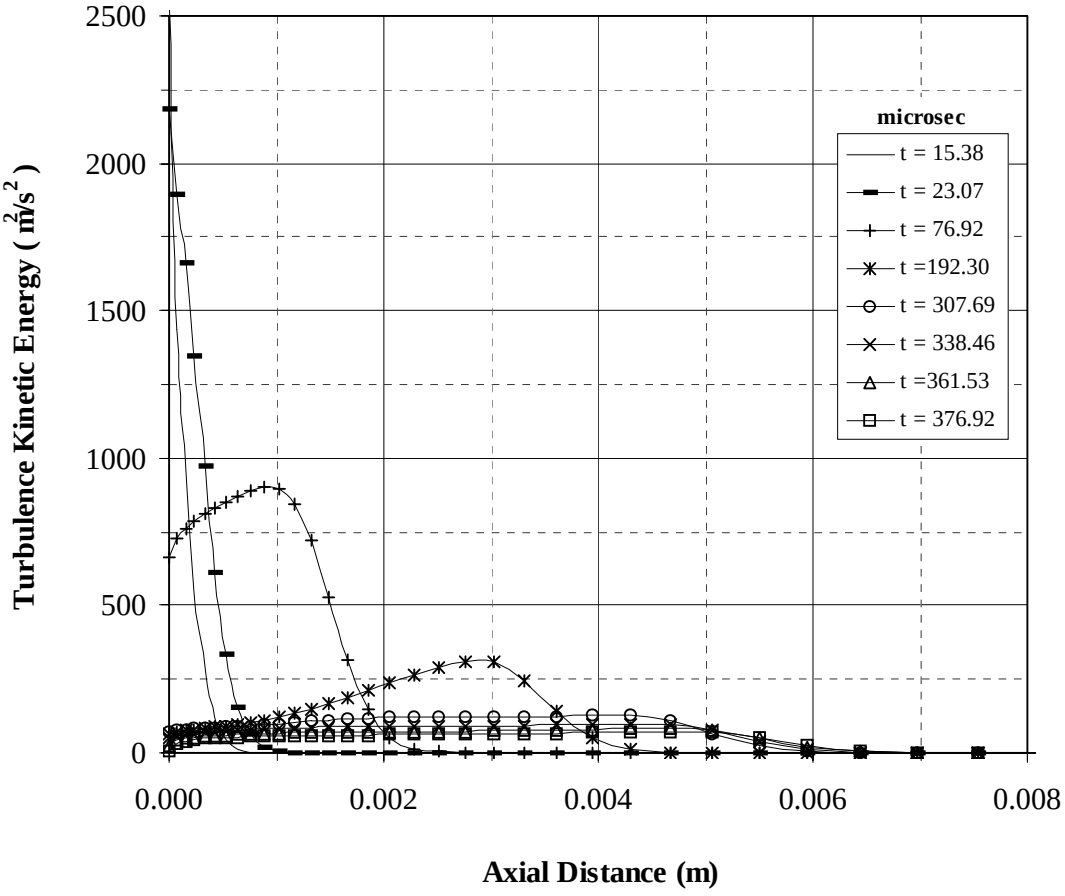

Figure 5.10: Temporal variation of turbulence kinetic energy along the jet symmetry axis at r = 0 m for air jet expanding into initially stagnant air.

with progressing time (Fig. 5.12). As the jet inlet profile becomes almost similar, the pressure magnitude along the symmetry axis does not vary considerably, which in turn results nearly similar pressure profiles along the symmetry axis.

Figure 5.13 shows temperature profiles along the symmetry axis as time variable while Figure 5.14 shows temperature contours at different times. Temperature profiles follow almost the profiles of velocity magnitude. This is more pronounced in the early periods. In this case, convective heat transfer from the jet surface to its ambient is small due to short period of time and small area of jet surface. As the time progresses, temperature profiles extend into the jet ambient as follows the jet expansion. When the jet exit profiles become almost similar in magnitude and shape, the extension of the temperature profiles into the ambient becomes similar to the case observed for the unsteady jets [29].

Figure 5.15 shows the dimensionless ratio(ratio of the jet width to penetration depth) while the logo in the figure shows temporal behavior of penetration depth. The penetration depth in the early period is low as compared to jet width in the radial direction. Moreover, as the time progresses, penetration depth becomes larger and the radial expansion of the jet becomes less than the penetration along the jet symmetry axis. However, as the time progresses further, jet expansion results in almost self-similar region as noted in the previous study [29]. In this case D/Z_t attains almost steady decay, which is more pronounced after 250 μs. Moreover, it was shown that for a fixed jet exit velocity profile a self-similar transient jet could be resulted [29]. Since the gas inlet velocity profiles are varied in the present simulations (in order to

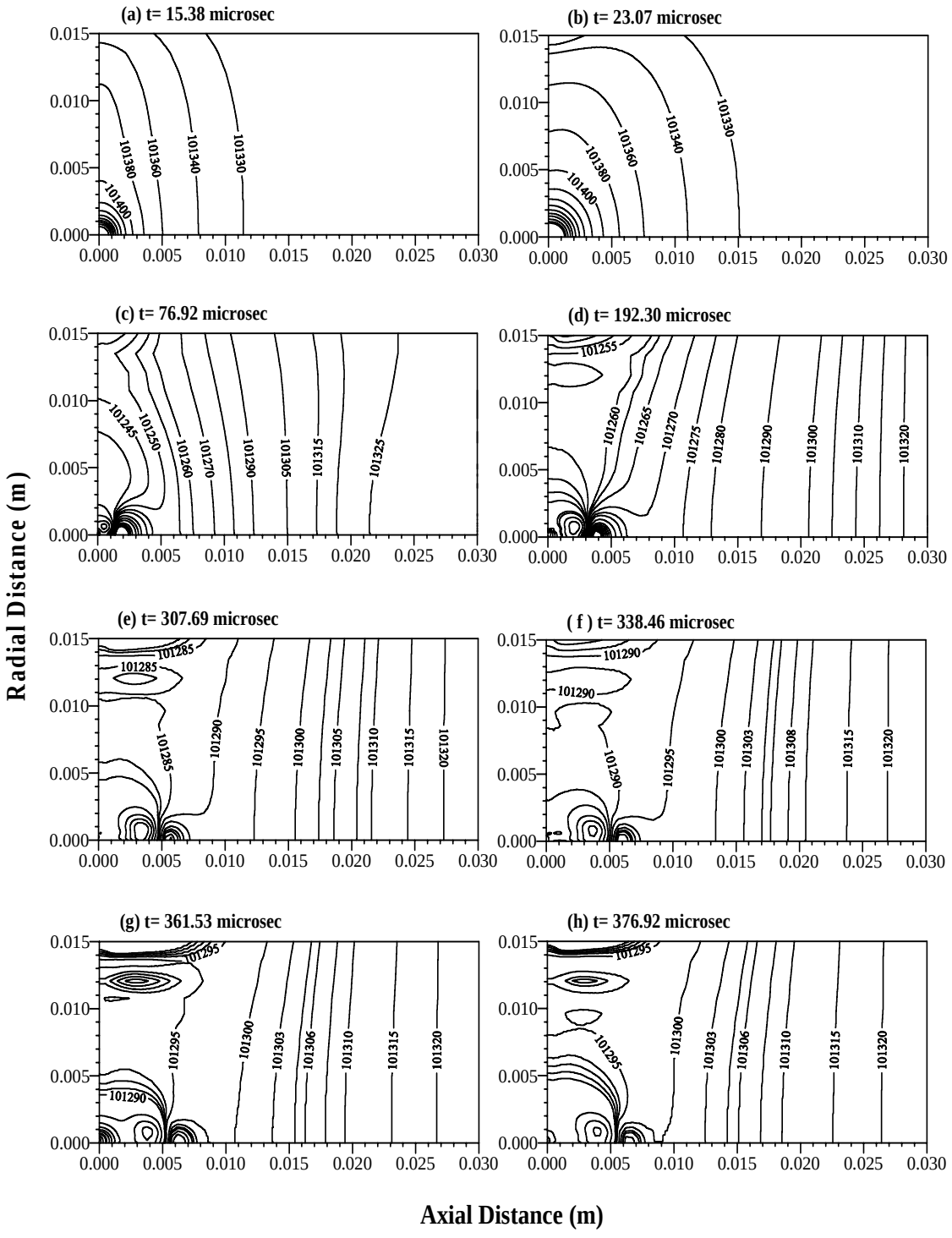

Figure 5.11: Time development of pressure (Pa) contours for an axisymmetric transient turbulent air jet expanding into initially stagnant air.

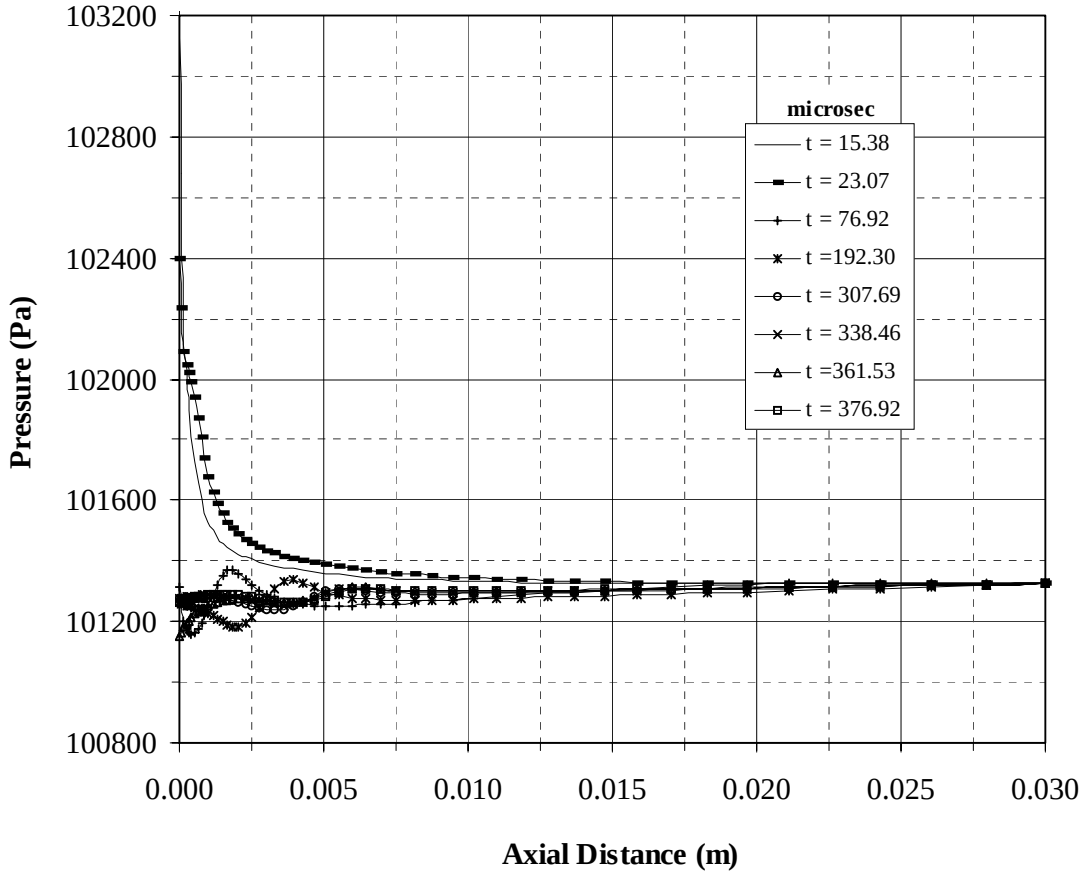

Figure 5.12: Temporal variation of pressure along the jet symmetry axis at r = 0 m for air jet expanding into initially stagnant air.

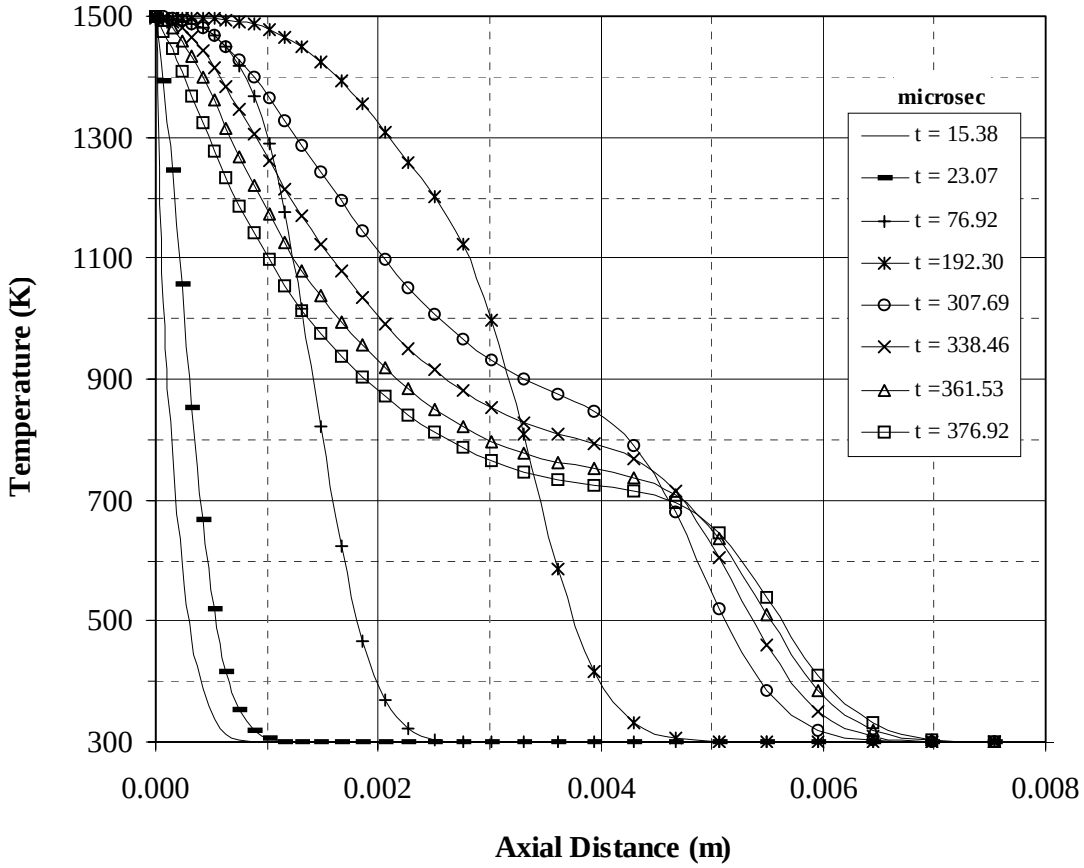

Figure 5.13: Temporal variation of temperature along the jet symmetry axis at r = 0 m for air jet expanding into initially stagnant air.

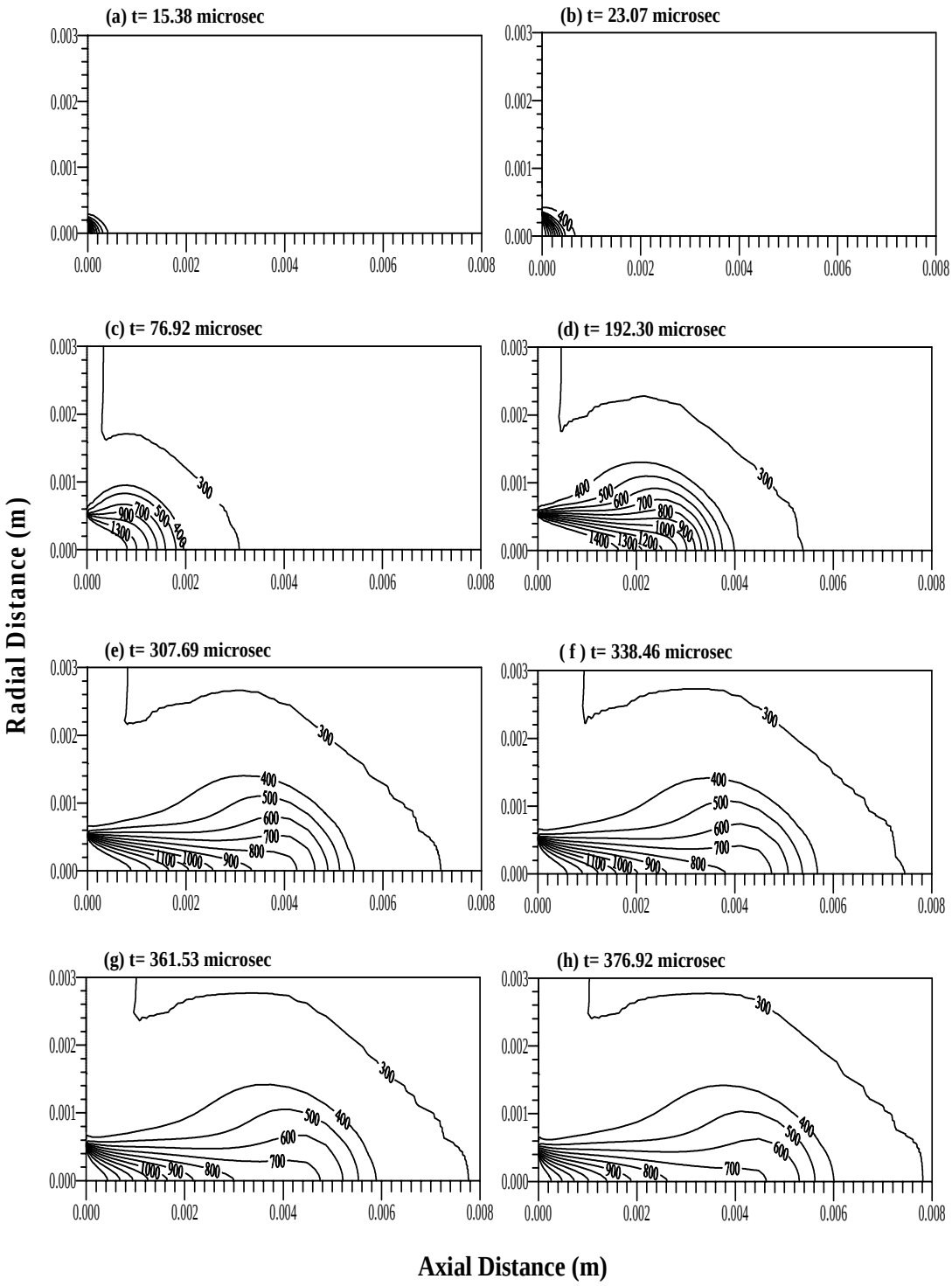

Figure 5.14: Time development of temperature (K) contours for an axisymmetric transient turbulent air jet expanding into initially stagnant air.

resemble vapor ejection from the laser-produced cavity), a self- similar region is not observed clearly in the initial period, except when the jet exit profiles become almost similar. This corresponds to time period of 350 μs.

Figure 5.16 shows the ratio of penetration depth (Z_t) to $\frac{1}{4}$ power of momentum rate per unit density $\left(\dot{M}_{Air}\ /\overline{\rho}\right)$. It should be noted that the penetration number is given as [29]:

$$\frac{Z_t}{\left(\dot{M}_{Air}\ /\overline{\rho}\right)^{1/4} \times \sqrt{t}} = f(D/Z_t) \tag{5.1}$$

It was reported that for slow flow transient jets, the penetration number remains constant [29]. It can be observed from Figure 5.16 that the penetration number increases linearly with $\sqrt{t}$ for $\sqrt{t} \leq 12\sqrt{\mu s}$ and beyond this time it changes vastly, i.e. constant slope of the curve indicates the constant rate of increase in penetration number. Consequently, in the early period jet behavior is similar to that corresponding to slow flow jet expansion. In this case, the penetration depth is low and the momentum of the jet is high. As the time progresses, some portion of the jet momentum is lost due to viscous effect. This in turn reduces the specific momentum of the jet. Moreover, as the time progresses, the jet penetration rate reduces due to large diffusion in the region next to the jet front. Although the jet penetration rate reduces with progressing time, the jet momentum reduces more swiftly because of the viscous dissipation. Therefore, the rate of momentum loss is considerably higher than the reduction in penetration rate. This, in turn, results in rapid rise of slope of

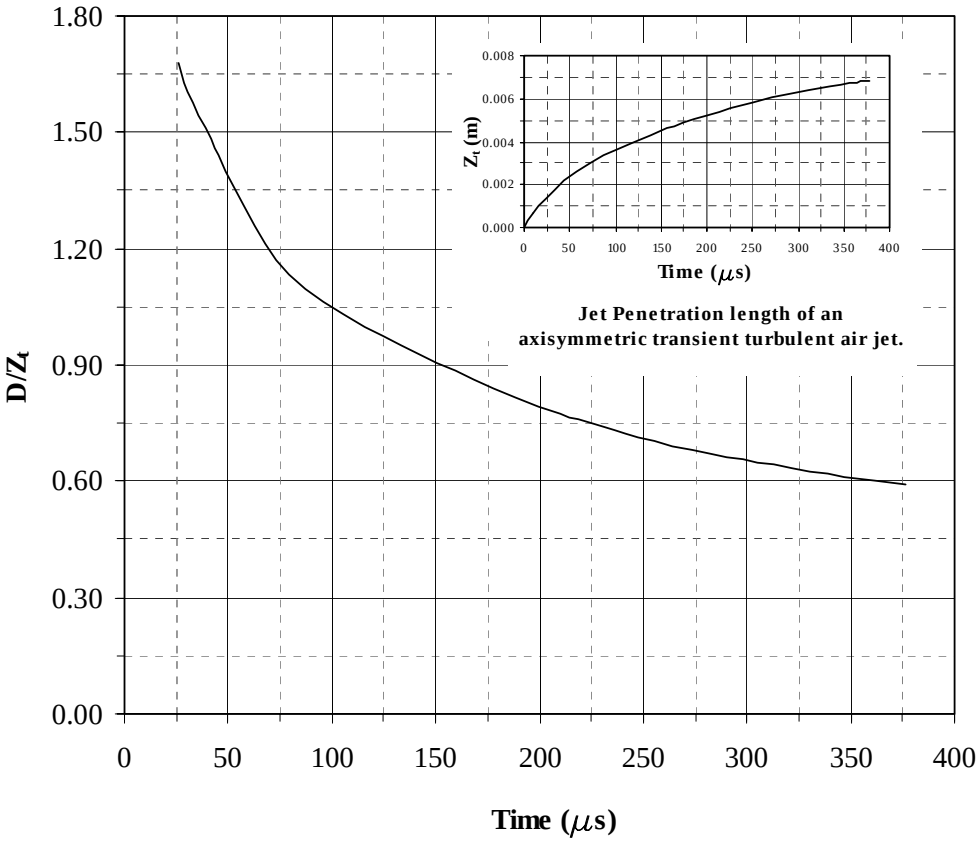

Figure 5.15: Ratio of jet width to penetration length with time for an axisymmetric transient turbulent air jet expanding into initially stagnant air.

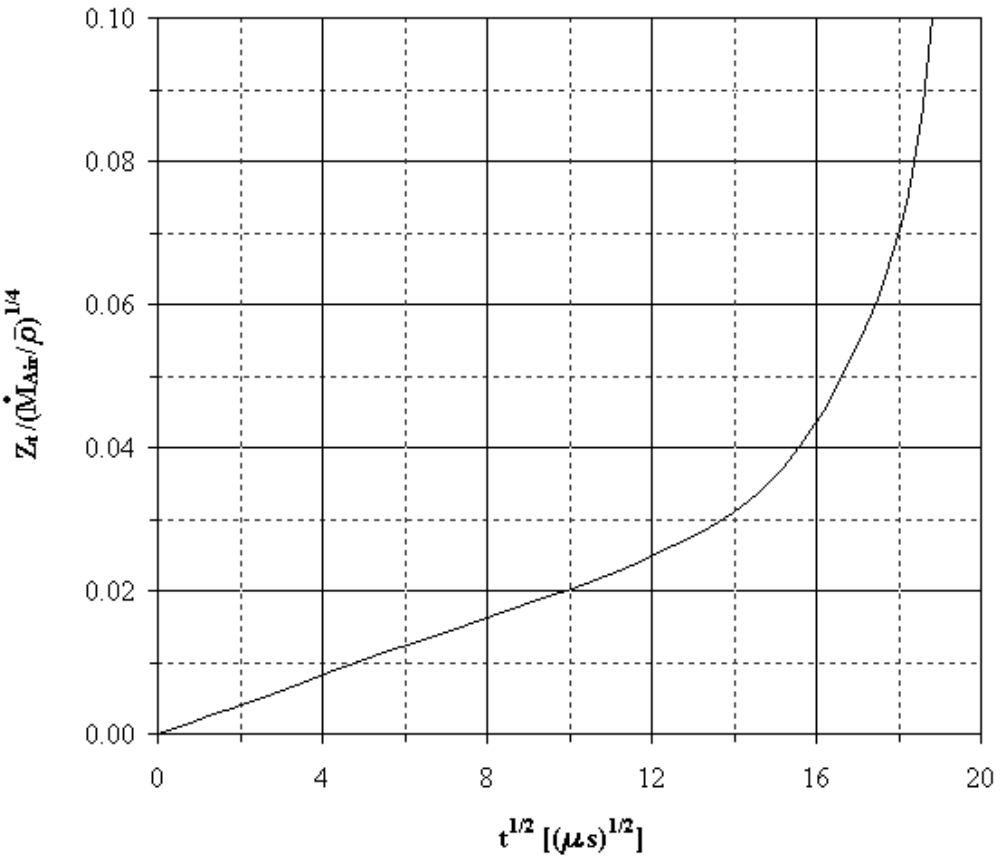

Figure 5.16: Penetration rate of an axisymmetric transient turbulent air jet exiting into initially stagnant air.

the curve in the figure for $\sqrt{t} \geq 12\sqrt{\mu s}$.

5.2.2 Transient Helium Jet into Stagnant Air

Figures 5.17 & 5.18 show the velocity vector in the close region of the jet expansion as well as in the radially extended and axially contracted region at different times. In the early times, jet expands first radially and then along the axial direction; this is because of the jet exit velocity profile, which develops radially with time, as well as stagnant air resistance opposing the jet expansion in the axial direction. Since the jet inlet velocity profile changes with time, there is no specific pattern of expansion is observed from the vector plot until after time reaches $t = 76.92\ \mu s$. As the time progresses, jet inlet velocity decays so that the jet expansion into its ambient dies. Moreover, the flow entrainment results in a circulation cell next to the jet boundary, which is more pronounced after $t = 192.30\ \mu s$. As the time progresses the orientation of the circular cell changes and the cell moves away from the jet boundary. As the time progresses further, the magnitude of jet inlet velocity reduces, the size of the circulation cell increases. In this case, jet boundary mixes with the secondary flow generated by the circulation cell.

Figure 5.19 shows the velocity magnitude contours while Figure 5.20 shows its variation along the symmetry axis as time variable. In the early period, jet expansion is not considerable and as the time progresses jet expands radially first and then expands further along the axial direction. This is because of the jet exit velocity profile, which develops radially with time as well as still air resistance opposing the

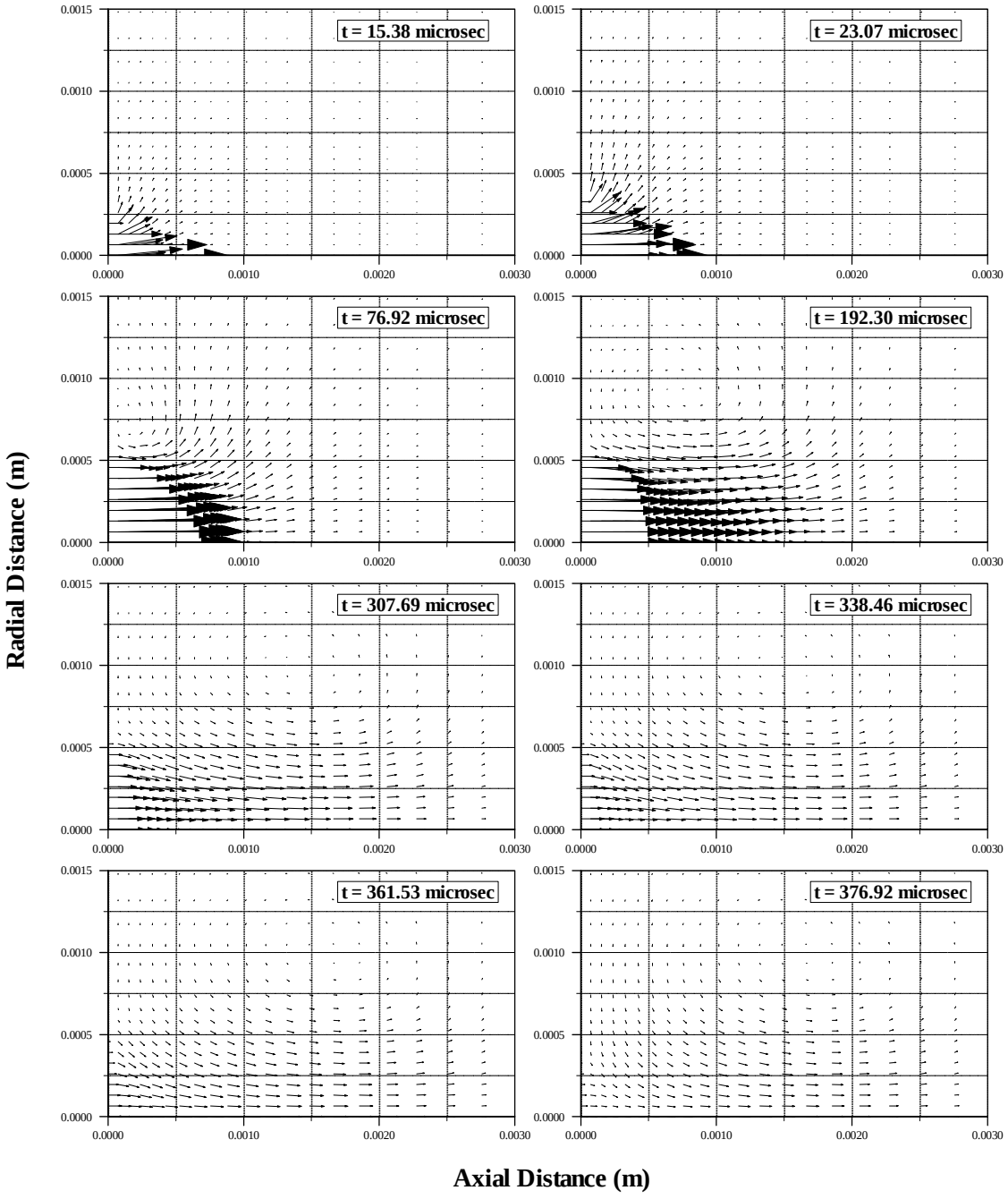

Figure 5.17: Time development of velocity vector plots for an axisymmetric transient turbulent helium jet close to the jet inlet-expansion region.

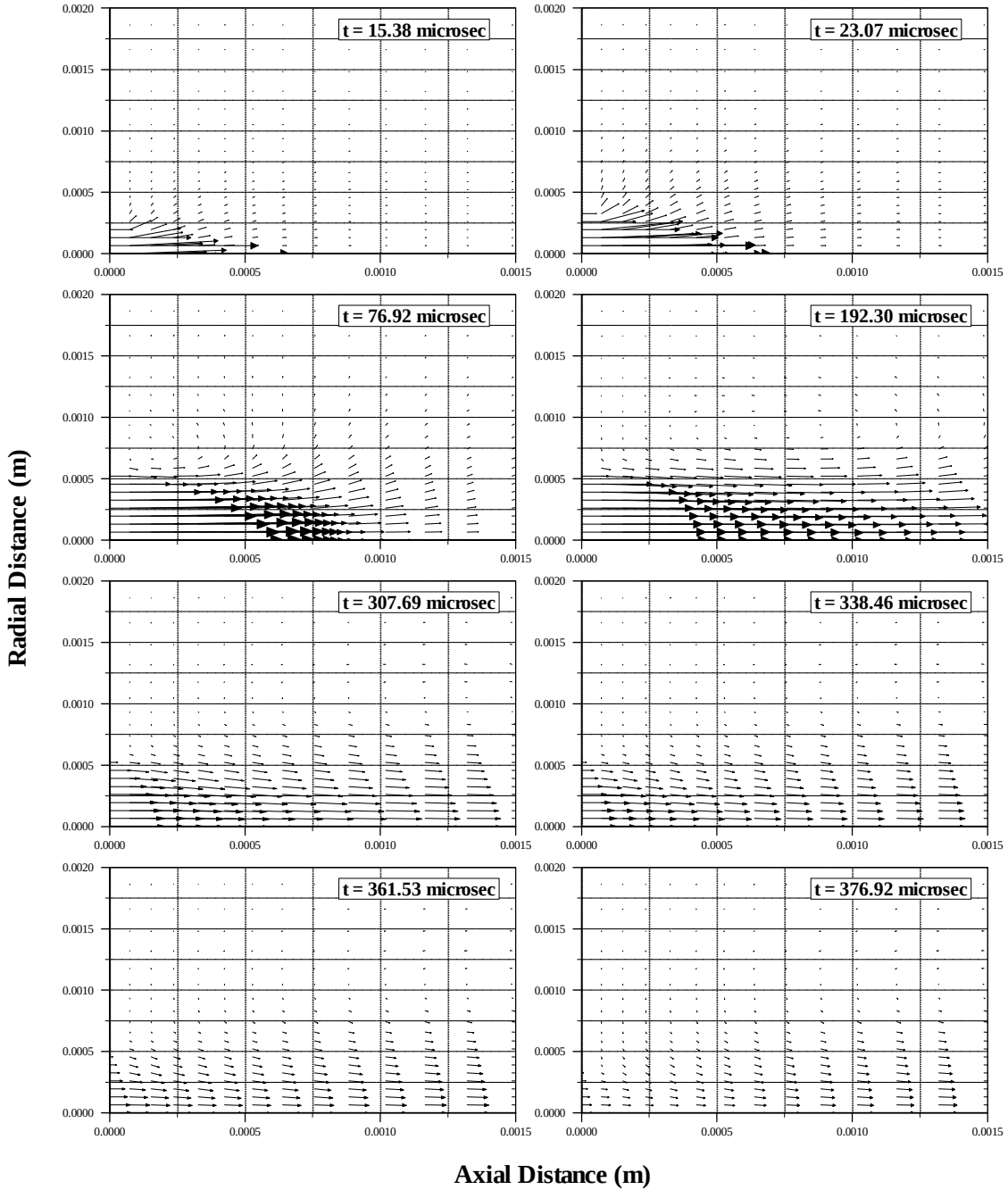

Figure 5.18: Time development of velocity vector plots for an axisymmetric transient turbulent helium jet in the radially expanded and axially contracted region.

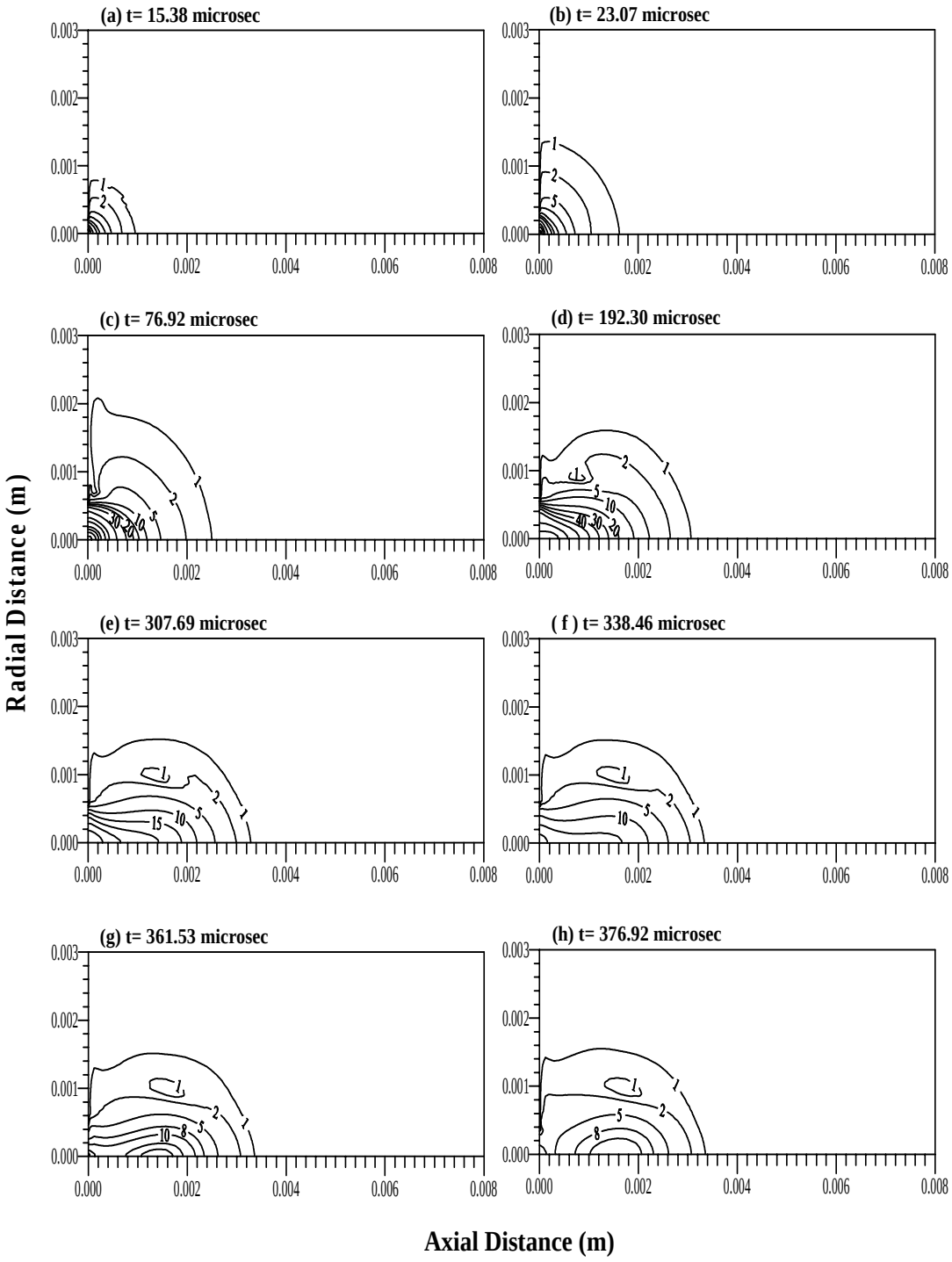

Figure 5.19: Time development of velocity magnitude (m/s) contours for an axisymmetric transient turbulent helium jet expanding into initially stagnant air.

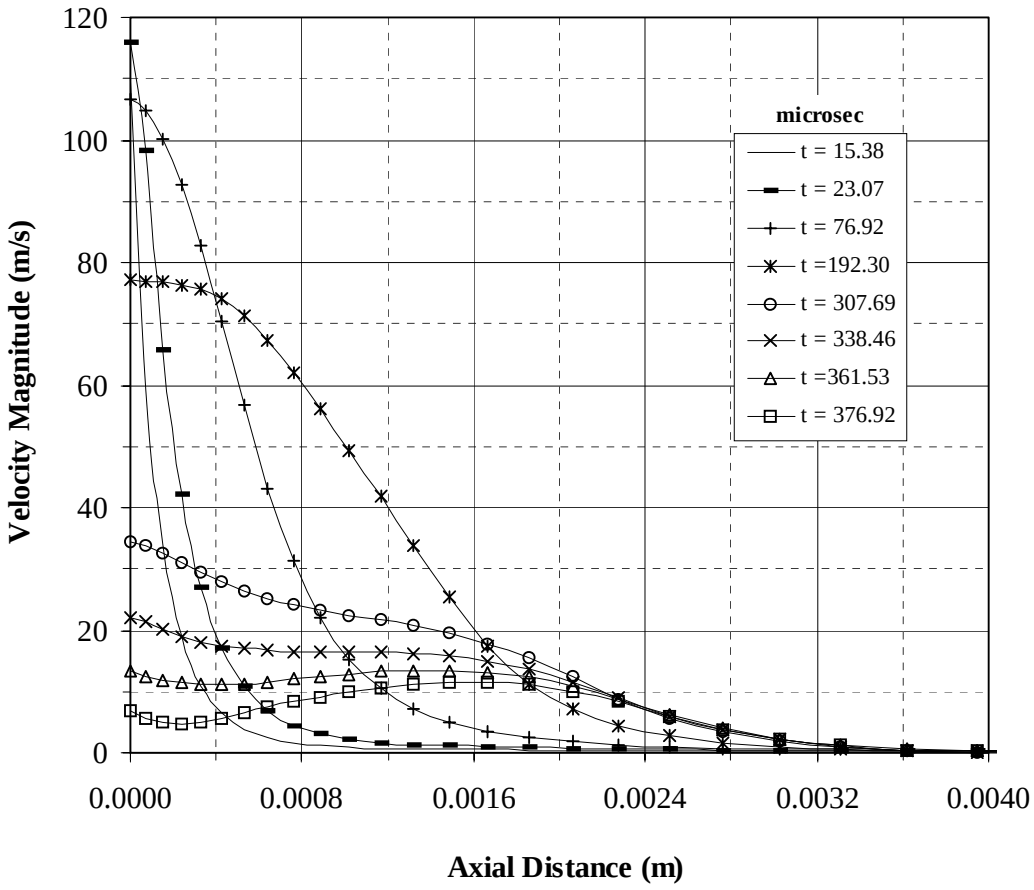

Figure 5.20: Temporal variation of velocity magnitude along the jet symmetry axis at r = 0 m for helium jet expanding into initially stagnant air.

jet expansion in the axial direction. Flow entrainment is evident after $t = 76.92\ \mu s$, in this case, the outer velocity contours differ than those corresponding to earlier time period. Although the jet penetration extends in the axial direction, velocity magnitude reduces considerably with progressing time (Fig. 5.20). This occurs because of the jet exit velocity profile, where the mean velocity reduces significantly (Fig. 5.5). The turbulence kinetic energy is high at the jet exit in the early period. This can be observed from Figure 5.21, in which turbulence kinetic energy along the symmetry axis is shown. This is because of the jet exit velocity profile. It should be noted that the turbulence kinetic energy is associated with the jet exit velocity profile (Eq. (3.34)). The turbulence kinetic energy reduces at jet exit; however, it attains relatively high values along the symmetry axis during $76.92 \leq t \leq 192.30 \mu s$. As the time progresses, its magnitude reduces and does not alter much along the symmetry axis. This indicates that initial jet expansion results in high degree of turbulence and once the jet penetration is progressed, the degree of turbulence reduces significantly. Moreover, changes in jet exit velocity profile results in changes in velocity magnitude along the symmetry axis. This, in turn, causes large variation in turbulence kinetic energy, which was also observed in the previous study [82].

Figure 5.22 shows the pressure contours in the region close to the jet expansion and Figure 5.23 shows the pressure distribution along the symmetry axis. The flow entrainment and formation of circulation cell is evident from the pressure contours, which is more visible after $t = 192.30\ \mu s$. In the early period, jet radial expansion is more than its axial expansion due to the pressure which builds up close to the jet

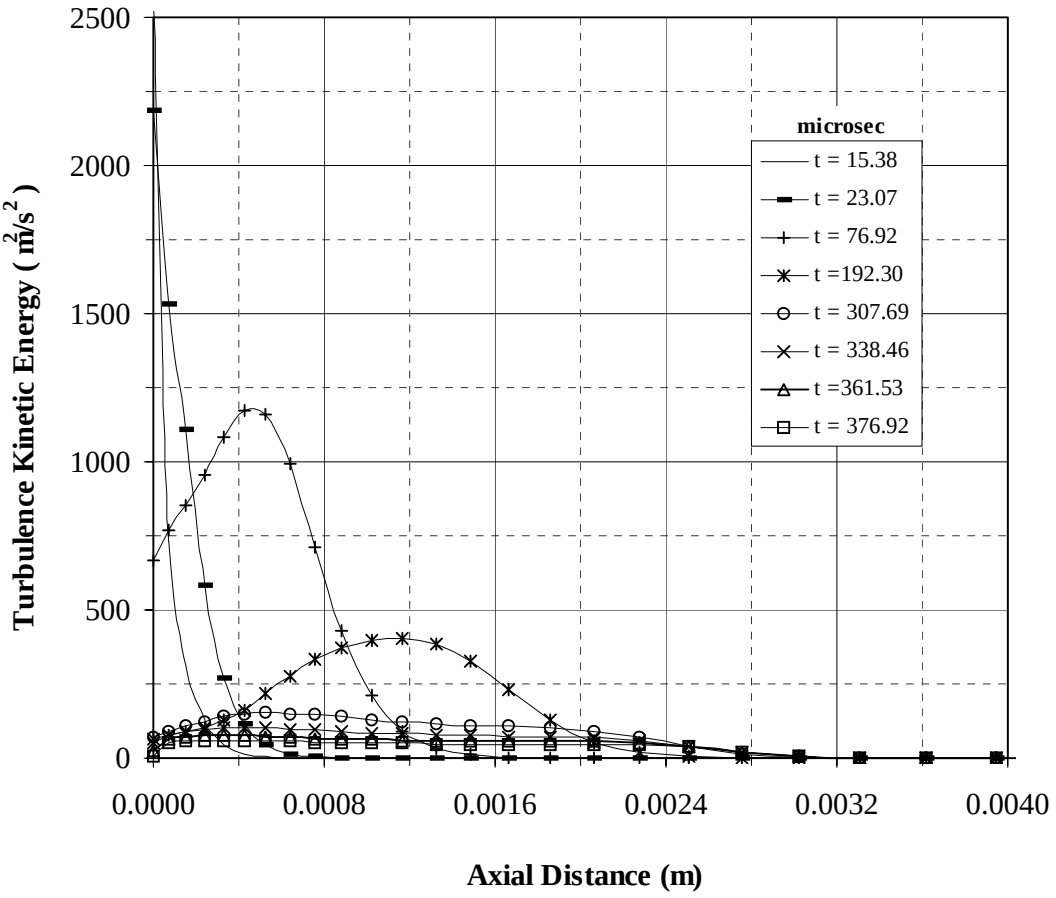

Figure 5.21: Temporal variation of turbulence kinetic energy along the jet symmetry axis at r = 0 m for helium jet expanding into initially stagnant air.

inlet region and as time reaches $t = 192.30\ \mu s$ axial expansion of the jet becomes significant, in which case, the pressure in the jet front region becomes higher than the jet inlet. This implies the shifting of the pressure peak along the symmetry axis with progressing time (Fig. 5.23). As the jet inlet profile becomes almost similar, the pressure magnitude along the symmetry axis does not vary considerably, which in turn results nearly similar pressure profiles along the symmetry axis.

Figure 5.24 shows temperature contours in the region of jet expansion at different times while Figure 5.25 shows variation of temperature along the symmetry axis at different periods. It should be noted that helium jet temperature inletting the control volume is set to 1500 K. Consequently, as the jet expands the high temperature helium results in convection and conduction heating of the ambient air. Moreover, the circulation cell formed next to jet boundary enhances the convective heating of the ambient air. This situation is evident from the temperature contours, i.e., 400 K temperature contour extends considerably into the air ambient. As the magnitude of the jet inlet velocity reduces, which occurs after $t = 307.69\ \mu s$, the region heated by the helium jet still remains hot, but the size of the high temperature region reduces. This shows that the heat transfer from the high temperature jet to its ambient is considerable despite the fact that the time is short. Moreover, due to short period of time, the circulation cell does not convect energy from the heated ambient gas resulting in cooling the ambient gas in this region. When examining Figure 5.25, the temperature profiles almost follow the velocity profiles, provided that as the distance along the symmetry axis increases, the jet front temperature reduces sharply due to

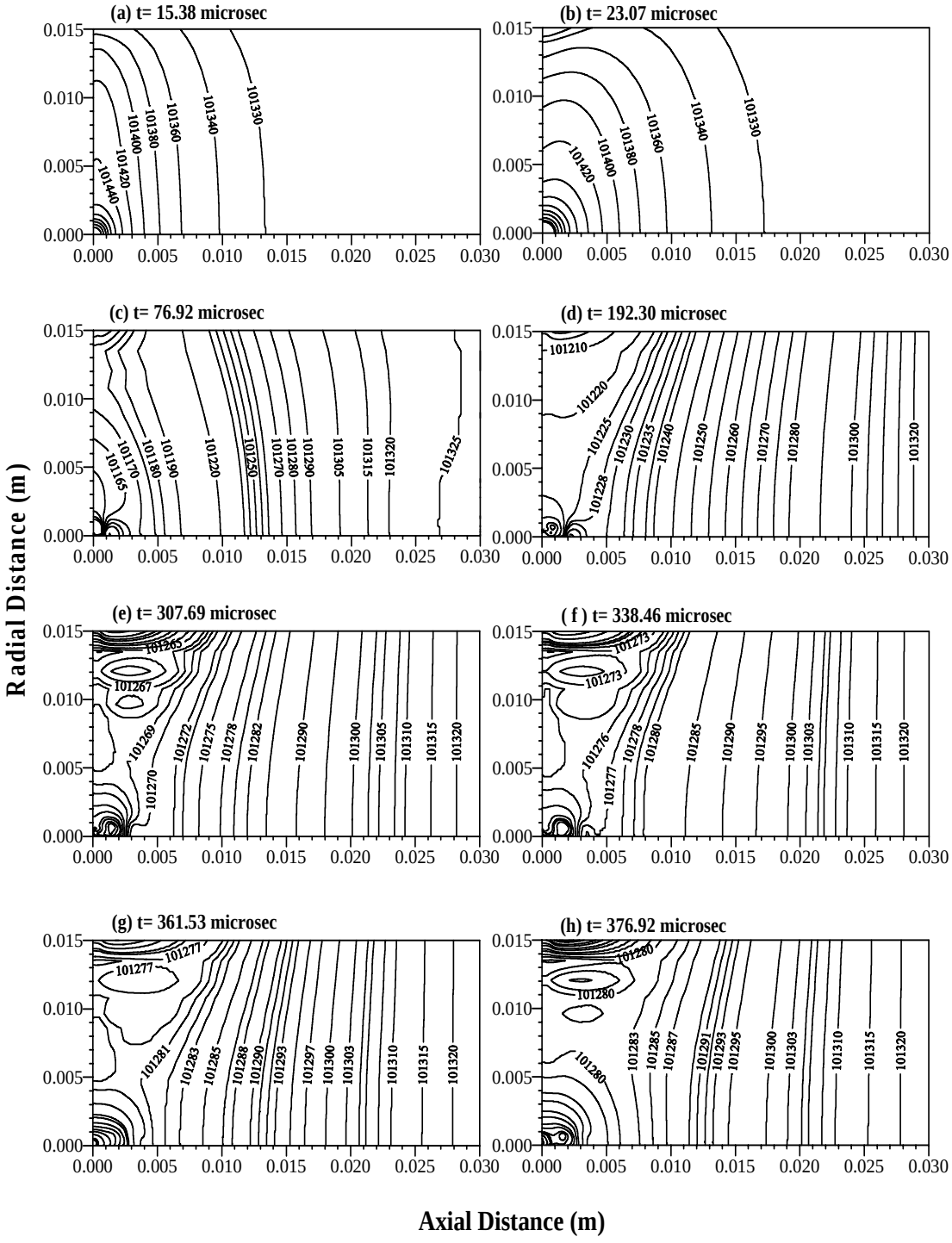

Figure 5.22: Time development of pressure (Pa) contours for an axisymmetric transient turbulent helium jet expanding into initially stagnant air.

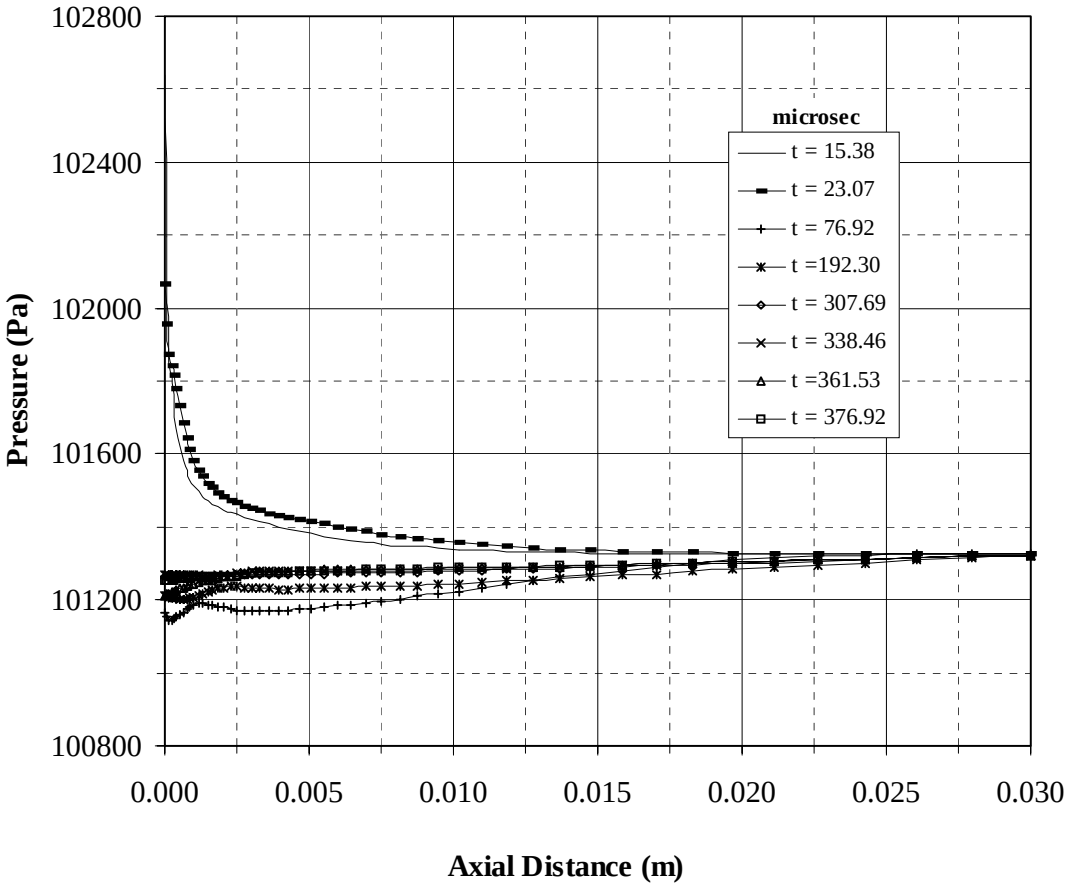

Figure 5.23: Temporal variation of pressure along the jet symmetry axis at r = 0 m for helium jet expanding into initially stagnant air.

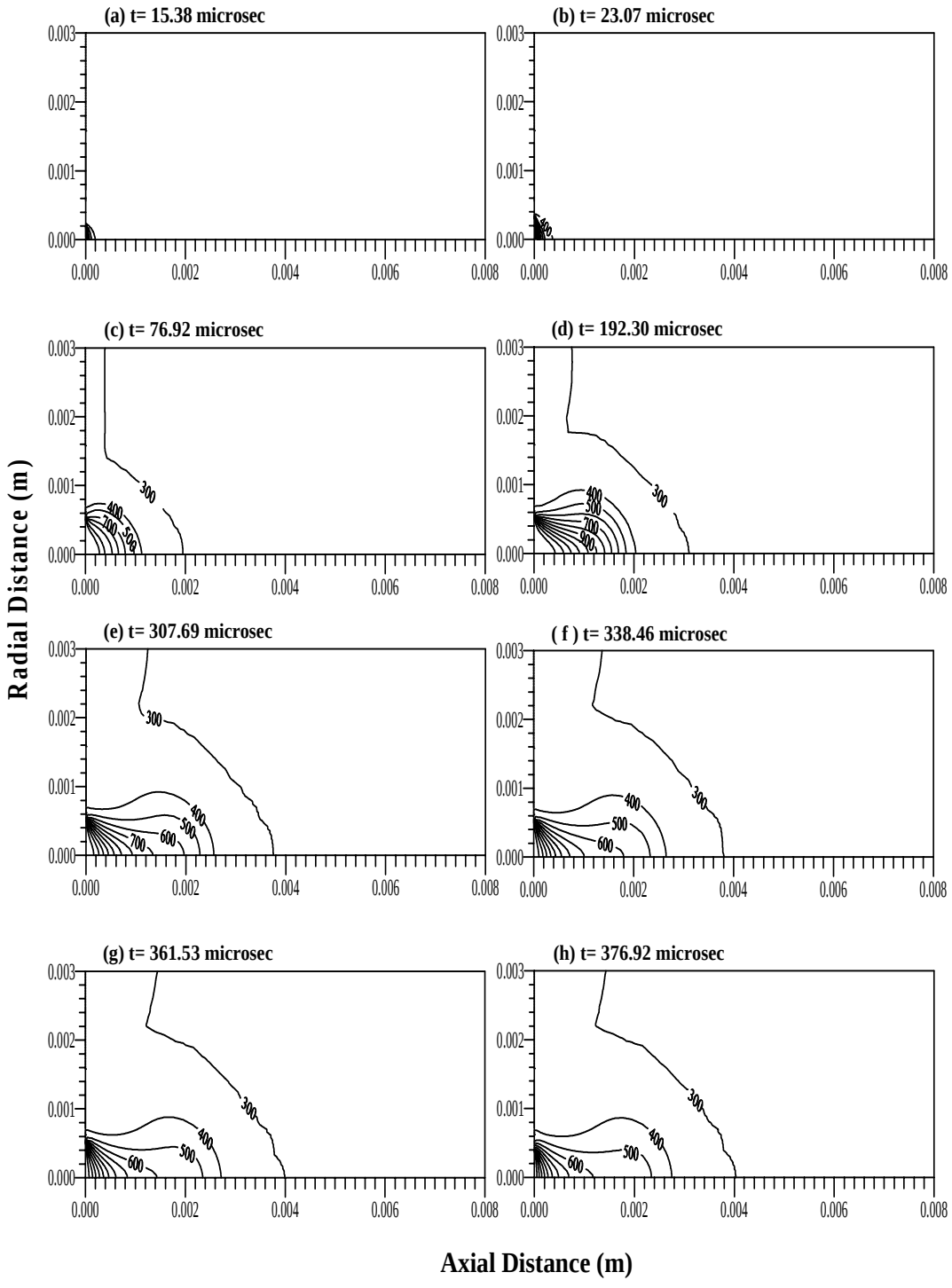

Figure 5.24: Time development of temperature (K) contours for an axisymmetric transient turbulent helium jet expanding into initially stagnant air.

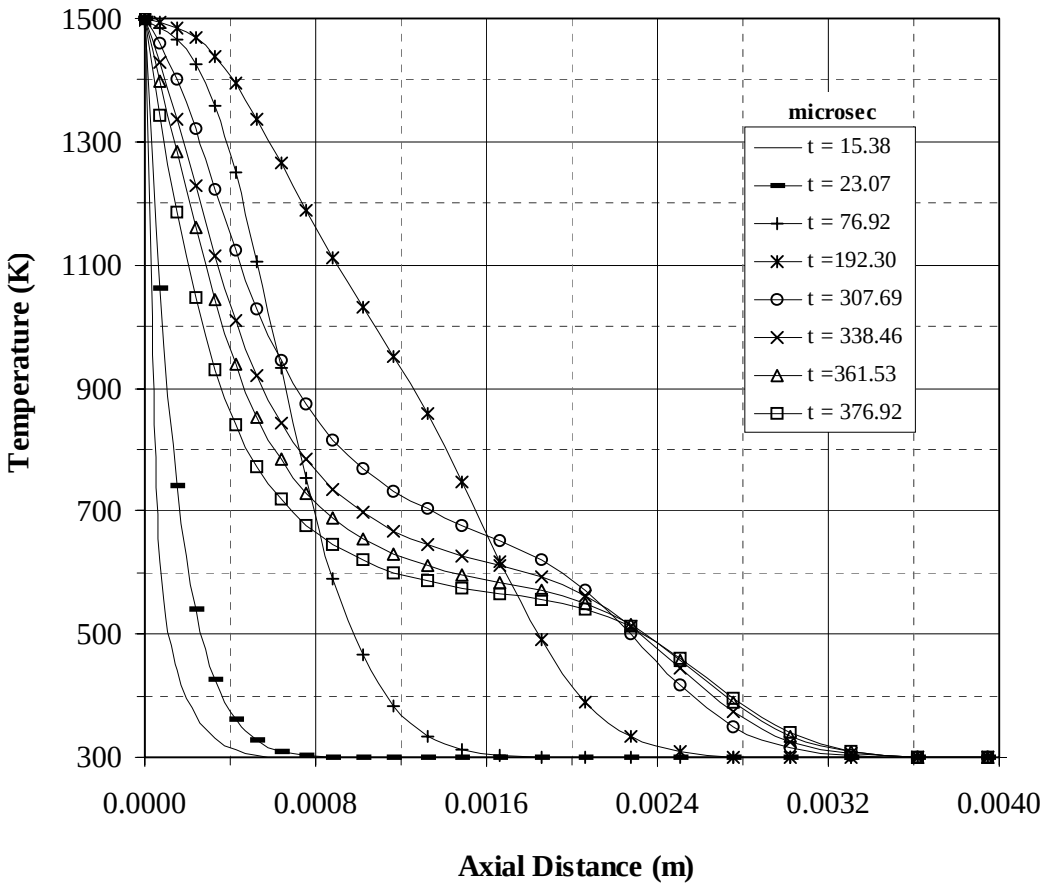

Figure 5.25: Temporal variation of temperature along the jet symmetry axis at r = 0 m for helium jet expanding into initially stagnant air.

heat transfer from jet to its ambient.

Figures 5.26, 5.27 & 5.28 show mass ratio of helium, nitrogen and oxygen along the symmetry axis at different times. Depending on the jet expansion, the helium mass ratio decays sharply along the symmetry axis. However, the deviation in helium mass ratio at different time is because of the jet inlet velocity profile, which changes with time (Fig. 5.5). This is particularly true for the early period ($t \leq 76.92\ \mu s$). Figures 5.27 & 5.28 show N_2 and O_2 mass ratio along the symmetry axis as time variable. The existence of N_2 and O_2 indicates the presence of air. The amount of air present reduces along the symmetry axis as the time period progresses. Moreover, at the jet inlet air does not mix with helium along the symmetry axis for all times concerned. However, mixing of air with helium is evident as the distance along the symmetry axis from the jet inlet increases into the downstream of the jet. This indicates that while the helium jet expands into the stagnant air, some air molecules remain in the region close to the jet inlet. In addition, the expansion of helium into air accelerates the diffusional transport of air into the helium jet.

Figure 5.29 shows mass fraction of helium, nitrogen, and oxygen along the symmetry axis at 192.30 μs. Although the mass fraction of helium close to the helium jet inlet is high, small fraction of nitrogen and oxygen is present there.

The same explanation regarding the enrichment of helium and depletion of nitrogen and oxygen along the symmetry axis can be made if mass fraction contours of helium, nitrogen, and oxygen are considered (Figs. 5.30, 5.31 & 5.32). The only difference is that the radial expansion of the jet cannot be explained using Figures 5.26,

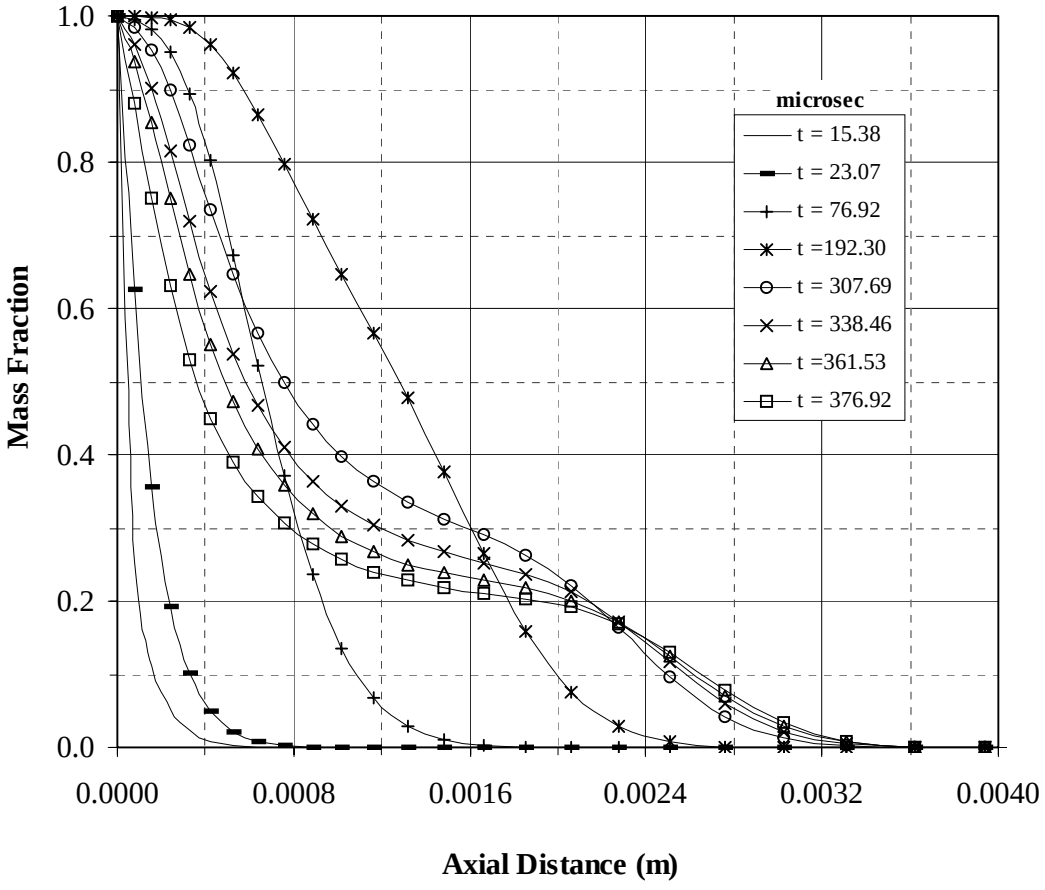

Figure 5.26: Temporal variation of mass fraction of helium along the jet symmetry axis at r = 0 m for helium jet expanding into initially stagnant air.

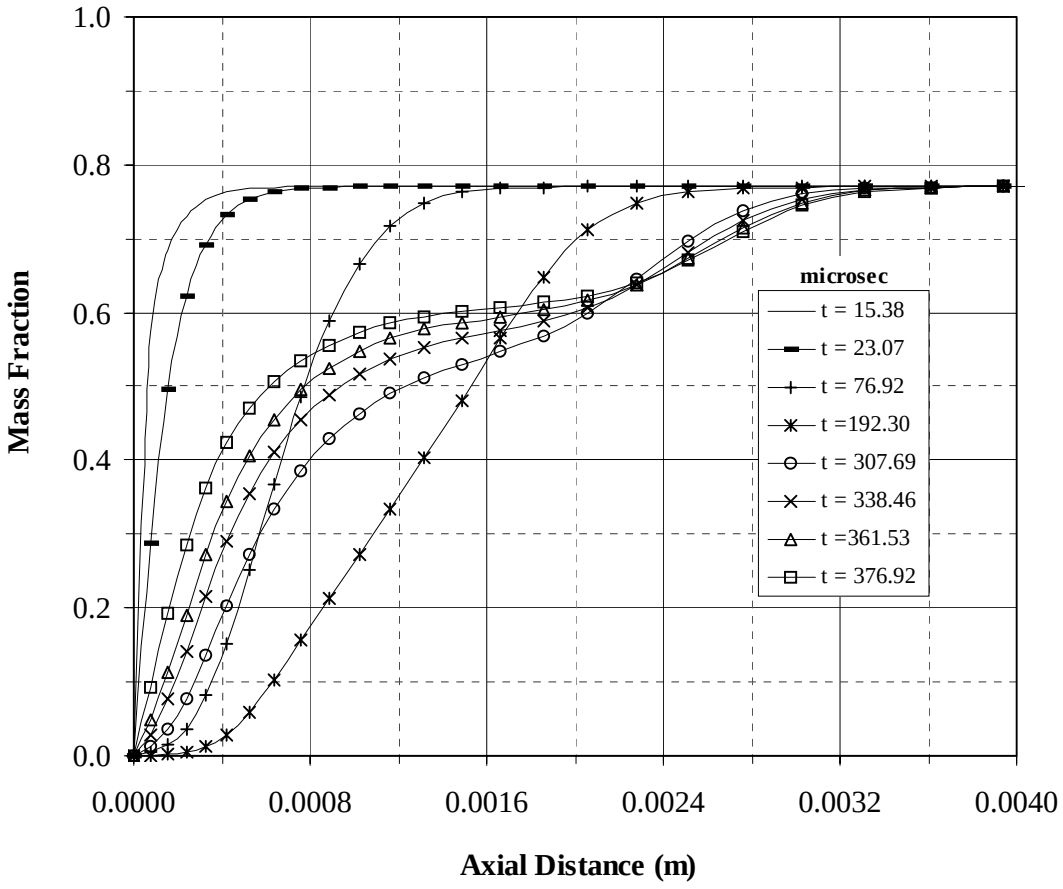

Figure 5.27: Temporal variation of mass fraction of nitrogen along the jet symmetry axis at r = 0 m for helium jet expanding into initially stagnant air.

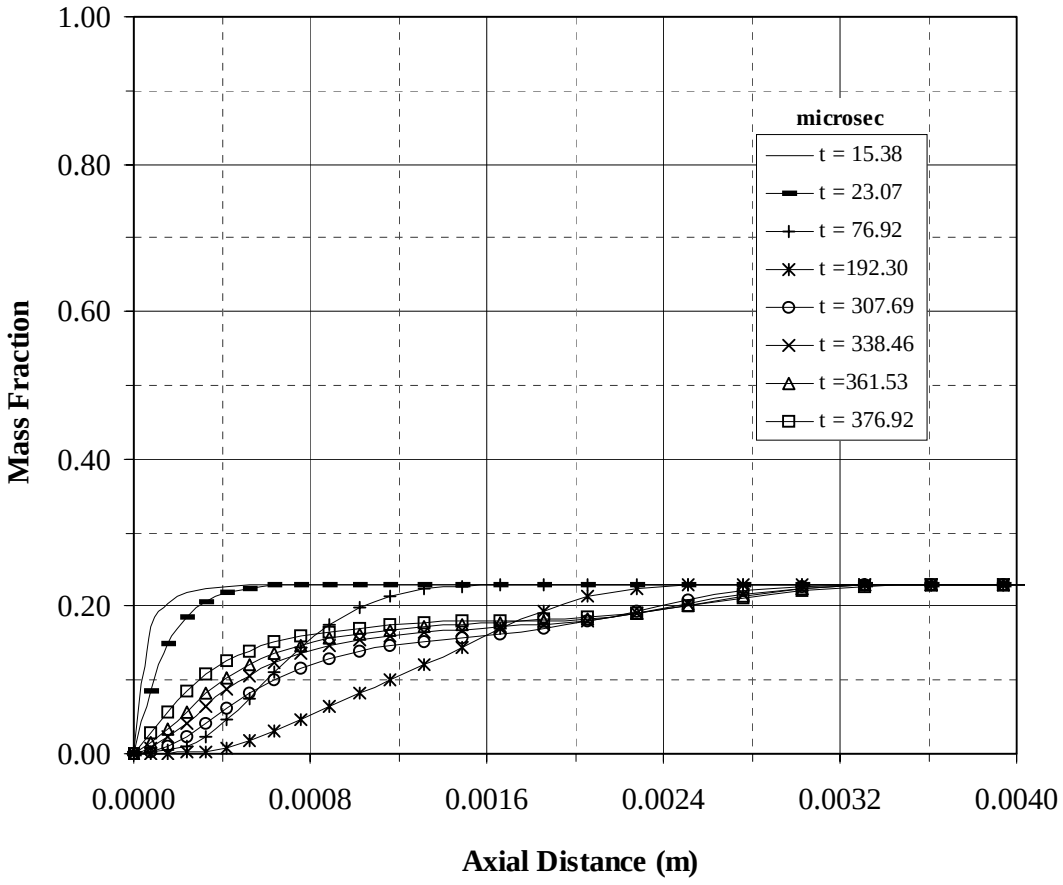

Figure 5.28: Temporal variation of mass fraction of oxygen along the jet symmetry axis at r = 0 m for helium jet expanding into initially stagnant air.

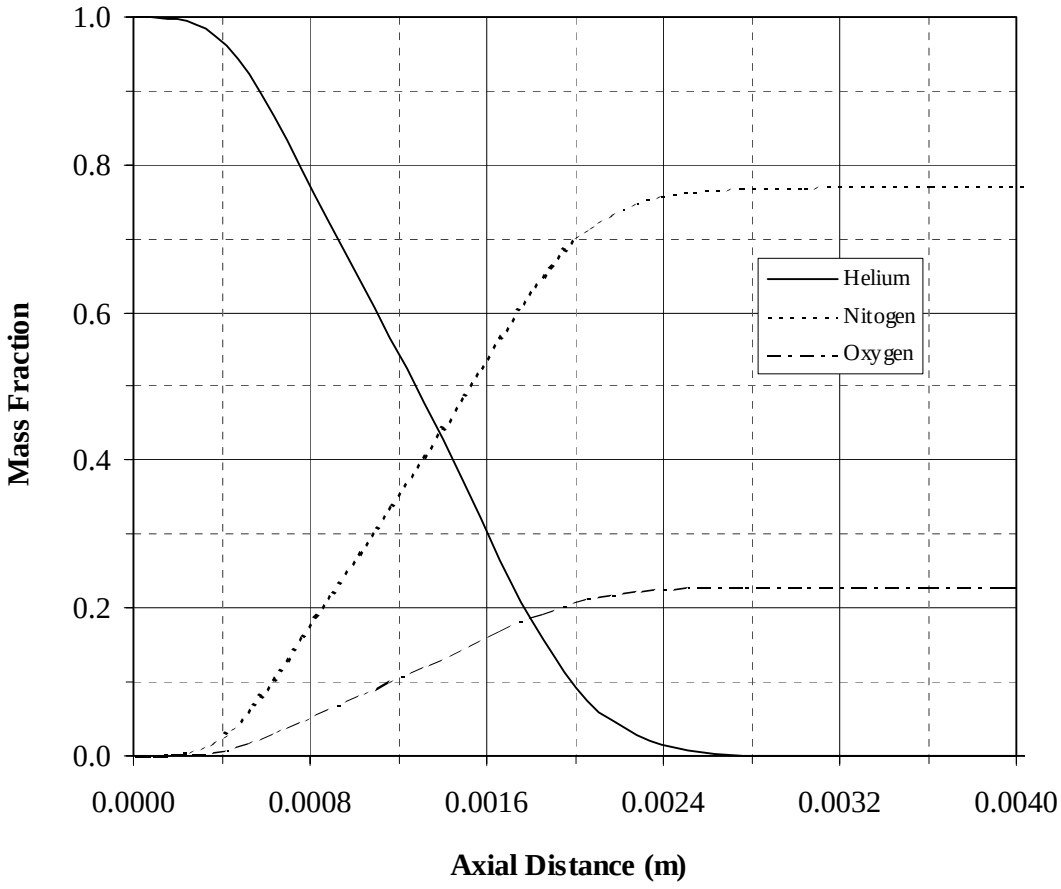

Figure 5.29: Mass fraction of helium, nitrogen and oxygen along the jet symmetry axis at r = 0 m and t = 192.30 microseconds for helium jet expanding into initially stagnant air.

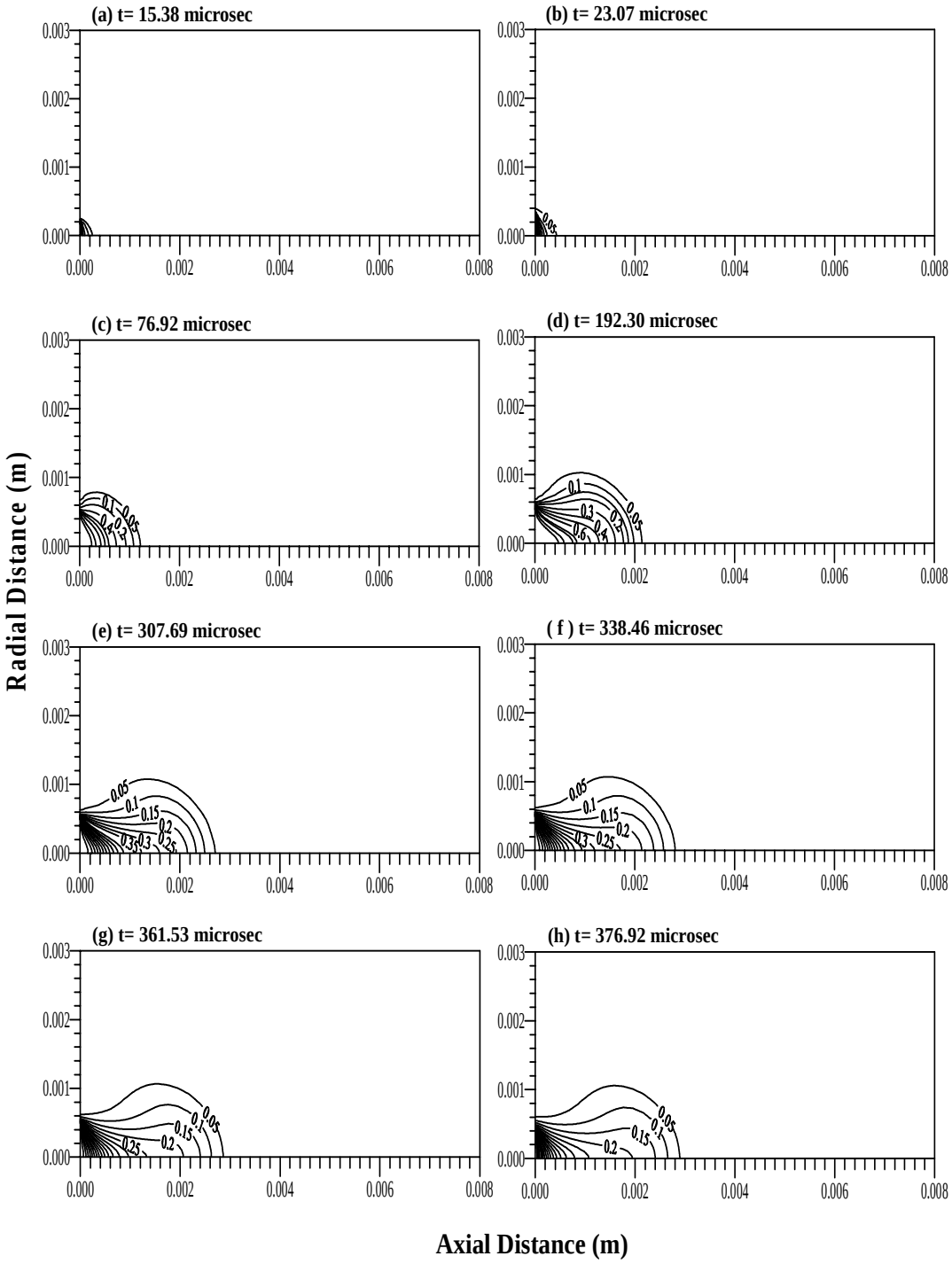

Figure 5.30: Time development of mass fraction contours of helium for an axisymmetric transient turbulent helium jet expanding into initially stagnant air.

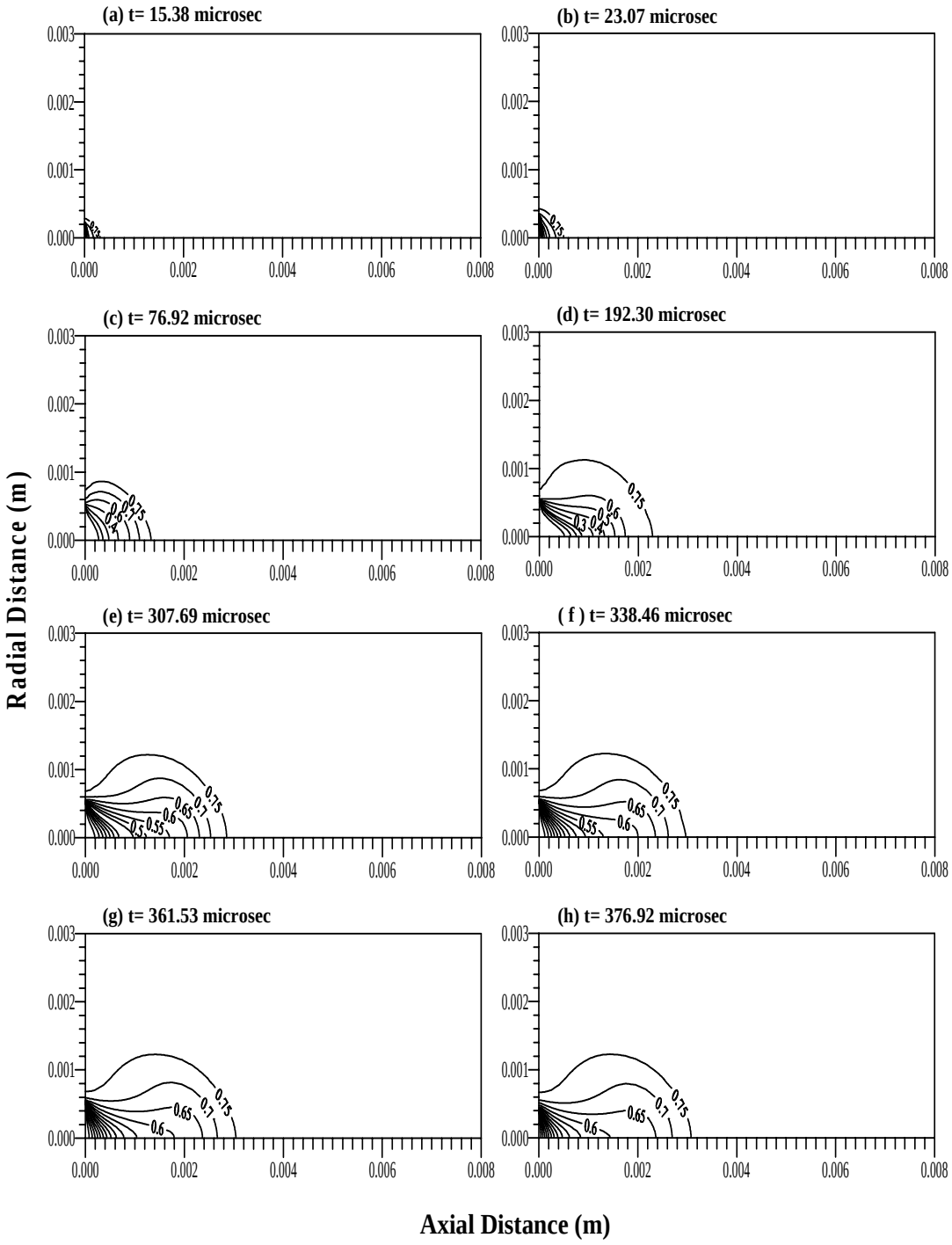

Figure 5.31: Time development of mass fraction contours of nitrogen for an axisymmetric transient turbulent helium jet expanding into initially stagnant air.

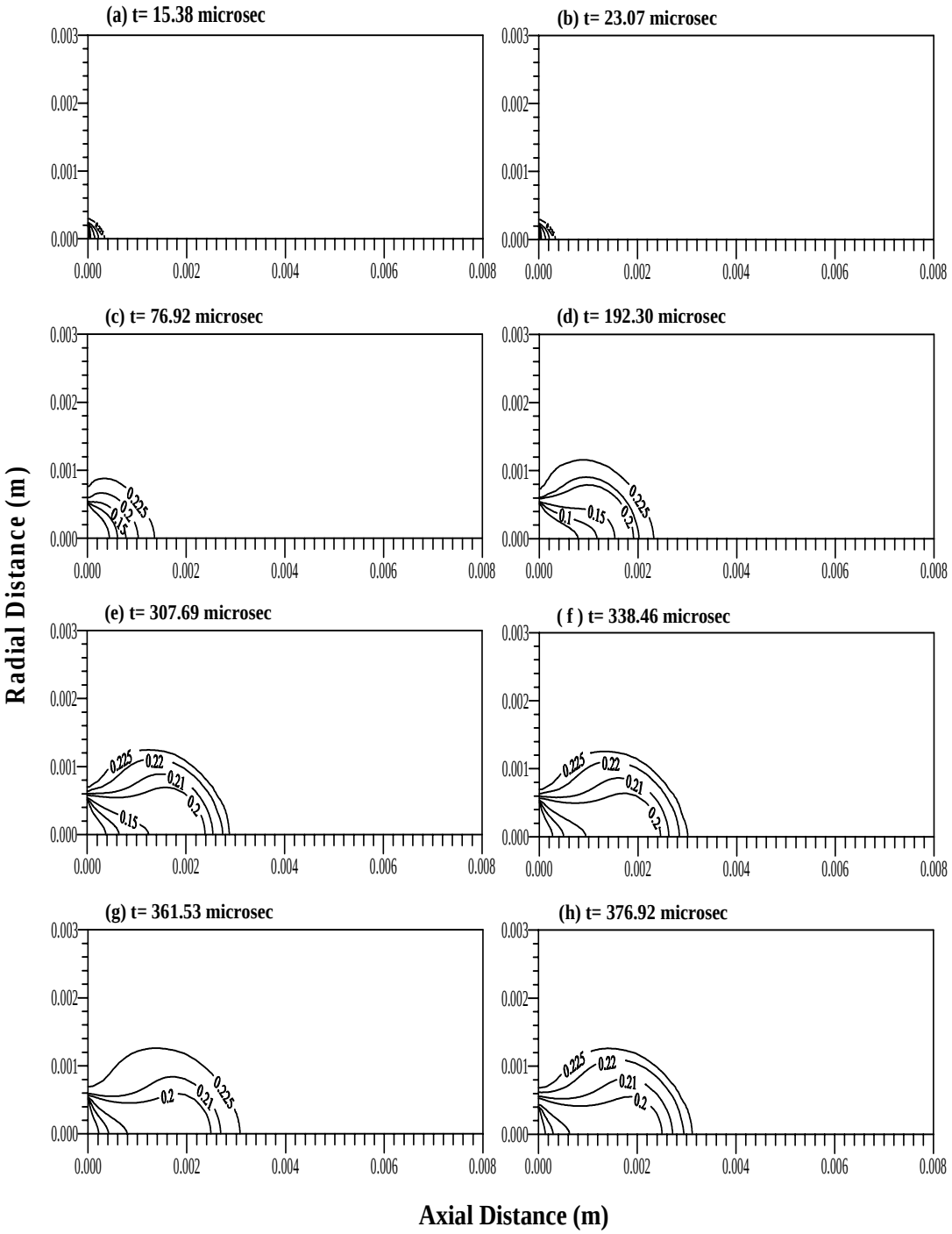

Figure 5.32: Time development of mass fraction contours of oxygen for an axisymmetric transient turbulent helium jet expanding into initially stagnant air.

5.27 & 5.28. In the early period, helium jet expansion is not considerable and this situation is evident by the sharp decay in the mass fraction of helium and sharp rise in the mass fraction of nitrogen and oxygen close to the jet inlet along the symmetry axis for $t \leq 23.07\ \mu s$. As the time progresses the helium jet expands radially as well as axially but when time reaches 192.30 μs axial expansion of the jet becomes significant as compared to the radial expansion. In the later stages of jet expansion, although the axial expansion rate is faster than the radial expansion rate, large diffusion of helium jet into the ambient makes the expansion rate in the axial direction slower than the previous times of dominant axial penetration. This phenomenon enforces the gradual decay in mass fraction of helium and gradual rise in mass fraction of nitrogen and oxygen along the symmetry axis.

Figure 5.33 shows the ratio of jet width to penetration length (D/Z_t) with time. It should be noted that D represents the maximum width of the jet while its maximum axial length is Z_t at each time. The transient jet approaches a self-similar configuration with an asymptotic D/Z_t ratio. In this case, the jet approaches self-similar as D/Z_t becomes 0.65. The similar situation is observed by Hill and Ouellette [29], provided that D/Z_t obtained is less than the present finding. This is due to different jet inlet configurations. Moreover, the transition length appears to be about 3 jet inlet diameters, less than the data reported earlier for steady jet [83]. In the early period ($t \leq 76.92\ \mu s$), jet is transient and it is nowhere self-similar in the flow field. This is because of the jet inlet velocity profile, which is developing with time as shown in Figure 5.5. As the jet inlet velocity profiles become almost similar the attainment

of self-similarity in the flow field becomes possible.

Figure 5.34 shows the variation of ratio of penetration length (Z_t) to $\frac{1}{4}$ power of momentum rate per unit density $\left(\dot{M}_{He}/\overline{\rho}\right)$ with $\sqrt{t}$. The dimensionless quantity $\frac{Z_t}{\left(\dot{M}_{He}/\overline{\rho}\right)^{1/4}\times\sqrt{t}}$ represents the penetration number [29,32], where $\dot{M}_{He}$ is the total exit momentum flow rate. It should be noted that for the transient jet, the penetration is a linear function of $\sqrt{t}$, i.e., $\frac{Z_t}{\left(\dot{M}_{He}/\overline{\rho}\right)^{1/4}\times\sqrt{t}} = constant$. It can be observed that during $\sqrt{t} \leq 14\sqrt{\mu s}$, the slope of the curve remains almost the same. As the time progresses, the slope of the curve increases and varies with increasing $\sqrt{t}$. Consequently, to achieve a constant penetration number during the jet expansion is almost impossible in the present study, because of variation in momentum flow into the control volume during the jet expansion. However, the slope of the curve during the period $6\sqrt{\mu s} \leq \sqrt{t} \leq 14\sqrt{\mu s}$ is similar to that obtained from the previous study [84].

5.2.3 Comparisons of Results Obtained Due to Transient Air and Helium Jets

In order to compare the transient jet behavior due to air and helium jets, jet penetration properties are considered when comparing Figures 5.15 and 5.33 in which ratio of jet width to penetration length (D/Z_t) with time are shown. Although the behavior of (D/Z_t) with time is similar, the slopes of both curves vary considerably. In this case, the slope of transiently expanding helium jet results in higher slope [$\Delta(D/Z_t)/\Delta t$] than air jet. This indicates that air jet penetrates more into its ambient

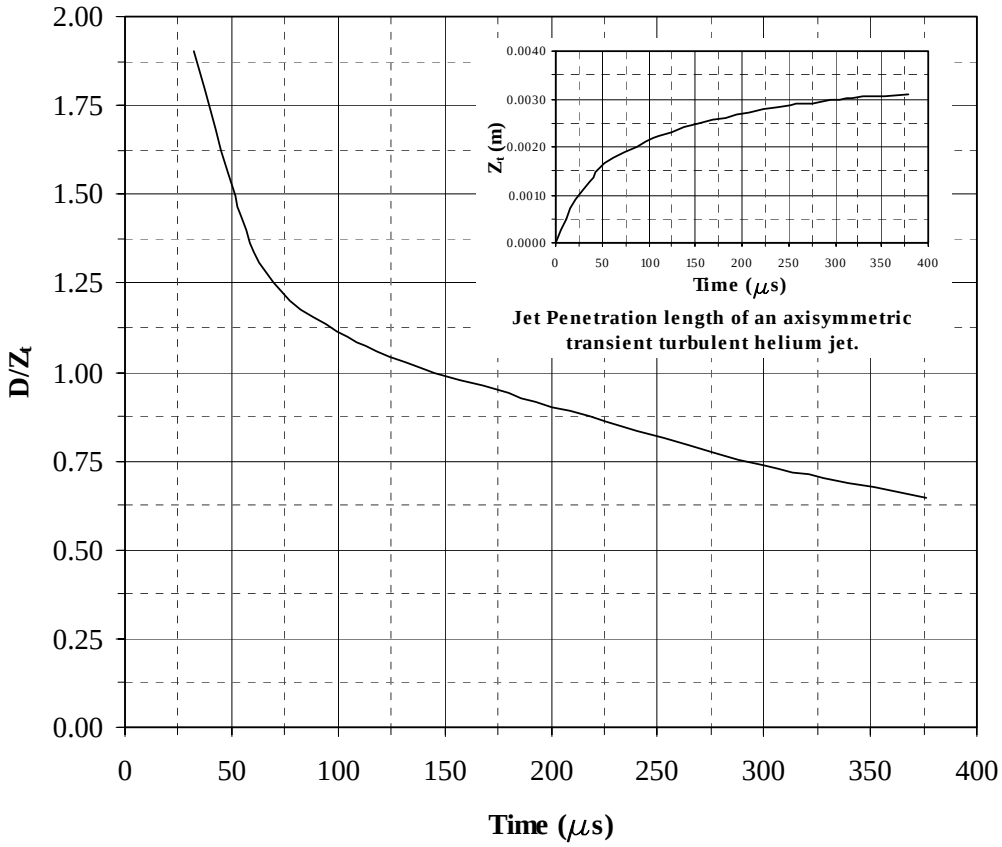

Figure 5.33: Ratio of jet width to penetration length with time for an axisymmetric transient turbulent helium jet expanding into initially stagnant air.

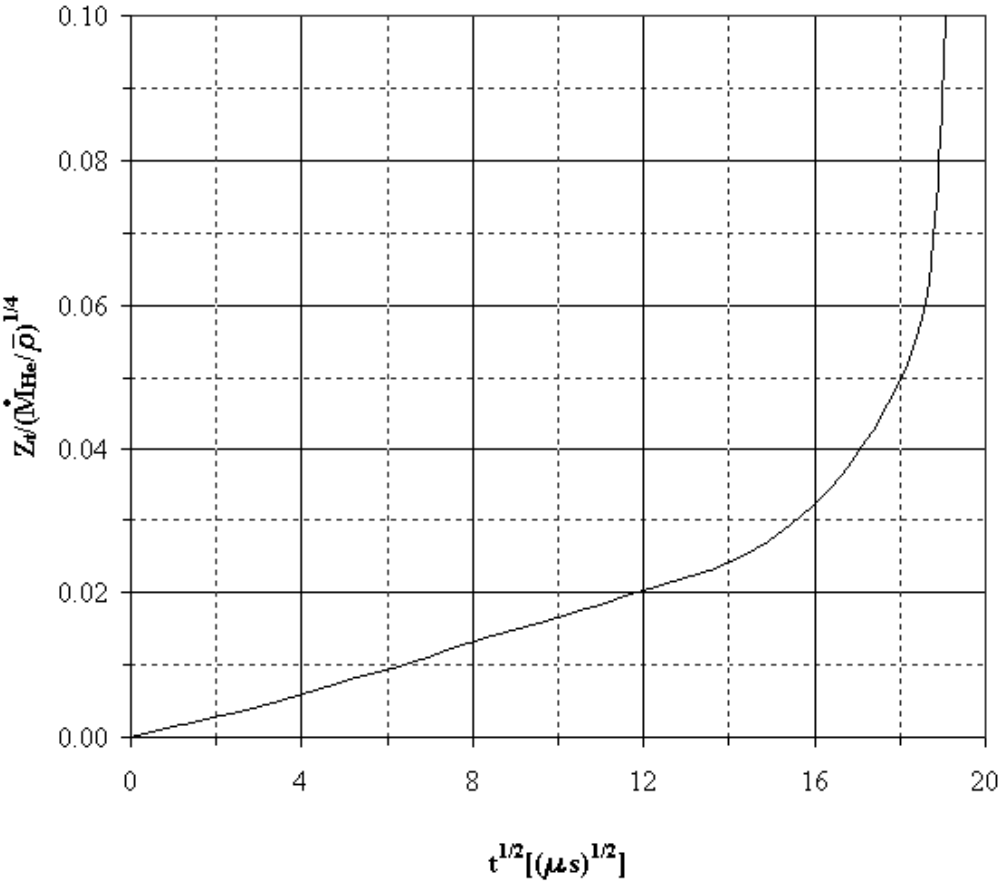

Figure 5.34: Penetration rate of an axisymmetric transient turbulent helium jet exiting into initially stagnant air.

than the helium jet. This occurs because of the density of the helium, which is lower than the air. This can also be observed from temperature curves (Figs. 5.13 & 5.25). In the case of penetration number, both jets behave similarly (Figs.5.34 & 5.16), provided that longer expansion of the air jet results in larger gradients $\left[\Delta(Z_t/\overline{\rho}\,\dot{M})^{1/4}/\Delta\sqrt{t})\right]$. This, is, again due to the thermophysical properties of the fluids, which differ considerably. It should be noted that helium has the density almost 1/10 of air. Consequently, the momentum of helium jet onset of leaving the solid surface is considerably smaller than that corresponding to air jet, despite the fact that both jets have the same transiently varying velocity profiles at this location. Moreover, the specific heat capacity of helium is almost 5 times higher than the air. It is, therefore, expected that the convective heating of the ambient gas by the transient jet is higher in the case of helium. Since the inlet momentum of helium jet is lower than the air jet, this situation is not reflected in temperature contours in the region next to helium jet (Fig. 5.24).

5.3 Opposing Jets

In practical laser heating process an assisting gas jet coaxial with the laser-heating source impinges onto the transiently developing vapor jet emanating from the irradiated solid surface. In the next phase of the present study, a high temperature transiently developing helium jet, resembling the vapor ejection from a laser induced surface, and an opposing steady air jet, resembling the assisting gas jet, are studied. Since the thermophysical properties of the evaporating surface are not known in

the open literature, helium at 1500 K (imitating the evaporating temperature of the laser-irradiated solid) is considered as the transiently developing jet. This enforces the assumption that the transiently developing helium and steady air jets behave like perfect gases. Using helium, which is different from the laser irradiated vapor, and air at such a high temperature as perfect gases may not give the complete answer; however, it enables to demonstrate the quantitative behavior of the opposing jets-situation which is caused by the impingement of the assisting gas jet with the vapor jet. Moreover, the velocity profile of the transiently developing vapor jet measured previously by Yilbas et al [78] is used as the velocity profile of the transiently developing helium jet at one inlet to the control volume (inlet 1), and $\frac{1}{7}th-$ power velocity profile is used as the velocity profile of the steady air jet (assisting gas jet) at the second inlet to the control volume (inlet 2). Figure 5.5 shows the velocity profiles of the transiently developing vapor jet. Furthermore, since the flow field is actually generated by the opposing of the high velocity transiently developing helium and steady air jet and the flow field is mainly of interest in the near wall region, therefore low Reynolds number $k-\epsilon$ model is used to accommodate turbulence in the simulations. In this phase of the study, the transient effect and the influence of the assisting gas velocity on the flow, temperature, pressure, and species mass fraction fields are discussed.

5.3.1 Transient Effect on The Flow Field Due to Opposing Jets

Opposing jet situation resembling the laser gas assisted processing is discussed. The transiently developing jet resembling the laser-induced vapor plume and the steady jet impinging onto the transiently developing jet are considered. The geometric configurations of the jets are selected in accordance with the actual laser processing conditions.

Figure 5.35 shows velocity vectors in the region close to the transiently developing jet region for different periods. The transiently developing jet penetrates into steady opposing jet during the early period ($t \leq 23.07\ \mu s$). As the transiently developing jet size increases in the radial direction, the opposing jet suppresses the penetration of the jet in the axial direction. In this case, a circulation cell next to the steady jet boundary and close to the transient jet is developed ($t = 76.92\ \mu s$). As the time progresses further ($t = 192.30\ \mu s$), radial extension of the transiently developing jet enhances, which in turn accelerates the radial flow in the region close to the solid wall. Consequently, the orientation of the circulation cell changes and it moves away from the steady jet boundary. In this case, transiently developing jet velocity develops further in the radial direction and its velocity profile enables the impinging jet to spread radially in the region close to the impinging jet. As the time progresses further ($t \geq 361.53\ \mu s$), the average velocity of the transiently developing jet reduces and the impinging jet suppresses further penetration of the transiently developing jet and

enhanced radial flow close to the wall ensures the steady jet expansion in this region. The radial expansion of the steady jet at $t \geq 361.53\ \mu s$ is also observed from Figure 5.36, in which velocity magnitude contours are shown. The size of the circulation cell grows as time progresses. It should be noted that the transiently developing jet profiles at control volume inlet changes with time. Consequently, its effect on the size and orientation of the circulation cell varies with time.

Figure 5.37 shows the pressure contours in the region close to the transiently developing jet. The high magnitude pressure contours extend into the steady jet region along the axial direction during the early period. This indicates that a triangle like transiently developing jet velocity profile penetrates deeper into the steady impinging jet. As the time progresses, the transiently developing jet expands radially, which in turn influences streamline curvature of the steady impinging jet. Consequently, transiently developing jet penetration into the steady jet region is suppressed by the stagnation region developed in the vicinity of transiently developing jet boundary. This enhances the development of the radial flow; therefore, a circulation cell is formed next to the steady jet boundary, provided that the pressure field gradually reduces in this region. In the case of $t = 376.92\ \mu s$, the appearance of pressure contour ($101.270\ KPa$) may suggest the formation of the secondary cell close to the developing jet boundary. However, close examination of velocity contours and velocity vectors indicate that the flow mixing in this region occurs and formation of secondary cell is unlikely.

Figure 5.38 shows helium mass fraction contours in the region close to the tran-

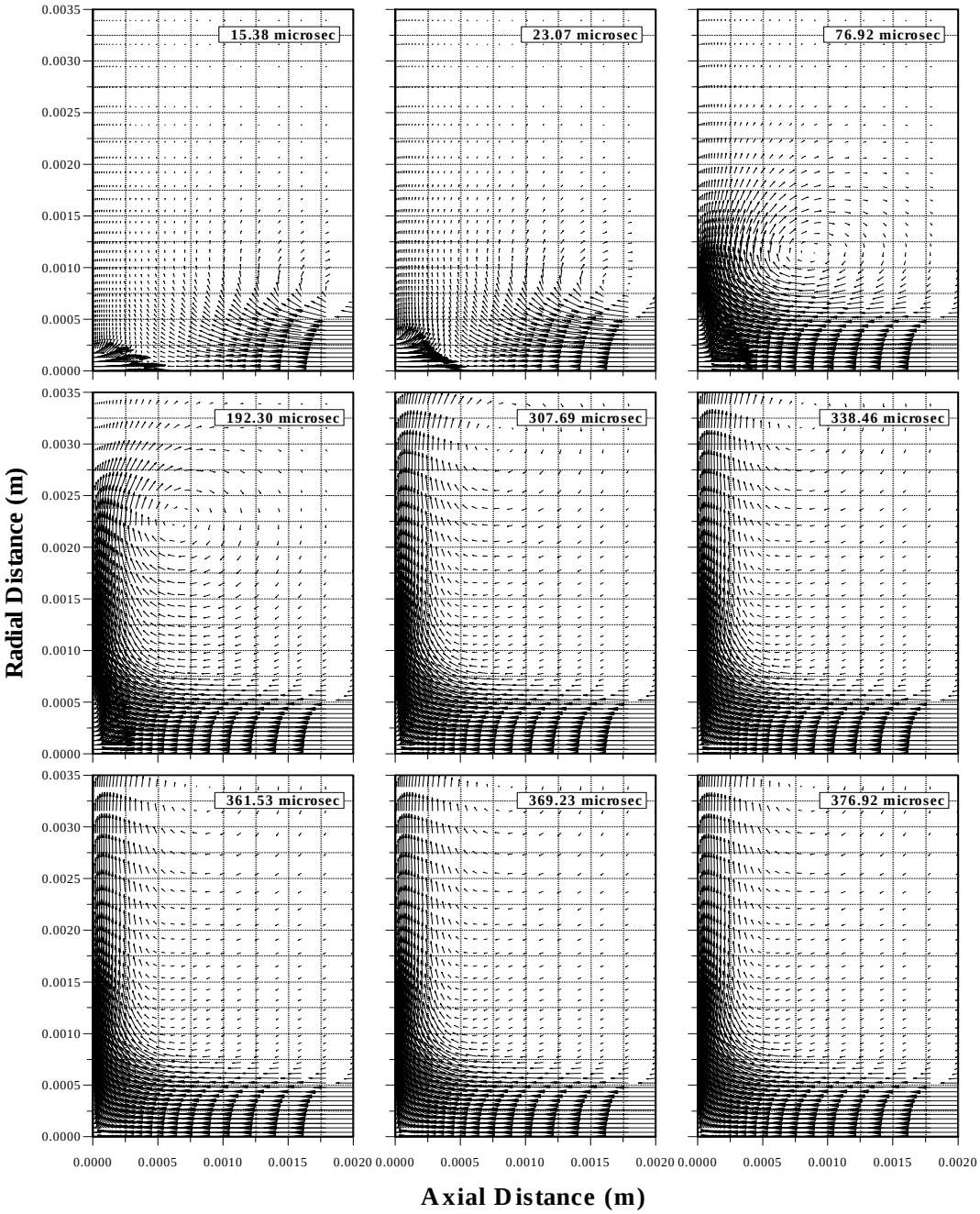

Figure 5.35: Time development of velocity vector plots of He-air mixture for an axisymmetric transiently developing helium jet opposing the steady air jet at air jet velocity of 100 m/s.

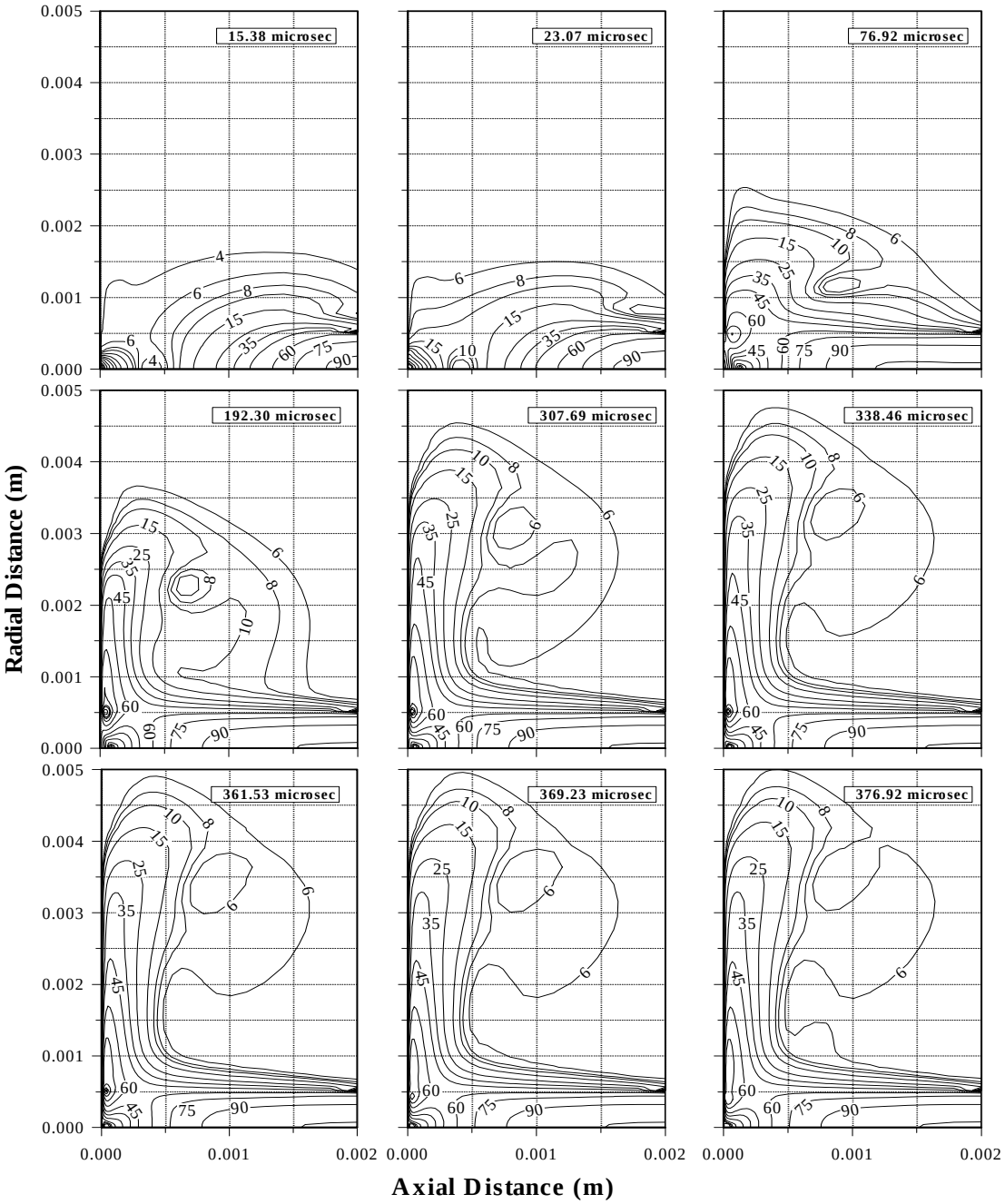

Figure 5.36: Time development of velocity magnitude (m/s) contours of He-air mixture for an axisymmetric transiently developing helium jet opposing the steady air jet at air jet velocity of 100 m/s.

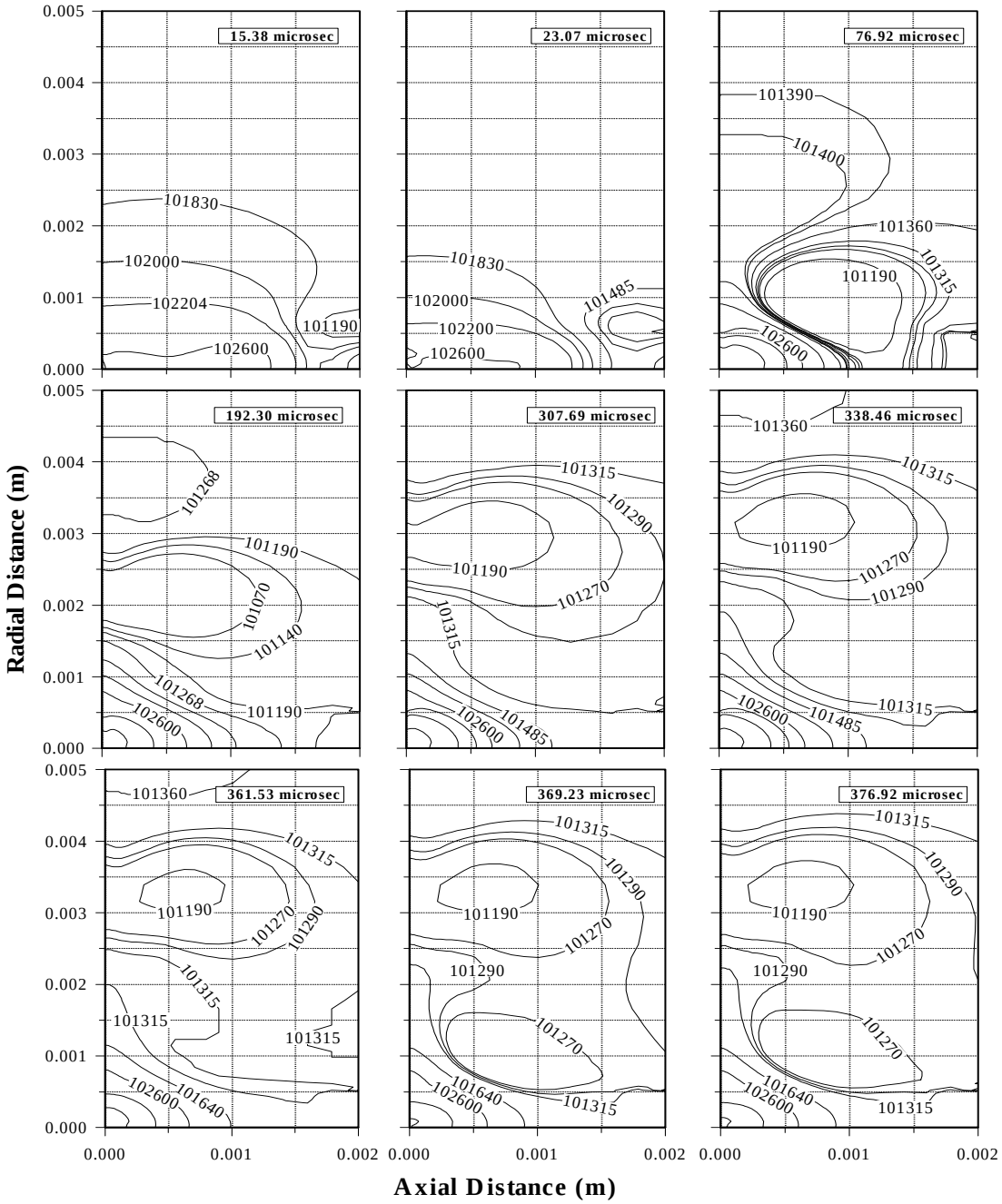

Figure 5.37: Time development of pressure (Pa) contours of He-air mixture for an axisymmetric transiently developing helium jet opposing the steady air jet at air jet velocity of 100 m/s.

siently developing jet. In the early time when transiently developing jet axially extends into the steady impinging jet, helium mass fraction is higher close to the transiently developing jet entering region. As the time progresses, radial expansion of the transient jet and flow mixing in the region next to the transient jet boundary lower the helium mass fraction while increase the nitrogen mass fraction (Fig.5.39). Moreover, mass fraction of helium is suppressed further by the steady impinging jet for $t = 376.92\ \mu s$. In the case of nitrogen mass fraction (Fig.5.39), nitrogen mass fraction reduces in the region close to the transient jet. This is more pronounced in the early times. Moreover, flow mixing close to the transient jet boundary enhances the nitrogen mass fraction in this region, which is clearly observed for $t \geq 307.69\ \mu s$. It should be noted that the impinging steady jet is air, which composes of oxygen and nitrogen. The presence of nitrogen indicates the presence of air in the flow field.

Figure 5.40 shows temperature contours in the region close to the transient jet. Transiently developing helium jet is at 1500 K at the onset of emanating from the wall (cavity wall) while steady impinging jet temperature is 300 K at the jet entry. Consequently, transiently developing jet core temperature remains high while at the mixing region temperature of the steady jet increases due to the convective and conductive heat transfer in the mixing region. In the early period $t = 15.38\ \mu s$, although the transient jet expands axially into the steady jet, temperature across the transient jet boundary does not attain high values. Moreover, transient jet core temperature extends further into the steady jet at $t = 23.07\ \mu s$. Due to radial extension of the transiently developing jet and modification of streamline curvature

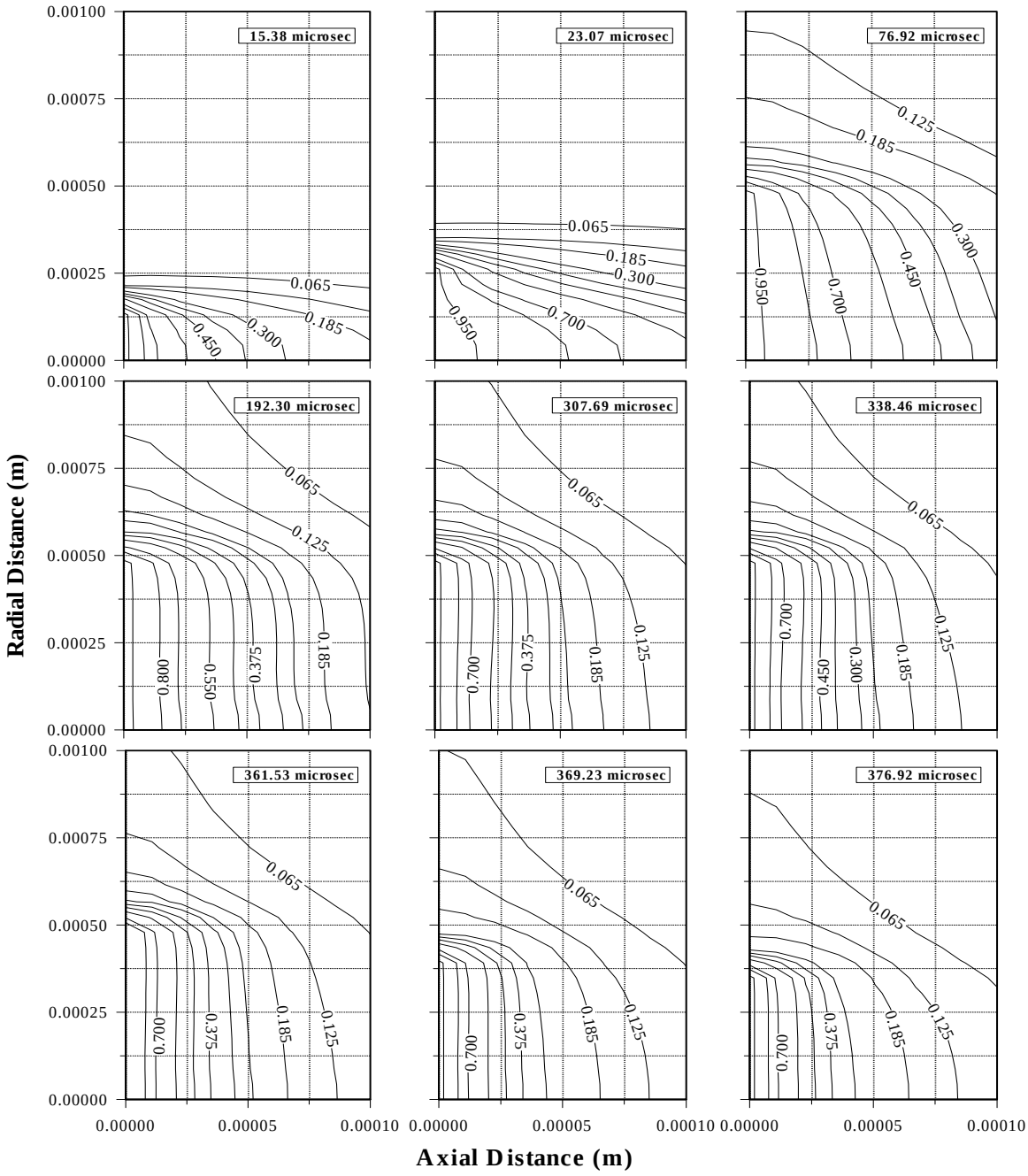

Figure 5.38: Time development of mass fraction contours of helium in He-air mixture for an axisymmetric transiently developing helium jet opposing the steady air jet at air jet velocity of 100 m/s.

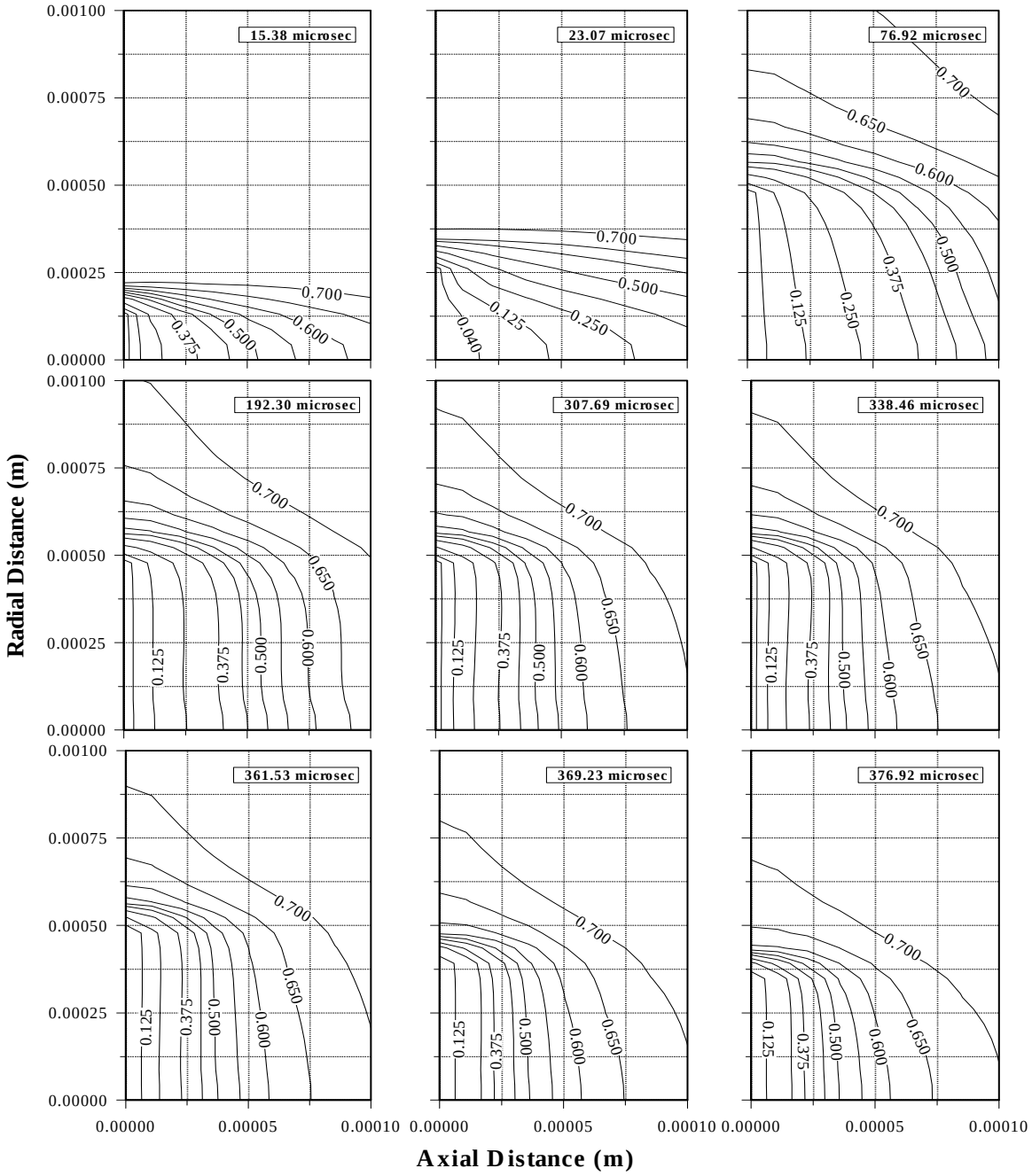

Figure 5.39: Time development of mass fraction contours of nitrogen in He-air mixture for an axisymmetric transiently developing helium jet opposing the steady air jet at air jet velocity of 100 m/s.

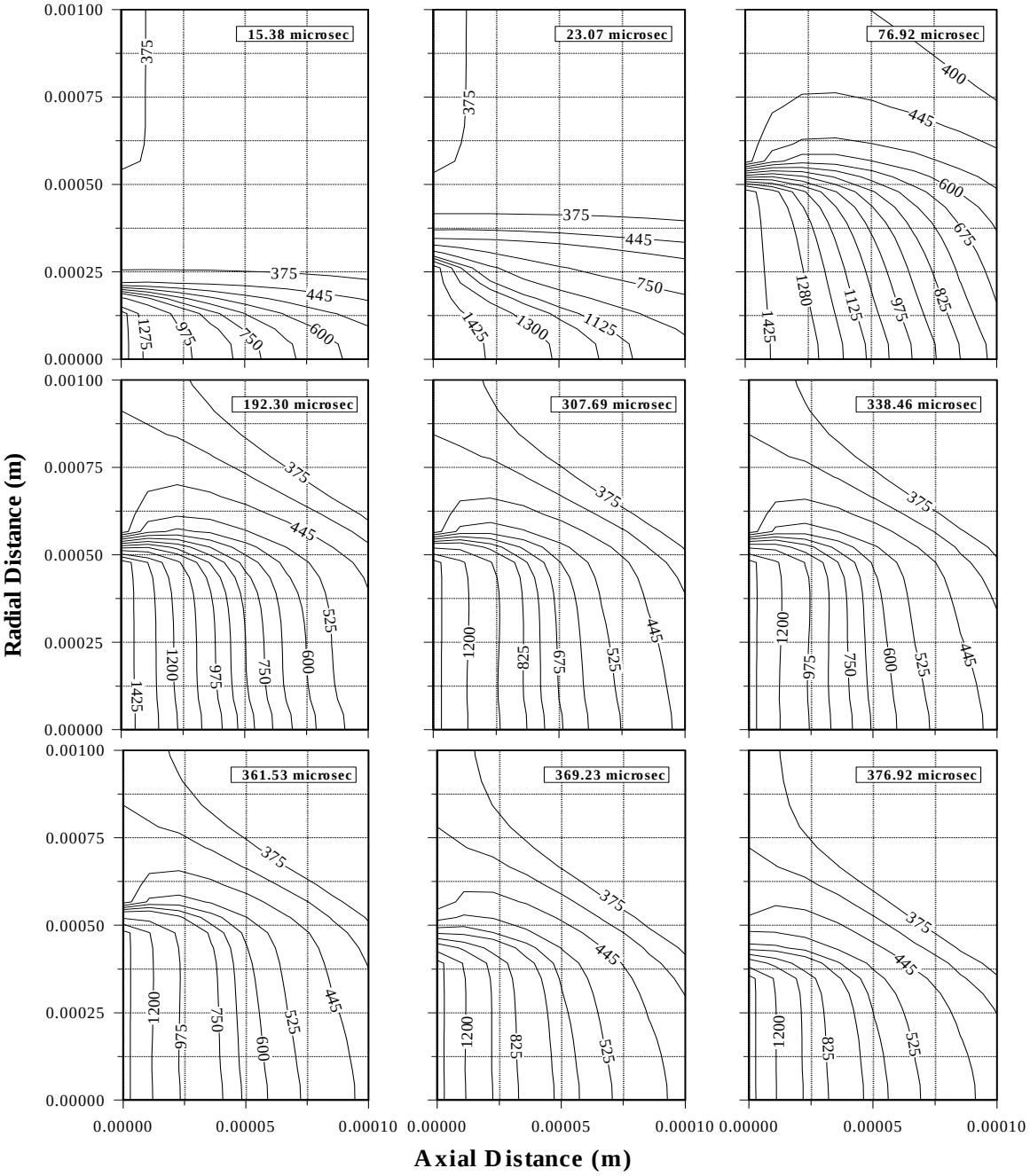

Figure 5.40: Time development of temperature (K) contours of He-air mixture for an axisymmetric transiently developing helium jet opposing the steady air jet at air jet velocity of 100 m/s.

of the steady jet, temperature field is modified considerably with progressing time. In this case, flow mixing enhances the temperature rise in the region close to the transiently developing jet.

Figure 5.41 shows velocity magnitude ratio with x/b_j along the symmetry axis for different periods. It should be noted that "b_j" represents the half velocity width of the jet and the axial distance is measured from the steady air jet inlet. Moreover, x/b_j remains constant along the symmetry axis for free jets [85]. The steady impinging jet expands gradually along the symmetry axis, since velocity magnitude ratio remains almost the same for $x/b_j \leq 5$. Due to the transiently developing jet, steady jet expansion in axial direction is suppressed. In this case, radial expansion of steady jet occurs as observed from Figure 5.36. This results in radial jet emanating from the region where steady and transiently developing jets meet. Although the transiently developing jet modifies the flow structure around the jets-meeting-region, the radial jet behaves like almost a steady jet. Consequently, x/b_j ratio remains constant with velocity magnitude ratio as consistent with the previous work [56].

Figure 5.42 shows the ratio of jet width to penetration length (D/Z_t) of the transiently developing jet. "D" represents the maximum width of the jet and the maximum jet height in axial direction is Z_t. It should be noted that the transient jet approaches the self-similar situation when D/Z_t remains almost constant with time. In the present case, transiently developing jet does not approach a self-similar situation at any time. The sharp increase in D/Z_t represents the radial expansion of the jet due to the opposing steady jet. Once the developing jet reaches a stage where

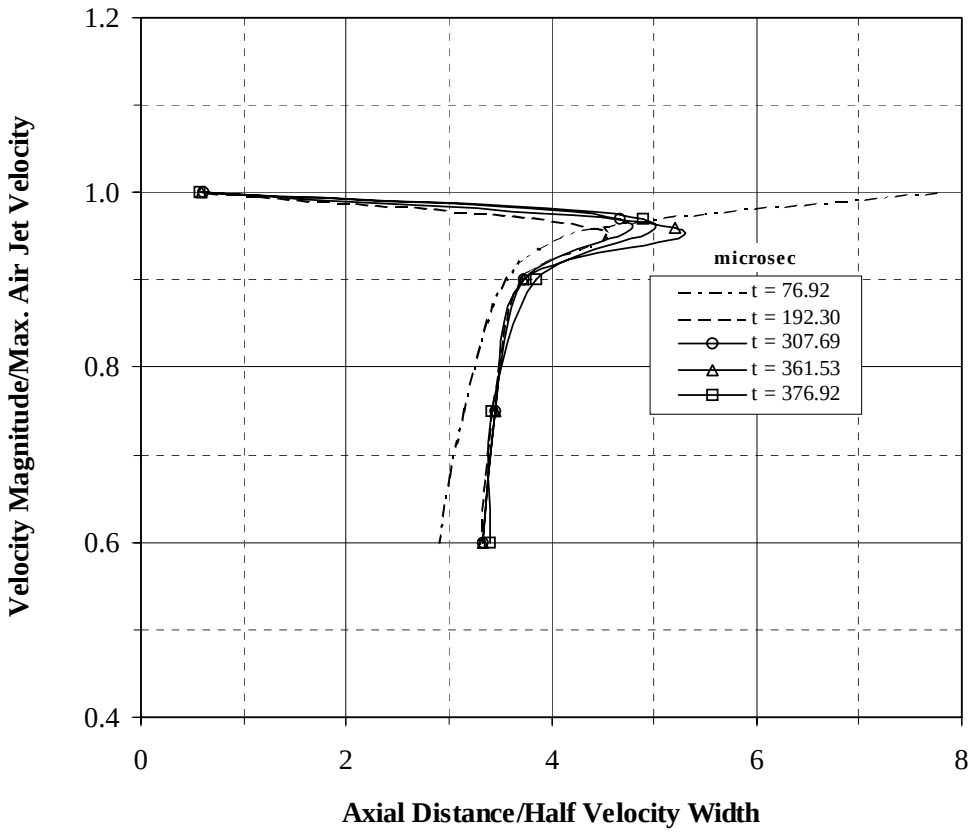

Figure 5.41: Velocity magnitude ratio with dimensionless axial distance measured from the steady air jet inlet at r = 0 m.

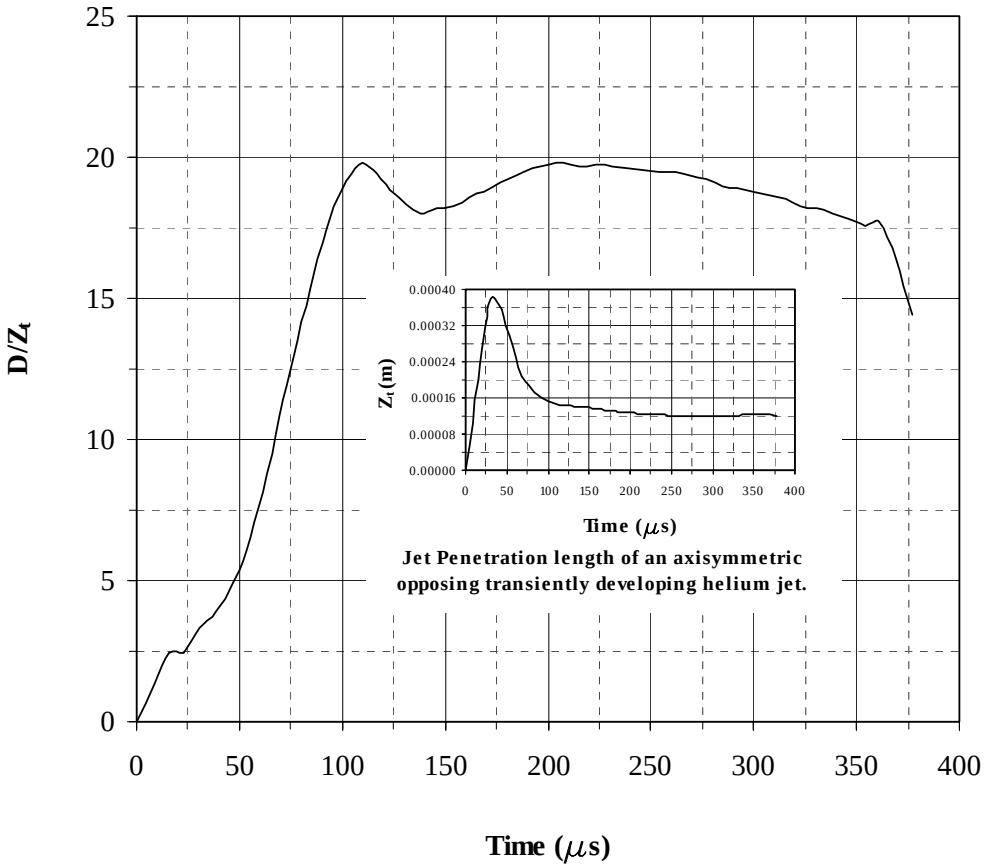

Figure 5.42: Ratio of jet width to penetration length with time for an axisymmetric transiently developing helium jet opposing the steady air jet.

the radial expansion of the jet remains almost steady; in which case, penetration of transiently developing jet in the axial direction is suppressed by the opposing steady jet. The decaying of D/Z_t with time attributes to the decaying of the transiently developing jet as can also be observed from Figure 5.5, i.e., the mean velocity of the transiently developing jet decays and its magnitude reduces gradually to zero.

Figure 5.43 shows the variation of ratio of penetration length (Z_t) to $\frac{1}{4}$ power of momentum rate per unit density $\left(\dot{M}_{He}/\overline{\rho}\right)$ with $\sqrt{t}$. The dimensionless quantity $\frac{Z_t}{\left(\dot{M}_{He}/\overline{\rho}\right)^{1/4}\times\sqrt{t}}$ represents the penetration number [29,32], where $\dot{M}_{He}$ is the total exit momentum flow rate at the transiently developing jet inlet. It should be noted that the penetration number remains constant for self-developing transient jets. In the present situation, the penetration number attains almost steady value during $10 - 15\sqrt{\mu s}$. This period corresponds to the transiently developing jet entering velocity profiles being similar (Fig. 5.5). Moreover, sharp increase in the penetration number during $\sqrt{t} \leq 5\sqrt{\mu s}$ represents the axial penetration of the jet, which is significant in the early periods as can be observed from Figure 5.36. This is also evident from Figure 5.44, in which the ratio of total momentum flow rates corresponding to transiently developing and steady jets. In this case the momentum ratio increases sharply in the early period and increases steadily during $7.5 \leq \sqrt{t} \leq 12.5\sqrt{\mu s}$. Despite the fact that the momentum flow rate increases sharply in the early period and it is inversely proportional to the penetration number, substantial increase in Z_t enables to increase the penetration number during the period $\sqrt{t} \leq 5\sqrt{\mu s}$.

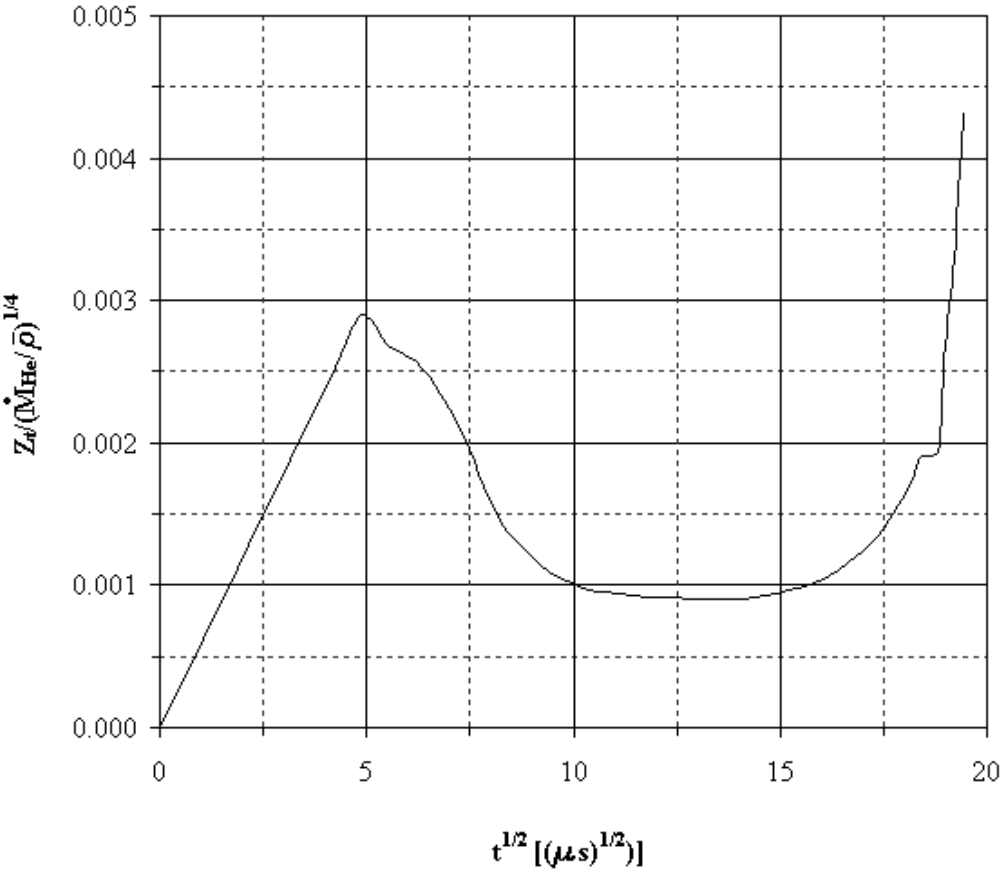

Figure 5.43: Penetration rate of an axisymmetric transiently developing helium jet opposing the steady air jet.

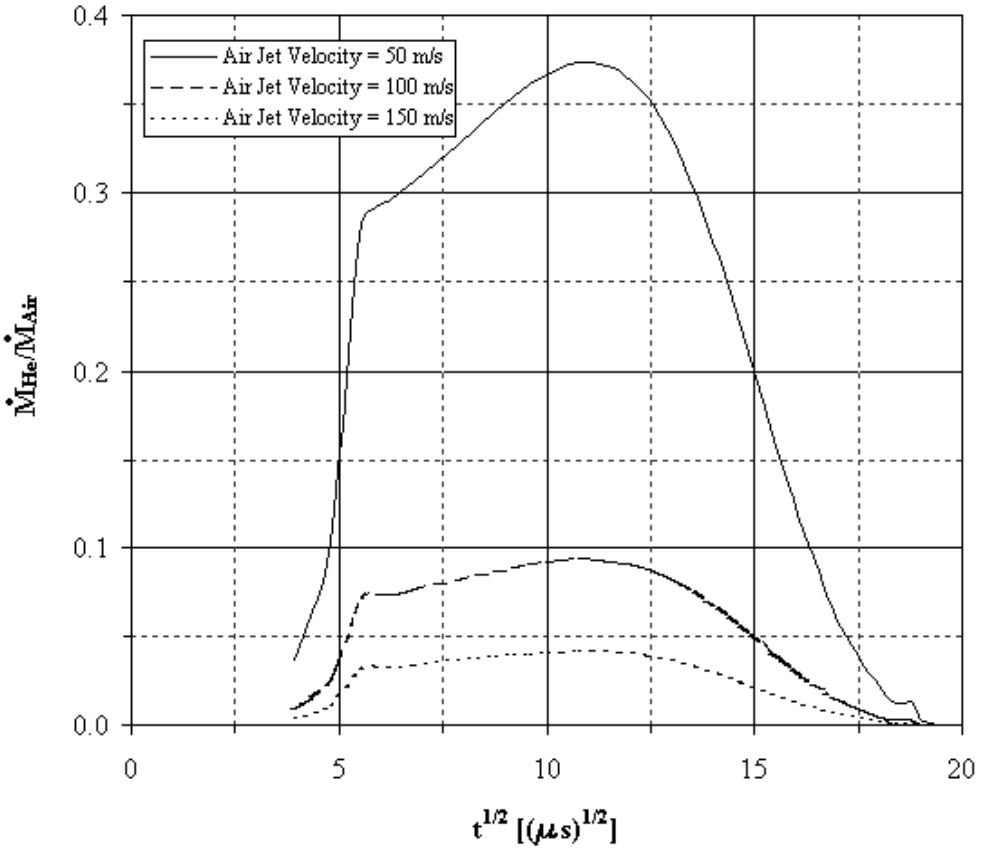

Figure 5.44: Momentum ratio at different air jet velocities versus square root of time for an axisymmetric transiently developing helium jet opposing the steady air jet.

5.3.2 Influence of Assisting Gas Velocity on The Flow Field Due to Opposing Jets

In order to examine the influence of the magnitude of steady jet mean velocity on the flow field due to transiently developing opposing jet, the mean velocity of the steady impinging jet is varied. In order to simplify the arguments, the results obtained for the flow field at time $t = 192.30\ \mu s$ are presented in the figures. It should be noted that at $t = 192.30\ \mu s$, transiently developing jet profiles at the onset of entering the control volume is almost developed in size (Fig. 5.5).

Figure 5.45 shows velocity vectors for different mean entering velocity of the steady jet at $t = 192.30\ \mu s$. In the case of low jet velocity ($5\ m/s$) transiently developing jet expands axially into the steady jet and the radial expansion of the jet is not considerable. Therefore, a weak circulation cell radially away from the transiently developing jet is developed. As the mean velocity of the steady jet increases, axial expansion of the transiently developing jet is suppressed and due to the streamline curvature effect of the steady impinging jet, radial flow next to the transiently developing jet is developed. The strength of the circulation cell increases, which in turn enhances the flow mixing next to the transiently developing jet boundary. Moreover, as the mean velocity of the steady jet increases further, the orientation of the circulation cell changes due to the enhancement of the radial flow entrainment. The strength of the circulation cell increases while the radial expansion of the transiently developing jet becomes considerable. In this case axial expansion of the transiently

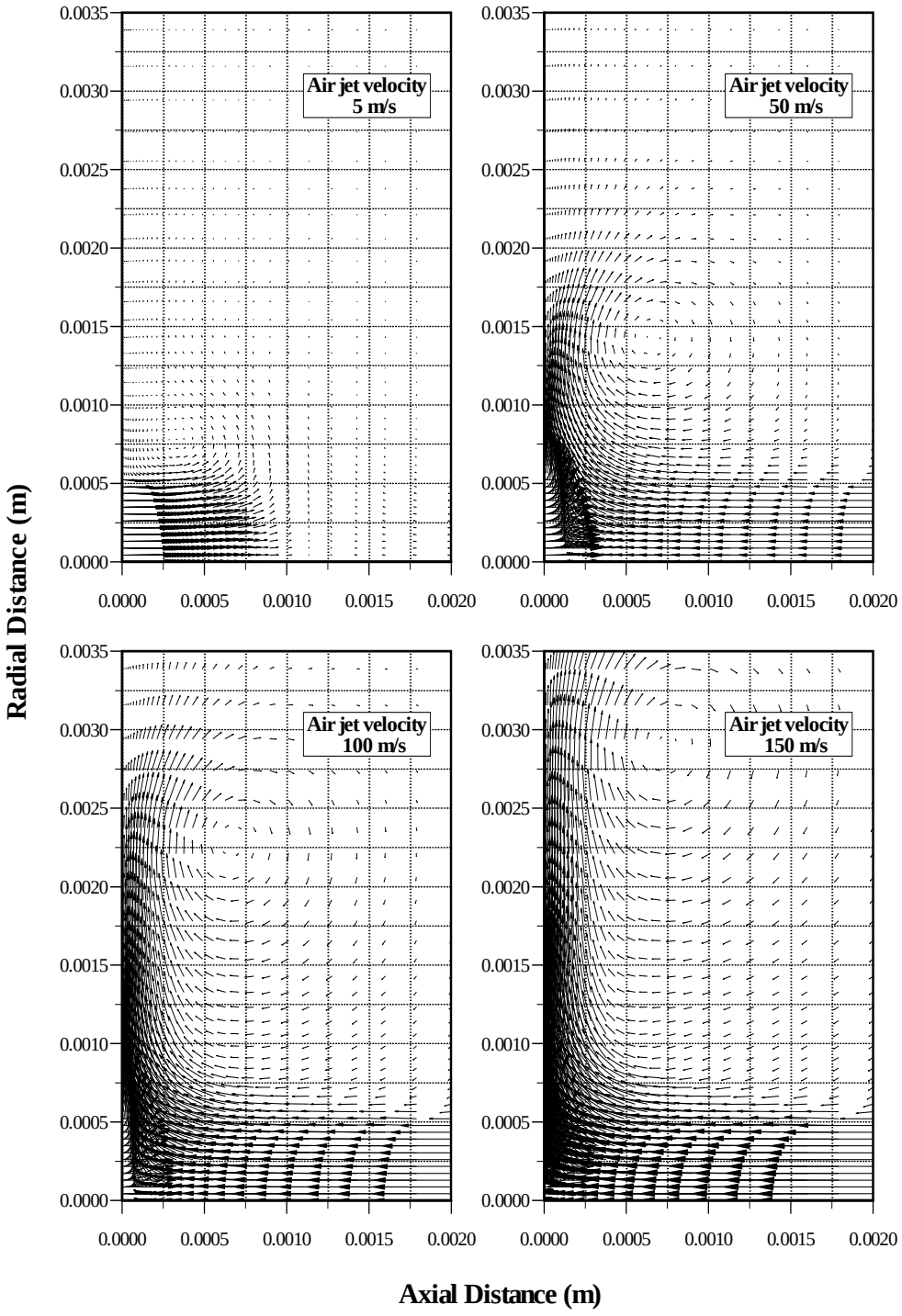

Figure 5.45: Velocity vector plots for four air jet velocities at 192.30 microseconds.

developing jet becomes minimum. This can also be seen from Figure 5.46, in which contours of velocity magnitude are shown. The flow mixing next to the transiently developing jet boundary is evident for 50 m/s mean velocity of the steady jet.

Figure 5.47 shows helium contours for different mean velocity of the steady jet at 192.30 μs. In the case of low mean velocity (5 m/s), the axial expansion of the transiently developing jet enables helium to penetrate into the steady impinging jet. Consequently, helium mass fraction attains considerably high values along the symmetry axis. It should be noted that steady impinging jet is air while transiently developing jet is helium. Moreover, existing of air in the helium jet is not observed. As the steady impinging jet velocity increases (50 m/s), helium penetration into air along the axial direction is suppressed and mixing of the air with helium next to the transiently developing jet boundary reduces the helium mass fraction in this region. As the steady impinging jet velocity increases further, helium penetration into air is suppressed considerably. The streamline curvature of the steady impinging jet enhances the mixing of helium with air in both axial and radial directions.

Figure 5.48 shows temperature contours for different entering mean velocity of steady jet at $t = 192.30$ μs. It should be noted that the helium jet is at 1500 K while the steady impinging jet is at 300 K. Consequently, as transiently developing jet expands into the steady jet, temperature of air increases in the region close to the transiently developing jet boundary. This situation is clearly observed for 5 m/s steady jet velocity. In this case, convection and conduction heating of the air take place. When the mean velocity of the steady jet increases, flow mixing modifies the

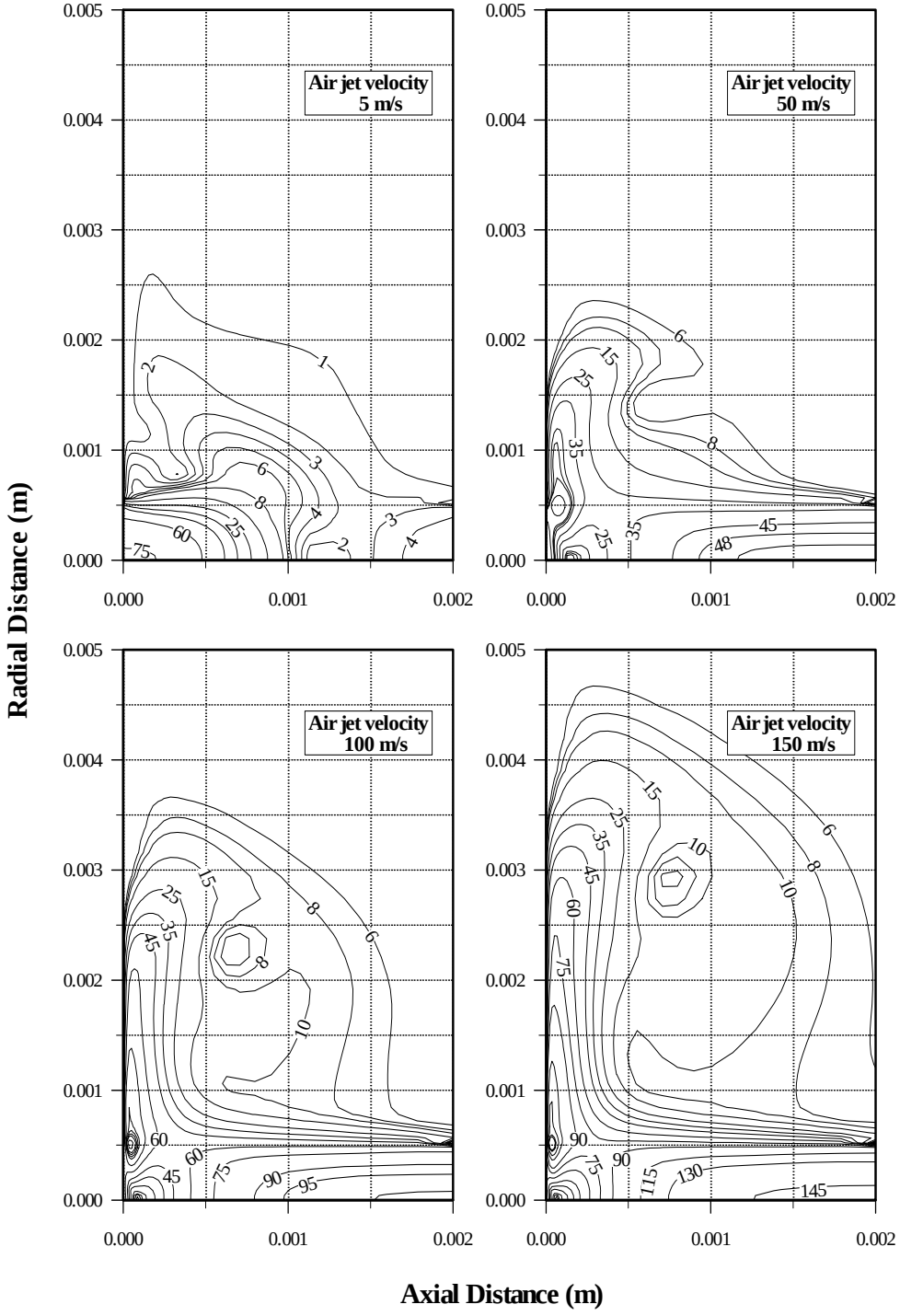

Figure 5.46: Velocity magnitude (m/s) contours for four air jet velocities at 192.30 microseconds.

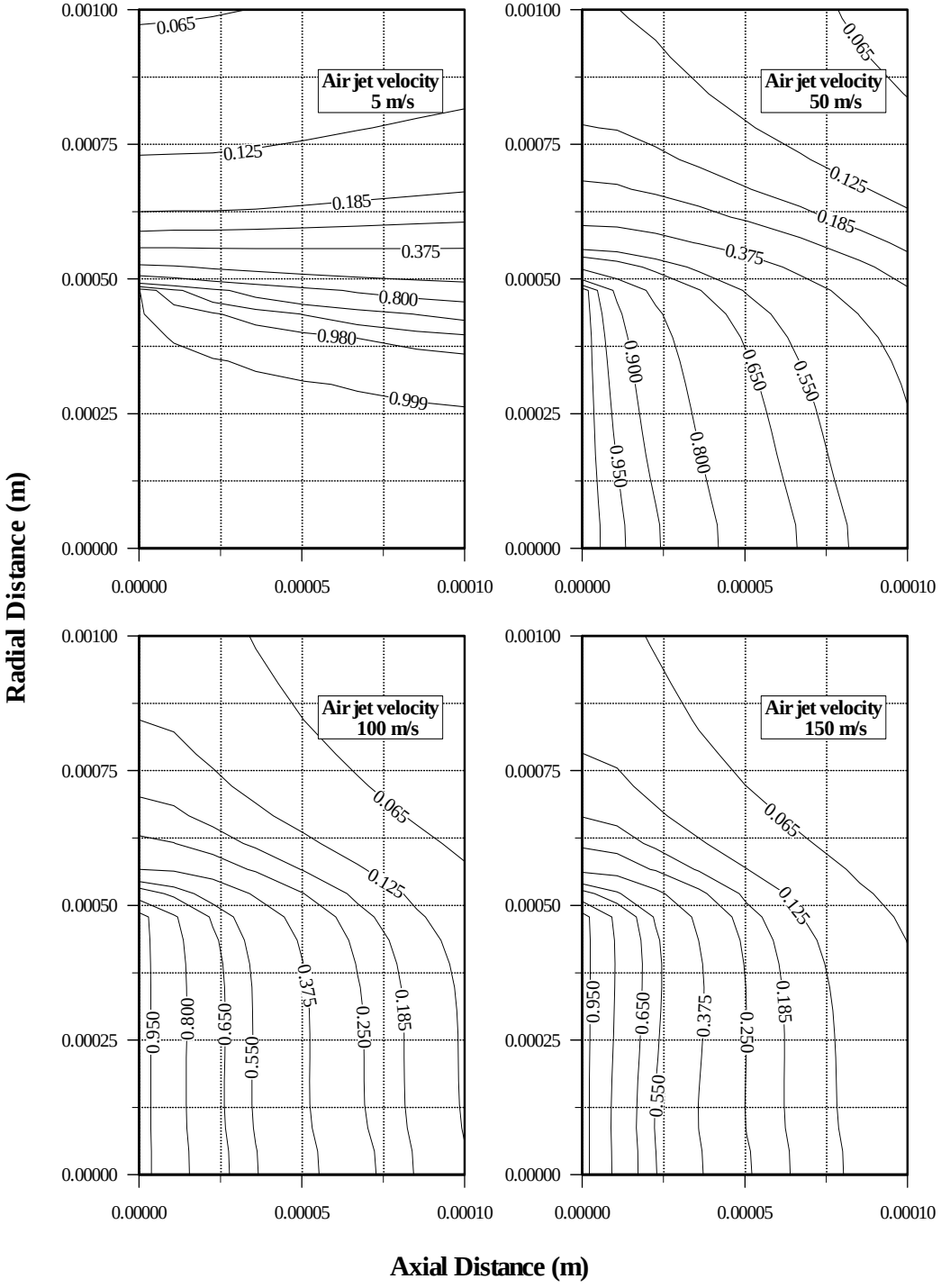

Figure 5.47: Mass fraction contours of helium for four air jet velocities at 192.30 microseconds.

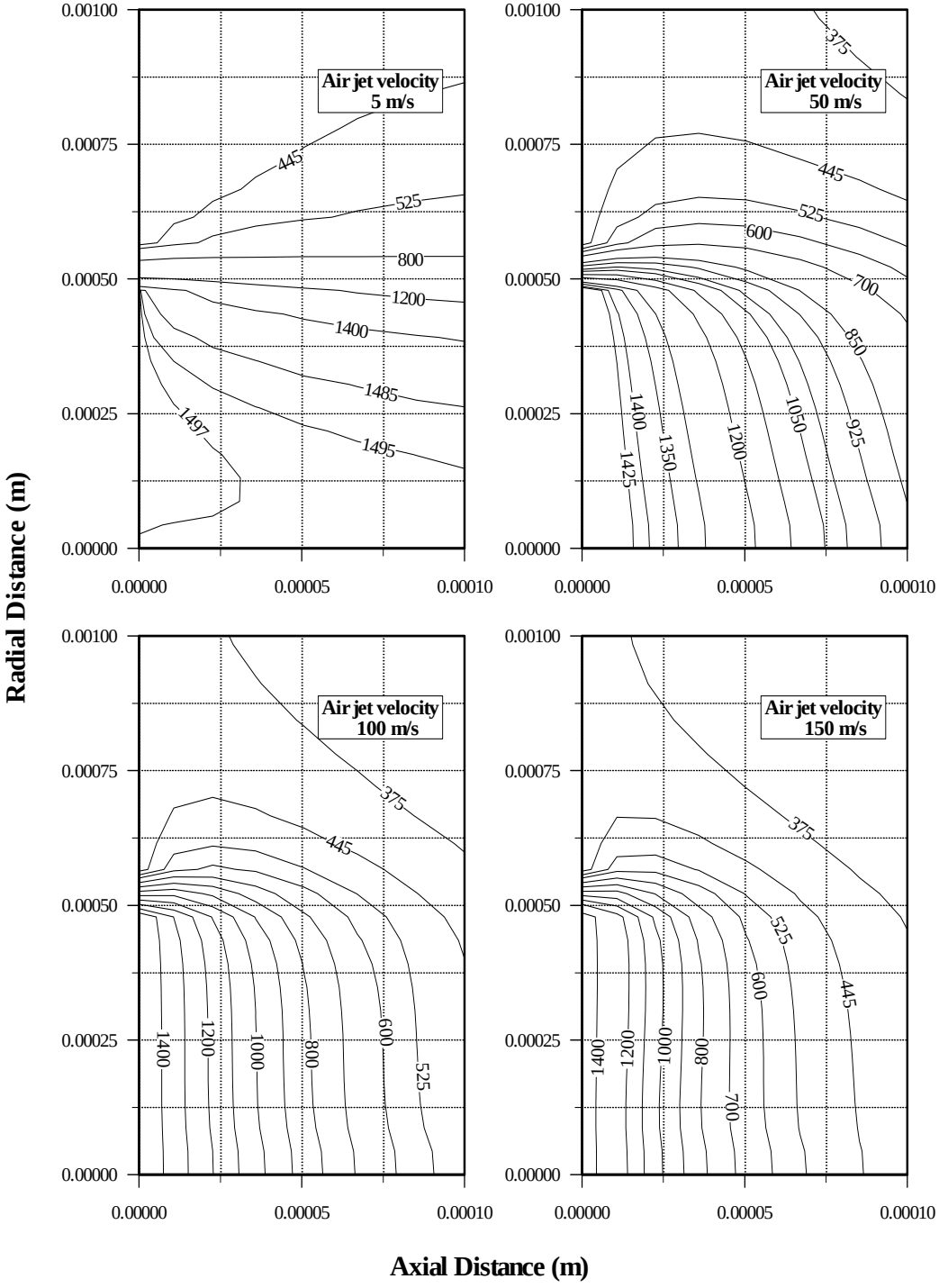

Figure 5.48: Temperature (K) contours for four air jet velocities at 192.30 microseconds.

temperature field in the region close to the transiently developing jet. Moreover, the circulation cell is not able to develop temperature contours that follow the velocity contours in the circulation cell. However, radial extension of temperature contours are observed for mean velocity of steady jet $\geq 100\ m/s$, i.e., the influence of streamline curvature effect of the steady impinging jet on the convective heat transfer becomes significant.

Figure 5.49 shows pressure contours for different entering mean velocity of the steady impinging jet at 192.30 μs. The variation in size and orientation of the circulation cell next to the jet boundary is evident with increasing mean velocity of the steady jet. Moreover, stagnation region where both jets meet moves towards the transiently developing jet when steady jet velocity increases. The radial expansion of the transiently developing jets results in high-pressure region extending in the radial direction.

Figure 5.50 shows the turbulence kinetic energy for different entering mean velocity of the steady jet at different periods. The maximum turbulence kinetic energy attains high values as mean steady jet velocity increases. Moreover, the maximum turbulence kinetic energy is generated in the region next to the stagnation zone; which is also confirmed in the previous study [10]. The location of the maximum turbulence kinetic energy moves towards the transiently developing jet as mean velocity of the steady jet increases. This is because of the stagnation region which moves towards the transiently developing jet. This can also be seen from Figure 5.51, in which axial velocity along the axial direction is shown, i.e., the location of zero axial velocity

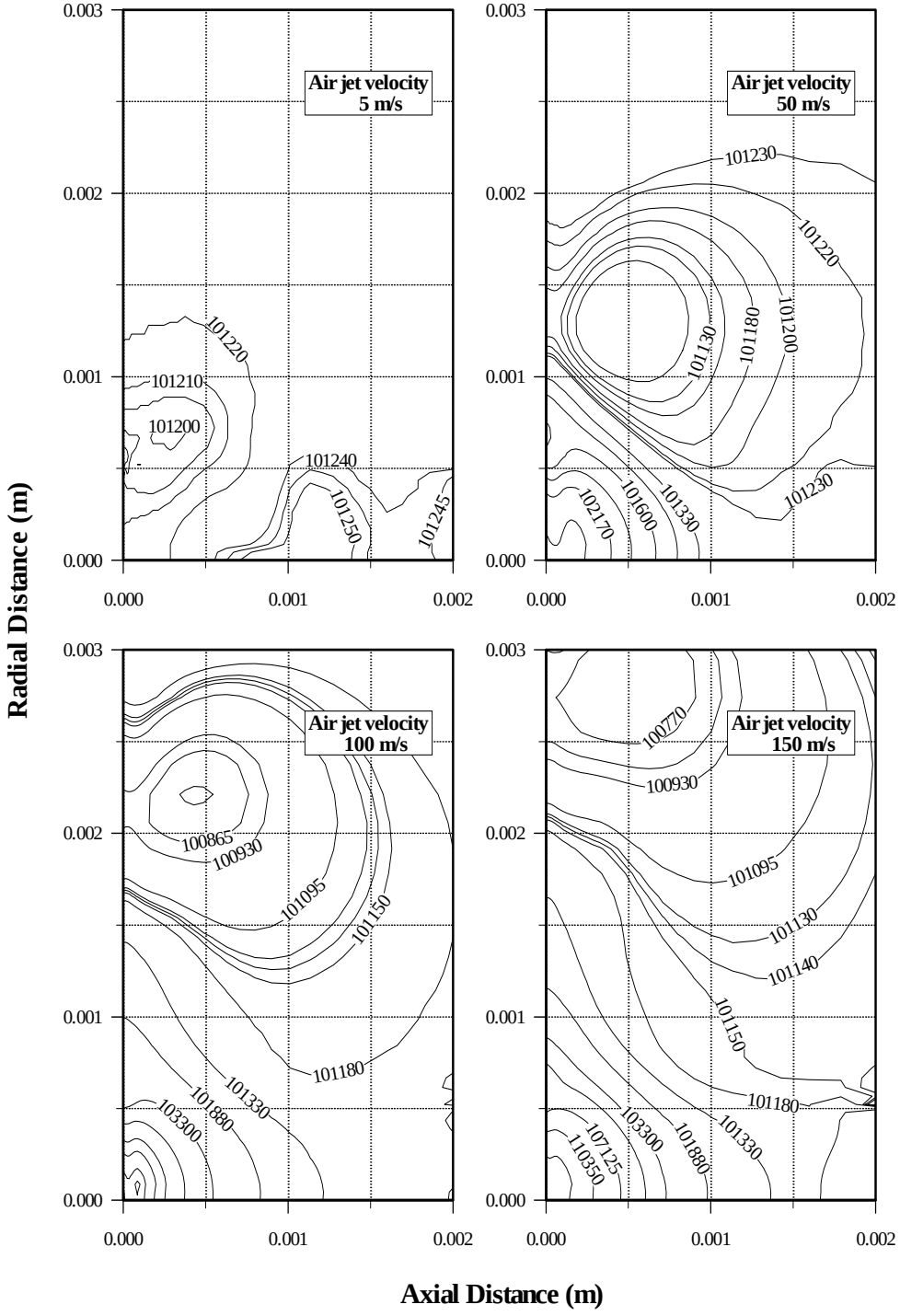

Figure 5.49: Pressure (Pa) contours for four air jet velocities at 192.30 microseconds.

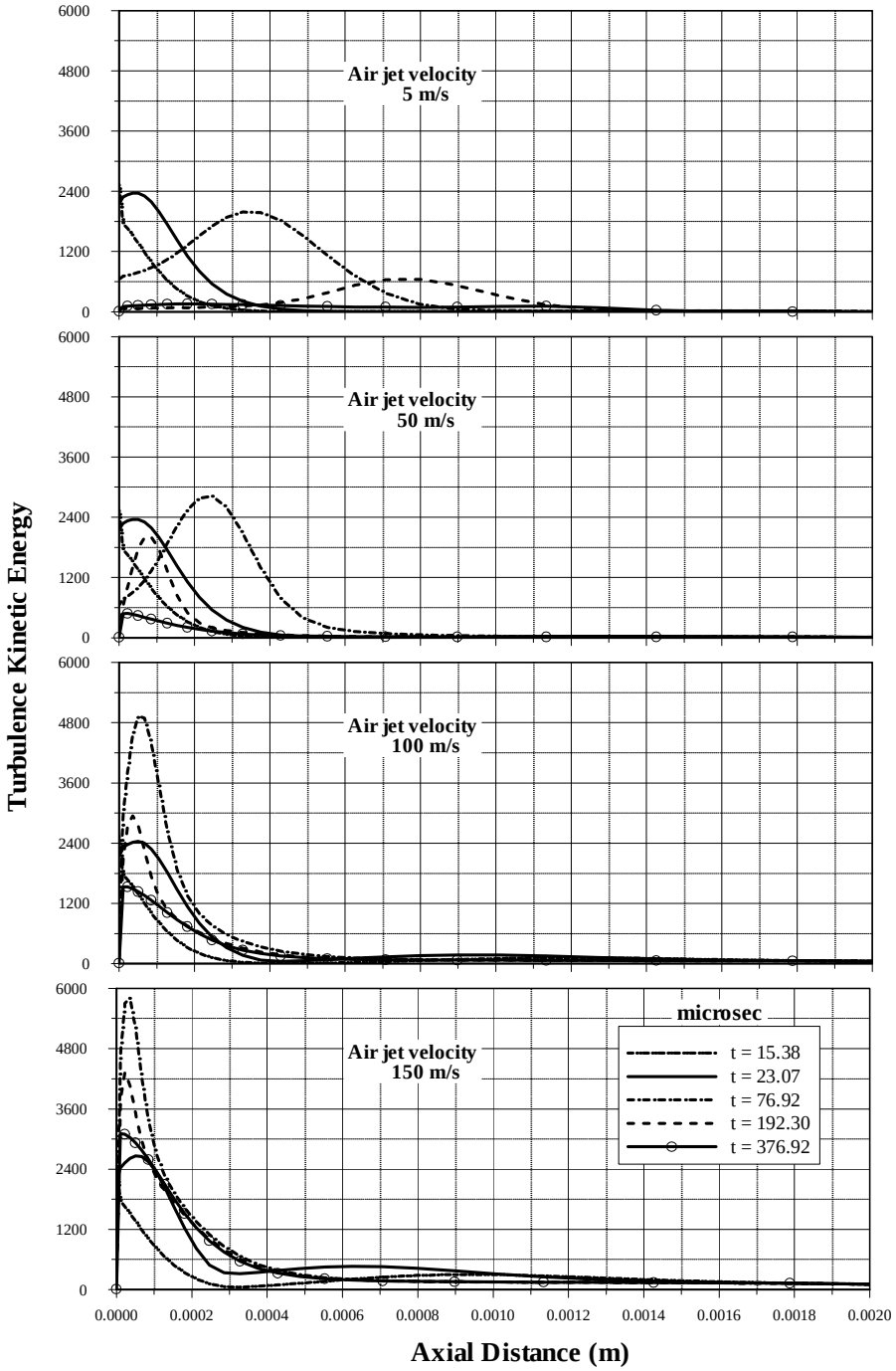

Figure 5.50: Temporal variation of turbulence kinetic energy of He-air mixture for four air jet velocites along the jet symmetry axis at r = 0 m.

moves towards the transiently developing jet as the mean velocity of the steady jet increases. The influence of streamline curvature on the turbulence kinetic energy generation becomes evident when mean velocity of the steady jet exceeds 100 m/s. In this case, turbulence kinetic energy generation becomes similar to that observed for stagnation point flow [10]. Depending on the transiently developing jet profiles, the magnitude of turbulence kinetic energy varies, i.e., the velocity profile resulting in high streamline curvature effect gives rise to highest turbulence kinetic energy generation, which occurs at 76.92 μs.

Figure 5.52 shows mass fraction of helium, nitrogen, and oxygen along the symmetry axis for different exiting mean velocity of the steady jet at 192.30 μs while Figure 5.53 shows mass fraction of helium, nitrogen, and oxygen along the symmetry axis for different times and 100 m/s mean velocity of the steady jet. Helium mass fraction reduces gradually along the symmetry axis for low mean velocity of steady jet. Moreover, increasing steady jet velocity results in sharp decay in helium mass fraction. In the case of oxygen and nitrogen, sharp decay of mass fraction is observed close to the transiently developing jet region. It should be noted that mass fraction ratio of O_2/N_2 is 0.29 in the steady air jet. However, in the region close to the transient jet, this ratio changes and oxygen mass fraction increases. This indicates that the diffusional transport of oxygen in the region close to the stagnation zone is higher than that corresponds to nitrogen. This is more pronounced for high steady jet mean velocities. Consequently, flow mixing and diffusional mass transport in the region close to the stagnation zone modify the mass fraction of oxygen and nitrogen.

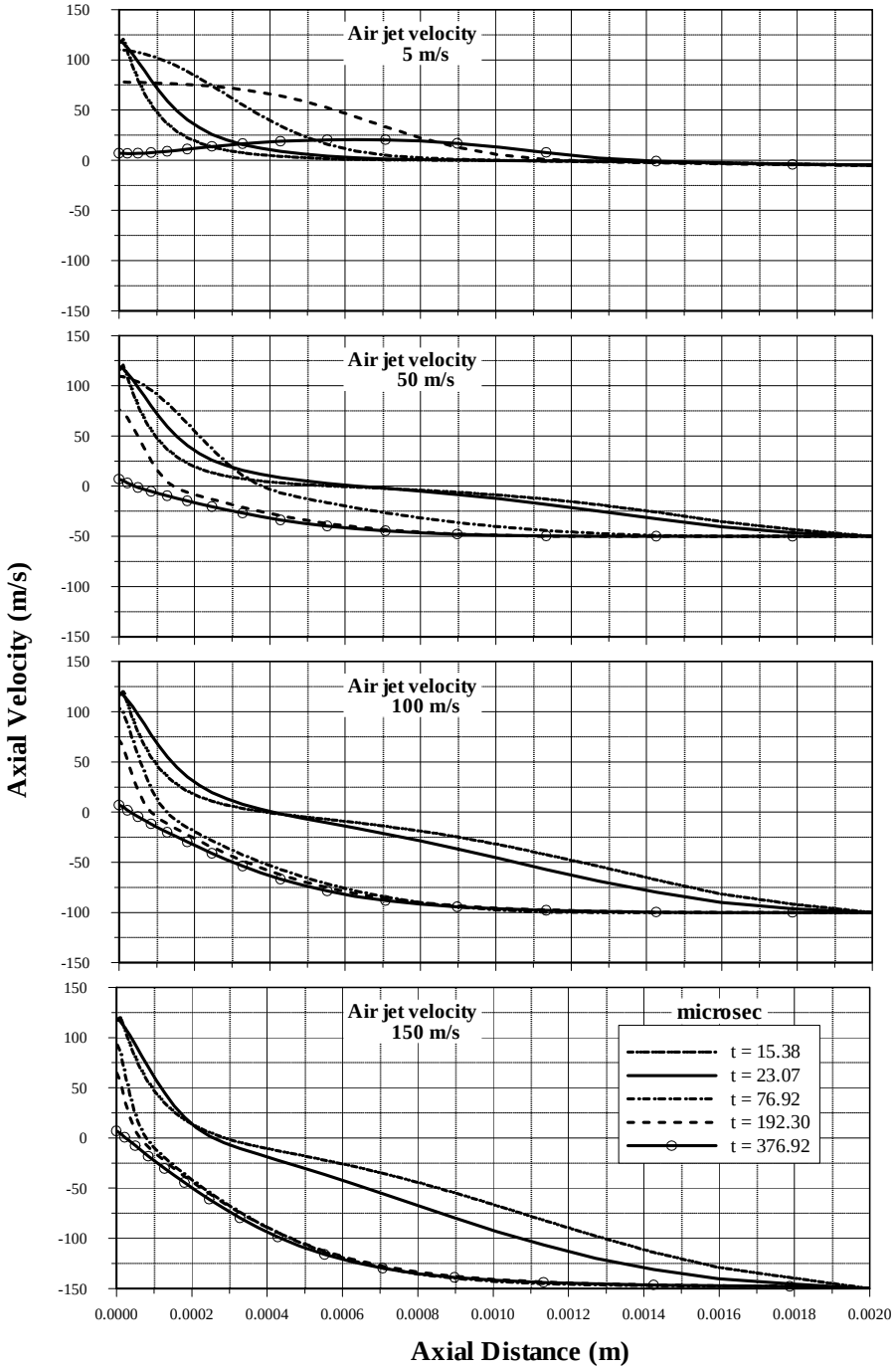

Figure 5.51: Temporal variation of axial velocity of He-air mixture for four air jet velocites along the jet symmetry axis at r = 0 m.

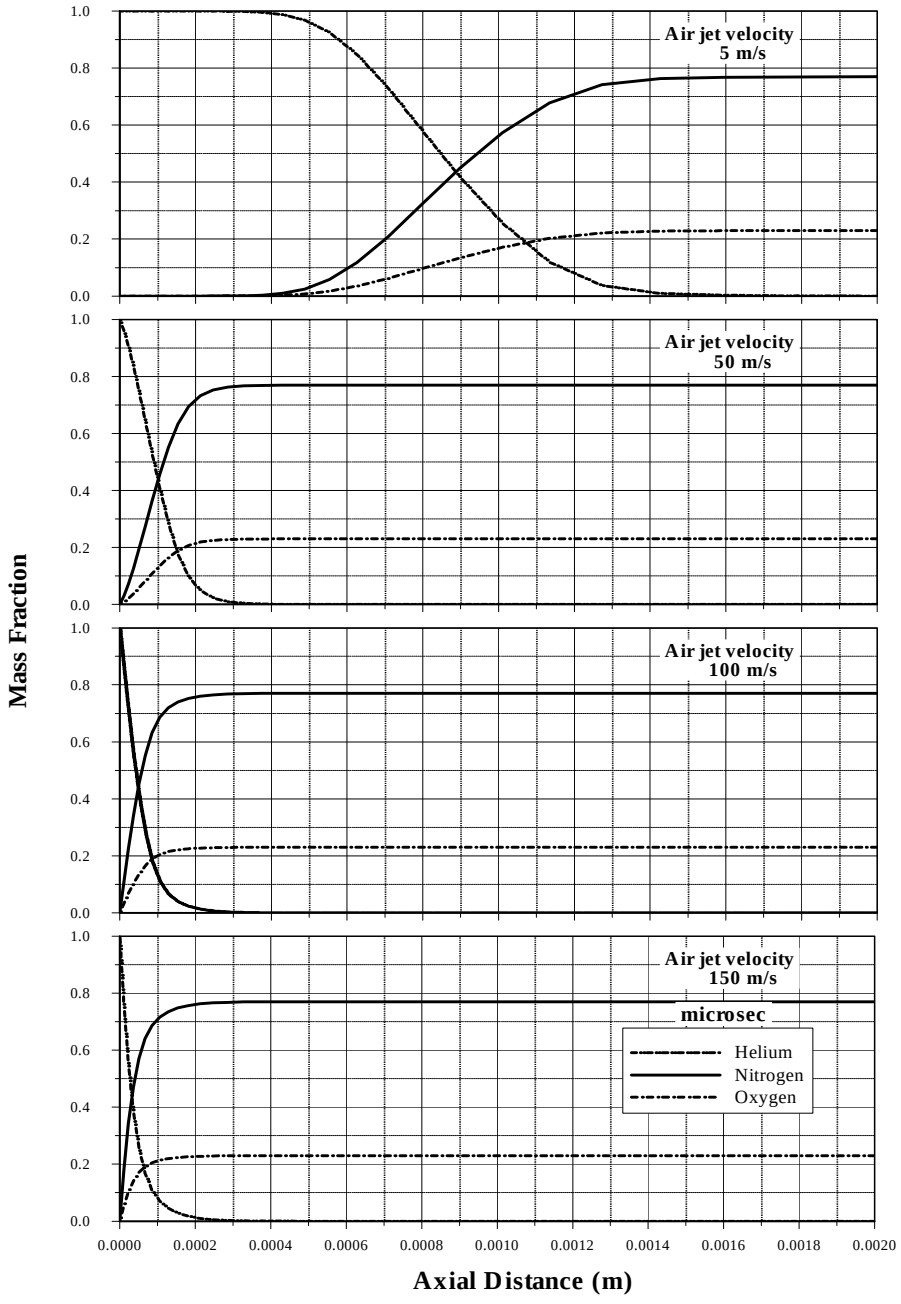

Figure 5.52: Variation of mass fraction of helium, nitrogen and oxygen in He-air mixture for four air jet velocites along the jet symmetry axis at r = 0 m and t = 192.30 microseconds.

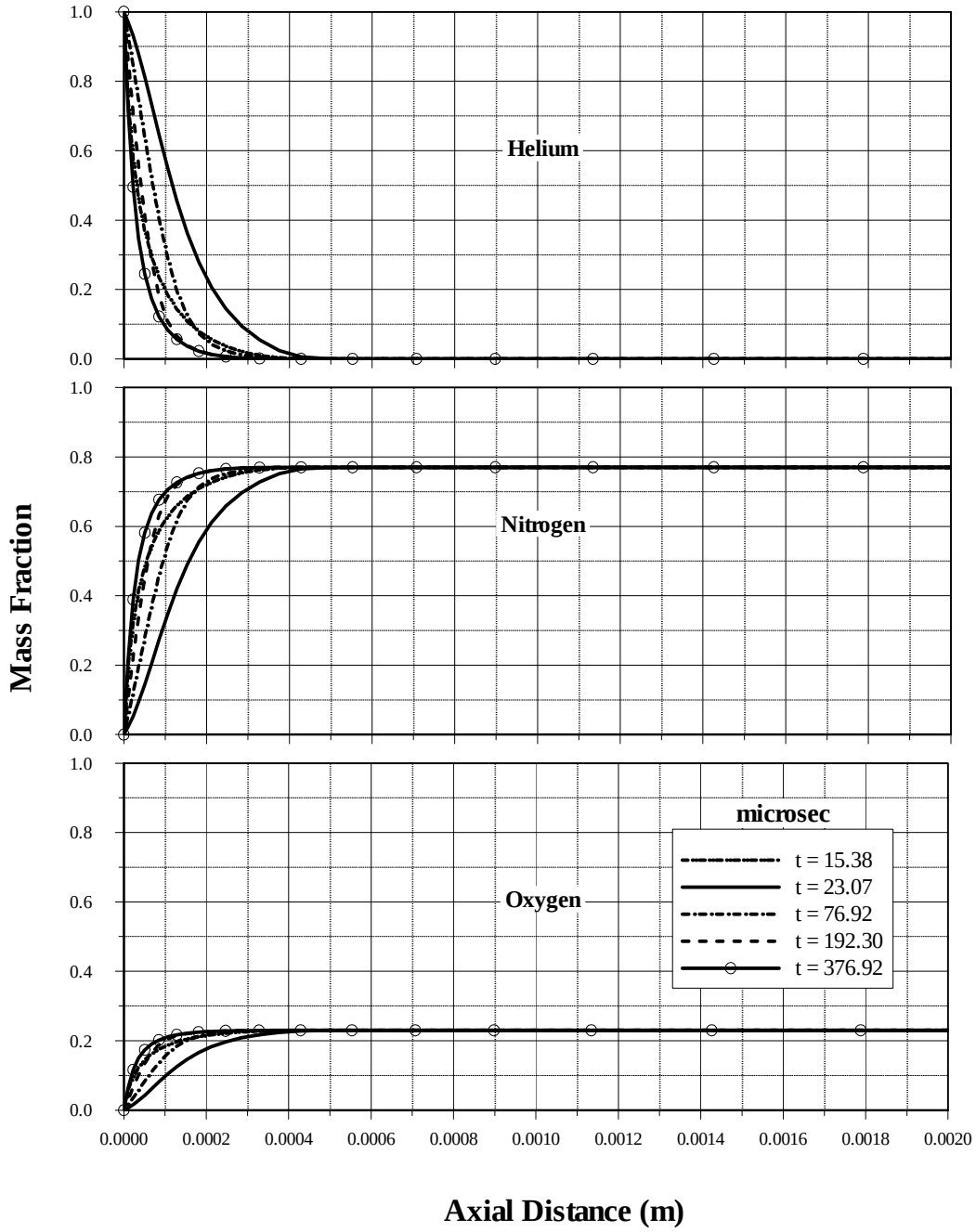

Figure 5.53: Temporal variation of mass fraction of helium, nitrogen and oxygen in He-air mixture along the jet symmetry axis at r = 0 m and at air jet velocity of 100 m/s.

Table 5.1: Thermophysical properties of fluids used in the simulations.

$Properties$	Air	$Helium\ (He)$	$He - Air\ mixture$
$k\ (W/m-k)$	0.0242	0.152	0.0454
$c_p\ (KJ/Kg-K)$	1.006	5.193	1.000
$\rho\ (Kg/m^3)$	1.225	0.1625	–
$\mu\ (Kg/m-s)$	1.7894×10^{-5}	1.99×10^{-5}	1.72×10^{-5}
$M\ (Kg/Kgmol)$	28.966	4.0026	28.966
$D_{AB}\ (m^2/s)$	–	–	2.88×10^{-5}

Chapter 6

CONCLUSIONS

6.1 Transient Jet Expansion into Stagnant Air

Transiently developing jet emanating from a free surface and expanding into air ambient is considered to resemble the vapor jet behavior ejected from the laser-produced cavity. Since the thermophysical properties of laser produced vapor is not known, air or helium at 1500 K is considered as emerging jet in the simulations. The jet exiting velocity profiles (jet velocity profiles onset of exiting the cavity) employed are obtained from the previous experimental study. This enables us to simulate the actual laser produced cavity exiting conditions. A numerical scheme employing control volume approach is employed when simulating the flow situations. The low Reynolds number $k - \varepsilon$ turbulence model is employed to account for the turbulence.

6.1.1 Transient Air Jet into Stagnant Air

It is found that in the early period the transient air jet expands more radially than it does axially. As the time progresses, the jet width to jet penetration depth ratio reduces. Once the jet exit velocity profiles become almost similar, self-similar transient jet behavior is resulted. The specific conclusions derived from the present

study can be listed as follows:

1) Changes in jet exit velocity profiles result in variation in velocity magnitude along the symmetry axis. This, in turn, alters the turbulence kinetic energy generation in this region. Moreover, very small change in velocity magnitude results in large change in turbulence kinetic energy.

2) In the early period temperature profiles follow the velocity profiles and the convective heat transfer from the jet surface to its ambient is small. This occurs because of small area of jet surface and short period of time, i.e., jet does not expand enough to generate a large surface area and the period of expansion is short and hence the heat transfer rate is low during early periods.

3) In the early period the ratio of jet expansion in the axial direction to the one-fourth power of jet momentum rate per unit density increases linearly with the square root of time, i.e., penetration number increases steadily. In this case, jet behaves similar to those observed for slow flow jets. As time progresses, the rate of momentum dissipation due to viscous dissipation becomes high and the penetration number increases rapidly. This is observed for $\sqrt{t} \geq 12\sqrt{\mu s}$ in the present case.

6.1.2 Transient Helium Jet into Stagnant Air

It is found that the transient helium jet approaches self-similar behavior as the dimensionless jet width (D/Z_t) becomes 0.65 and the transition length of the jet is obtained to be about 3 jet inlet diameters, which is less than the data reported in the previous study. The specific conclusions derived from the present study are listed as

follows:

1) The flow entrainment results in a circulation cell in the region next to the jet outer boundary after $t = 76.92\ \mu s$. The orientation of circulation cell changes with progressing time. This is due to the jet inlet velocity profiles, which varies with time.

2) Temperature contours follow almost the velocity profiles. Moreover, flow entrainment enhances the convective heat transfer rate, which in turn extends the high temperature field into the jet-entrained region.

3) The mass ratio of helium decays sharply as the distance along the symmetry axis increases away from the jet exit. The mixing of helium with air along the symmetry axis indicates that while helium jet expands into the stagnant air, some air molecules remain in the region close to the jet inlet as well as the expansion of the helium into air accelerates the diffusional transport of air into helium jet.

4) In the early period of helium jet expansion, self-similar behavior of the jet is not observed. This is because of the vast change of jet inlet velocity profiles in the early period.

5) The constant penetration number $\left(\frac{Z_t}{\left(\dot{M}_{He}/\overline{\rho} \right)^{1/4} \times \sqrt{t}} \right)$ is almost impossible during the jet expansion in the present situation, since the jet inlet velocity changes drastically in the early period.

6.2 Opposing Jets

The flow field due to opposing jet and transiently developing jet is studied in relation to laser-induced ablation process. Steady jet represents the assisting gas

while transiently developing jet resembles the vapor plume emanating from the solid surface during the ablation process. Since the thermophysical properties of the vapor plume are not known, helium at 1500 K is employed for the transiently developing jet while air is considered as an assisting gas. The flow, temperature and mass fraction fields are simulated numerically using a control volume approach. The low Reynolds number $k-\varepsilon$ turbulence model is employed to account for the turbulence.

6.2.1 Transient Effect on The Flow Field Due to Opposing Jets

It is found that the flow field in the region close to the transiently developing jet is influenced considerably by the assisting gas jet. In the early stage transiently developing jet expands in the axial direction and as the time progresses radial expansion of the jet dominates; in which case, a circulation cell next to the steady jet boundary is developed. The specific conclusions derived from the present study can be listed as follows:

1) The orientation and the size of the circulation cell next to the steady jet boundary are influenced by the transiently developing jet entering velocities. In this case, the velocity profile (similar to the profile for the fully developed flow) enhances the size of the circulation cell.

2) The transiently developing jet influences the streamline curvature of the steady impinging jet. In this case, enhancing radial flow suppresses the transiently developing

jet expansion in the axial direction.

3) The deep penetration of oxygen/nitrogen mass fraction into the region next to the helium jet entry indicates that the flow mixing in this region occurs, i.e., next to the stagnation region where two jets meet, the flow mixing is enhanced which can also be observed through temperature contours. This is more pronounced as time progresses.

4) A radial jet developed due to opposing of transiently developing and steady jets. In this case, the radial jet show similar behavior to that corresponding to the free jet, and the transiently developing jet characteristics do not affect considerably the radial free jet characteristics.

5) The transiently developing jet does not approach a self-similar condition at any period considered. Consequently, developing jet shows transient characteristics for all the durations considered in the present study.

6) The penetration number of transiently developing jet attains almost steady values during $10 - 15\sqrt{\mu s}$ period. Moreover, sharp increase in penetration number in the early period corresponds to the axial penetration of the jet.

6.2.2 Influence of Assisting Gas Velocity on The Flow Field Due to Opposing Jets

It is found that the influence of the magnitude of the mean velocity of the steady jet on the flow field in the region close to the transiently developing jet is found to be

very significant. In this case increasing mean velocity of impinging steady jet results in development of the circulation cell next to steady jet boundary. The orientation and strength of the circulation are modified by the mean velocity of the steady jet. In this case, streamline curvature effect and flow entrainment cause flow mixing next to the transiently developing jet boundary. Moreover, increasing mean velocity of the steady jet suppresses the axial expansion of the transiently developing jet; hence, the radial expansion of the jet is enhanced.

Mass fraction of helium decreases sharply in the axial direction as mean velocity of the steady jet increases. Although the mass fraction ratio of O_2/N_2 in steady air jet is 0.29 at jet inlet to the solution domain, it is modified in the region close to the stagnation zone. In this case, oxygen mass fraction enhances in this region. This suggests that flow mixing next to the transiently developing jet and diffusional mass transport modify the mass fraction of species considerably in this region.

6.3 Future Work and Recommendations

Since laser-machining applications are involved with the laser non-conduction limited heating situation, phase change in the solid substrate should be considered when modeling the laser-workpiece interaction. Moreover, the material properties vary with temperature; therefore, temperature dependent properties should be accommodated in the analysis. The rate of evaporation from the surface and the magnitude of recoil pressure in the cavity determine the evaporating front velocity. Consequently, evaporating front velocity of the vapor jet emanating from the cavity needs to be considered

when simulating the impinging gas effects on the laser-workpiece interaction.

Although the thermophysical properties of the evaporating front are not known, a high-density gas, such as steam, can be introduced in the simulations to resemble the evaporating front. The nucleation formation in the superheated liquid in the cavity and droplet formation in the vapor phase during the plume expansion could be accommodated in the heating model. Moreover, the influence of retarding zone on the vapor front expansion could be included in the analysis.

Bibliography

[1] I. Sezai, and A.A. Mohamad, Three-Dimensional Simulation of Laminar Rectangular Impinging Jets, Flow Structure, and Heat Transfer, *ASME Journal of Heat Transfer*, Vol. 121, pp. 50-56, 1999.

[2] P.Y. Tzeng, C.Y. Soong, and C.D. Hsieh, Numerical Investigation of Heat Transfer under Confined Impinging Turbulent Slot Jets, *Numerical Heat Transfer,* Part A*,* Vol. 35, pp. 903-924, 1999.

[3] S.H. Seyedein, M. Hasan, and A.S. Mujumdar, Turbulent Flow and Heat Transfer from Confined Multiple Impinging Slot Jets, *Numerical Heat Transfer,* Part A, Vol. 27, pp. 35-51, 1995.

[4] Y. Tzu, and C.H. Shyu, Numerical Study of Multiple Impinging Slot Jets with an Inclined Confinement Surface, *Numerical Heat Transfer,* Part A, Vol. 33, pp. 23-37, 1998.

[5] H. Fujimoto, H. Takuda, N. Hatta, and R. Viskanta, Numerical Simulation of Transient Cooling of a Hot Solid by an Impinging Free Surface Jet, *Numerical Heat Transfer,* Part A, Vol. 36, pp. 767-780, 1999.

[6] M.M. Rahman, A. J. Bula, and J.E. Leland, Conjugate Heat Transfer During Free Jet Impingement of a High Prandtl Number Fluid, *Numerical Heat Transfer,* Part B, Vol. 36, pp. 139-162, 1999.

[7] S.Z. Shuja, B.S. Yilbas, and M.O. Budair, Gas Jet Impingement on a Surface Having a Limited Constant Heat Flux Area: Various Turbulence Models, *Numerical Heat Transfer*, Part A, Vol. 36, pp. 171-200, 1999.

[8] S.Z. Shuja, B.S. Yilbas, and M.O. Budair, Modeling of Laser Heating of Solid Substance Including Assisting Gas Impingement, *Numerical Heat Transfer,* Part A, Vol. 33, pp. 315-339, 1998.

[9] T.J. Craft, L.J. W. Graham, and B.E. Launder, Impinging Jet Studies For Turbulence Model Assessment-II. An Examination of the Performance of Four Turbulence Models, *International Journal of Heat and Mass Transfer*, Vol. 36, No. 10, pp. 2685-2697, 1993.

[10] D. Cooper, D.C. Jackson, B.E. Launder, and G.X. Liao, Impinging Jet Studies For Turbulence Model Assessment-I. Flow-Field Experiments, *International Journal of Heat and Mass Transfer*, Vol. 36, No. 10, pp. 2675-2684, 1993.

[11] S. Parneix, M. Behnia, and P.A. Durbin, Predictions of Turbulent Heat Transfer in an Axisymmetric Jet Impinging on a Heated Pedestal, *ASME Journal of Heat Transfer*, Vol. 121, pp. 43-49, 1999.

[12] J.A. Fitzgerald, and S.V. Garimella, A Study of the Flow Field of a Confined and Submerged Impinging Jet, *International Journal of Heat and Mass Transfer*, Vol. 41, No. 8-9, pp. 1025-1034, 1998.

[13] J.A. Fitzgerald, and S.V. Garimella, Flow Field Effects on Heat Transfer in Confined Jet Impingement, *ASME Journal of Heat Transfer*, Vol. 119, pp. 630-632, 1997.

[14] J. Sakakibara, K. Hishida, and M. Maeda, Vortex Structure and Heat Transfer in the Stagnation Region of an Impinging Plane Jet (Simultaneous Measurements of Velocity and Temperature Fields by Digital Particle Image Velocimetry and Laser-Induced Fluorescence), *International Journal of Heat and Mass Transfer*, Vol. 40, No. 13, pp. 3163-3176, 1997.

[15] Y.S. Chung, D.H. Lee, and J.S. Lee, Heat Transfer Characteristics of an Axisymmetric Jet Impinging on the Rib-Roughened Convex Surface, *International Journal of Heat and Mass Transfer*, Vol. 42, pp. 2101–2110, 1999.

[16] H. Schlichting, *Boundary Layer Theory*, Seventh Edition, McGraw-Hill, New York.

[17] D.S. Lee, K.D. Kihm, and S.H. Chung, Analytical solutions for the developing jet from a fully- developed laminar tube flow, *ASME Journal of Fluid Engineering*, 119, pp.716-718, 1997.

[18] R.V. Wilson and A.O. Demuren, Numerical Simulation of Turbulent Jets with Rectangular Cross-Section, *ASME Journal of Fluid Engineering*, Vol. 120, pp. 285-290, 1998.

[19] M.-H. Chen, and Z.-C. Hong, A pdf Description of Turbulent Axisymmetric Free Jet Flow, *ASME Journal of Fluid Engineering*, Vol. 121, pp. 73-79, 1999.

[20] J.C.F. Pereira, and J.M..P. Rocha, Numerical Computation of Convective Dispersion in Turbulent Buoyant Jets, *Numerical Heat Transfer*, Part A, Vol. 23, pp. 399-414, 1993.

[21] G. Riopelle, G.D. Stubley, and A.B. Strong, Numerical Study of the Influence of the Ambient Pressure Field on Free Plane Turbulent Vertical Jets and Plumes, *Numerical Heat Transfer*, Part A, Vol. 26, pp. 273-286, 1994.

[22] G. Gerodimos, and R.M.C. So, Near-Wall Modeling of Plane Turbulent Wall Jets, *ASME Journal of Fluid Engineering*, Vol. 119, pp. 304-313, 1997.

[23] X. Zhou, Z. Sun, F. Durst and G. Brenner, Numerical Simulation of Turbulent Jet Flow and Combustion, *An International Journal of Computers & Mathematics with Applications*, Vol. 38, pp. 179-191, 1999.

[24] N.R. Panchapahesan, and J.L. Lumley, Turbulence Measurements in Axisym-

metric Jets of Air and Helium, Part 1, Air Jet, *Journal of Fluid Mechanics*, Vol. 246, pp. 197-223, 1993.

[25] F.C. Lockwood, and H.A. Moneib, Fluctuating Temperature Measurements in a Heated Round Free Jet, *Combustion, Science and Technology*, Vol. 22, pp. 63-81, 1980.

[26] X. Zhou, G. Brenner, T. Weber, and F. Durst, Finite-Rate Chemistry in Modelling of Two-Dimensional Jet Premixed CH_4/Air Flame, *International Journal of Heat and Mass Transfer*, Vol. 42, pp. 1757-1773, 1999.

[27] Q.V. Nguyen, R.W. Dibble, C.D. Carter, G.J. Fiechtner, and R.S. Barlow, Raman-LIF Measurements of Temperature, Major Species, OH and NO in Methane-Air Bunsen Flame, *Combustion and Flame*, Vol. 105, pp. 449-510, 1996.

[28] X. Zhou, Z. Sun, G. Brenner, and F. Durst, Combustion Modelling of Turbulent Jet Diffusion H_2/Air Flame With Detailed Chemistry, *International Journal of Heat and Mass Transfer*, Vol. 43, pp. 2075-2088, 2000.

[29] P. G. Hill, and P. Ouellette, Transient Turbulent Gaseous Fuel Jets for Diesel Engines, *ASME Journal of Fluid Engineering*, Vol. 121, pp. 93-101, 1999.

[30] J.S. Turner, The Starting Plume in Neutral Surroundings, *Journal of Fluid Mechanics*, Vol. 13, pp. 356-368, 1962.

[31] F.P. Ricou, and D.B. Spalding, Measurement of Entrainment by Asymmetrical Turbulent Jets, *Journal of Fluid Mechanics*, Vol. 11, Part 1, pp. 21-32, 1961.

[32] P. Ouellette, and P.G. Hill, Turbulent Transient Gas Injections, *ASME Journal of Fluid Engineering*, Vol. 122, pp. 743-753, 1999.

[33] J. Abraham, Entrainment Characteristics of Transient Gas Jets, *Numerical Heat Transfer*, Part A, Vol. 30, pp. 347-364, 1996.

[34] G. Singh, T. Sundararajan, and U.S.P. Shet, Entrainment and Mixing Studies for a Variable Density Confined Jet, *Numerical Heat Transfer*, Part A, Vol. 35, pp. 205-223, 1999.

[35] R.E. Breidenthal, The Turbulent Exponential Jet, *Physics of Fluids*, Vol. 29, No. 8, pp. 2346-2347, 1986.

[36] X. Boyan, and M. Furuyama, Jet Characteristics of CNG Injector with MPI System, *JSAE Review*, Vol. 19, pp. 229-234, 1998.

[37] J. Park, and H.D. Shin, Experimental Investigation of the Developing Process of an Unsteady Diffusion Flame, *Combustion and Flame*, Vol. 110, 42, pp. 67–77, 1997.

[38] K. Bremhorst, and P.G. Hollis, Velocity Field of an Axisymmetric Pulsed, Subsonic Air Jet, , *AIAA Journal*, Vol. 28, No. 12, pp. 2043-2049, 1990.

[39] J.S. Turner, Turbulent Entrainment: The Development of the Entrainment Assumption, and its Application to Geophysical Flows, *Journal of Fluid Mechanics*, Vol. 173, pp. 431-471, 1986.

[40] F. Fang, and B.L. Sill, Experimental Investigation of Unsteady Submerged Axisymmetric Jets, *Journal of Hydraulic Engineering*, Vol. 113, No. 5, pp. 663-669, 1987.

[41] H. Kouros, R. Medina, and H. Johari, Spreading Rate of an Unsteady Turbulent Jet, *AIAA Journal*, Vol. 31, No. 8, pp. 1524-1526, 1993.

[42] H. Johari, Q. Zhang, M.J. Rose, and S.M. Bourque, Impulsively Started Turbulent Jets, *AIAA Journal*, Vol. 35, No. 4, pp. 657-662, 1997.

[43] G. Papadopoulos and W.M. Pitts, Scaling the Near-Field Centerline Mixing Behavior of Axisymmetric Turbulent Jets, *AIAA Journal*, Vol. 36, No. 9, pp. 1635-1642, 1998.

[44] G. Papadopoulos, and W.M. Pitts, A Generic Centerline Velocity Decay Curve for Initially Turbulent Axisymmetric Jets, *ASME Journal of Fluid Engineering*, Vol. 121, pp. 80-85, 1999.

[45] J. Mi, and G.J. Nathan, Effect of Small Vortex-Generators on Scalar Mixing in the Developing Region of a Turbulent Jet, *International Journal of Heat and Mass Transfer*, Vol. 42, pp. 3919-3926, 1999.

[46] S. Aydore, and P.J. Disimile, Natural Coherent Structure Dynamics in Near Field of Fully Turbulent Axisymmetric Jet, *AIAA Journal*, Vol. 35, No. 7, pp. 1171-1178, 1997.

[47] H.B. Song, S. H. Yoon, and D. Hee, Flow and Heat Transfer Characteristics of a Two-Dimensional Oblique Wall Attaching Offset Jet, *International Journal of Heat and Mass Transfer*, Vol. 43, pp. 2395-2404, 2000.

[48] S.M. Hosseinalipour, and A.S. Mujumdar, Flow and Thermal Characteristics of Steady Two-Dimensional Confined Laminar Opposing Jets: Part I. Equal Jets, *Int. Comm. Heat Mass transfer*, Vol. 24, No. 1, pp. 27-38, 1997.

[49] S.M. Hosseinalipour, and A.S. Mujumdar, Flow and Thermal Characteristics of Steady Two-Dimensional Confined Laminar Opposing Jets: Part II. Unequal Jets, *Int. Comm. Heat Mass transfer*, Vol. 24, No. 1, pp. 39-50, 1997.

[50] D.A. Johnson, Experimental and Numerical Examination of Confined Laminar Opposed Jets. Part I. Momentum Imbalance, *Int. Comm. Heat Mass transfer*, Vol. 27, No. 4, pp. 443-454, 2000.

[51] D.A. Johnson, Experimental and Numerical Examination of Confined Laminar Opposed Jets. Part II. Momentum Balancing, *Int. Comm. Heat Mass transfer*, Vol. 27, No. 4, pp. 455-463, 2000.

[52] S.M. Hosseinalipour, and A.S. Mujumdar, Comparative Evaluation of Different Turbulence Models for Confined Impinging and Opposing Jet Flows, *Numerical Heat Transfer,* Part A, Vol. 28, pp. 647-666, 1995.

[53] W.J. Sheu, and N.C. Liou, Efficiency of Heat Transfer Between Opposed Corotating Jets, *Numerical Heat Transfer,* Part A, Vol. 36, pp. 35-49, 1999.

[54] K.M. Lam, and H.C. Chan, Round Jet in Ambient Counter Flowing Stream, *ASME Journal of Hydraulic Engineering*, Vol. 123, No. 10, pp. 895-903, 1997.

[55] N. Benet, L. Falk, H. Muhr, and E. Plasari, Characterization and Modelling of a Two Impinging Jet Mixer for Precipitation Process Using Laser Induced Fluorescence, *10^{th} European conference on mixing*, pp. 35-44, 2000.

[56] P.O. Witze, and H.A. Dwyer, The Turbulent Radial Jet, *Journal of Fluid Mechanics*, Vol. 75, No. 3, pp. 401-417, 1976.

[57] M.A. Jarrah, T.K. Aldoss, and A.M. Al-Sarkhi, Interaction of Two Opposite Conical Curved Wall Jets, *International Journal of Heat and Fluid Flow*, Vol. 17, No. 4, pp. 397-402, 1996.

[58] J.N. Gonsalves, and W.W. Duley, Cutting Thin Metal Sheets with the CW CO_2 laser, *Journal of Applied Physics*, Vol. 43, No. 11, pp. 4684-4687, 1972.

[59] M.F. Modest, and H. Abakians, Evaporative Cutting of a Semi-Infinite body with Moving CW Laser, *Journal of Heat Transfer*, Vol. 108, pp. 602-607, 1986.

[60] S.Y. Bang, and M.F. Modest, Multiple Reflection Effects on Evaporative Cutting With a Moving CW Laser, *Journal of Heat Transfer*, Vol. 113, pp. 663-669, 1991.

[61] S. Roy, and M.F. Modest, CW Laser Machining of Hard Ceramics-I, Effects of Three-Dimensional Conduction, Variable Properties and Various Laser Parameters, *International Journal of Heat and Mass Transfer,* Vol. 36, No. 14, pp. 3515-3528, 1993.

[62] S.Y. Bang, S. Roy, and M.F. Modest, CW Laser Machining of Hard Ceramics-II, Effects of Multiple Reflections, *International Journal of Heat and Mass Transfer,* Vol. 36, No. 14, pp. 3529-3540, 1993.

[63] M.F. Modest, Three-Dimensional, Transient Model for Laser Machining of Ablating/Decomposing Materials, *International Journal of Heat and Mass Transfer,* Vol. 39, No. 2, pp. 221-234, 1996.

[64] M.F. Modest, Laser Through-Cutting and Drilling Models For Ablating/Decomposing Materials, *Journal of Laser Applications,* Vol. 9, pp. 137-145, 1997.

[65] B.S. Yilbas, and Z. Yilbas, Some Aspects of Laser-Metal Vapor Interaction, *Pramana—Journal of Physics*, Vol. 31, No. 5, pp. 365-381, 1988.

[66] B.S. Yilbas, R. Davies, Z. Yilbas and A. Koc, Analysis of the Absorption Mechanism During Laser-Metal Interaction, *Pramana—Journal of Physics*, Vol. 34, No. 6, pp. 473-489, 1990.

[67] P.S. Wei, and J.Y. Ho, Energy Considerations in High-Energy Beam Drilling, *International Journal of Heat and Mass Transfer,* Vol. 33, No. 10, pp. 2207-2217, 1990.

[68] R.K. Ganesh, A. Faghri, and Y. Hahn, A Generalized Thermal Modelling for Laser Drilling Process—I. Mathematical Modeling and Numerical Methodology, *International Journal of Heat and Mass Transfer,* Vol. 40, No. 14, pp. 3351-3360, 1997.

[69] R.K. Ganesh, A. Faghri, and Y. Hahn, A Generalized Thermal Modelling for Laser Drilling Process—II Numerical Simulation and Results, *International Journal of Heat and Mass Transfer,* Vol. 40, No. 14, pp. 3361-3373, 1997.

[70] Y. Zhang, and A. Faghri, Vaporization, Melting, and Heat Conduction in the Laser Drilling Process, *International Journal of Heat and Mass Transfer,* Vol. 42, pp. 1775-1790, 1999.

[71] A.V. Gusarov, A.G. Gnedovets, and I. Smurov, Two-Dimensional Gas-Dynamic Model of Laser Ablation in an Ambient Gas, *Applied Surface Science*, Vol. 154-155, pp. 66-72, 2000.

[72] A. Kar, J.A. Rothenflue, and W.P. Latham, Scaling Laws for Thick-Section Cutting With a Chemical Oxygen-Iodine Laser, *Journal of Laser Applications*, Vol. 9, pp. 279-286, 1997.

[73] V. Semak, and A. Matsunawa, The Role of Recoil Pressure in Energy Balance During Laser Materials Processing, *J. Phys. D: Appl. Phys.*, Vol. 30, pp. 2541-2552, 1997.

[74] D.C. Wilcox, *Turbulence Modeling for CFD*, chapter 5, pp. 223-252, DCW Industries Inc., 2000.

[75] H.K. Versteeg, and W. Malalasekera, *An Introduction to Computational Fluid Dynamics, The Finite Volume Method*, Longman Scientific and Technical, 1995.

[76] W. Rodi, *Turbulence Models and Their Application in Hydraulics—A State of the Art Review*, Presented by the IAHR-Section on Fundamentals of Division II: Experimental and Mathematical Fluid Dynamics, 1984.

[77] C.K.G. Lam, and K.A. Bremhorst, Modified Form of the $K - \epsilon$ Model for Predicting Wall Turbulence, *Trans. ASME, Journal of Fluid Engineering*, Vol. 103, pp. 456-460, 1981.

[78] B.S. Yilbas, G.M. Arshed, and H.I. Acar, Investigation into Laser Produced Evaporating Front Characteristics in Relation to Laser Drilling, *Lasers in Engg.*, Vol. 13, pp. 65-74, 2003.

[79] R.S. Amano, and H. Brandt, Numerical Study of Turbulent Axisymmetric Jets Impinging on a Flat Plate and Flowing into an Axisymmetric Cavity, *ASME Journal of Fluid Engineering*, Vol. 106, pp. 410-417, 1984.

[80] B.E. Launder, and D.B. Spalding, *Mathematical Models of Turbulence,* Academic Press Inc. (London) Ltd., Third Printing 1979.

[81] S.V. Patankar, *Numerical Heat Transfer and Fluid Flow*, Series in Computa-

tional Methods in Mechanics and Thermal Sciences, McGraw-Hill Book Company, 1980.

[82] B.S. Yilbas, S.Z. Shuja, and M.O. Budair, Stagnation Point Flow Over a Heated Plate: Consideration of Gas Jet Velocity Profiles, in Print, *AJSE*, pp. xx-xx, 2003.

[83] I. Wygananski, and H. Fielder, Some Measurements in the Self-Preserving Jet, *Journal of Fluid Mechanics*, Vol. 38, Part 3, pp. 577-612, 1969.

[84] P.O. Witze, The Impulsively Started Incompressible Turbulent Jet, Sandia Laboratories Report SAND80-8617, Livermore, California, 1980.

[85] R.D. Blevins, *Applied Fluid Dynamics Handbook*, Van Nostrand Reinhold Company, 1984.

VITA

Ghulam Murshed Arshed

- Born: in Karachi, Pakistan.

  Address: 2/2, sector # 23, Reta Plot, Drigh Colony, Karachi−75230, Pakistan.

  Phone: (92-21) 457-8337

  (92-21) 501-8916

- Received Bachelor of Engineering from NED University of Engineering and Technology (Mechanical engineering) Karachi, Pakistan, 1995.

- Joined Mechanical Engineering Department of King Fahd University of Petroleum and Minerals, Dhahran, as a Research Assistant in 2000.

- Finished Master of Science in Mechanical Engineering from King Fahd University of Petroleum and Minerals, Dhahran, Saudi Arabia, 2003.